

©[2014]

Kun Yu

ALL RIGHTS RESERVED

**COPPER ION ADSORPTION BY CHITOSAN GEL  
NANOPARTICLES AND CALCIUM-ALGINATE GEL BEADS  
FOR WATER PURIFICATION APPLICATIONS**

by

KUN YU

A dissertation submitted to the  
Graduate School-New Brunswick  
Rutgers, The State University of New Jersey

In partial fulfillment of the requirements

For the degree of

Doctor of Philosophy

Graduate Program in Chemical and Biochemical Engineering

Written under the direction of

Dr. Nina C. Shapley

And approved by

---

---

---

---

New Brunswick, New Jersey

JANUARY, 2014

## **ABSTRACT OF THE DISSERTATION**

Copper ion adsorption by chitosan gel nanoparticles and calcium-alginate gel beads  
for water purification applications

By KUN YU

Dissertation Director:

Dr. Nina C. Shapley

Water purification is emerging as a critical need as resources become increasingly limited. Chitosan and alginate are both low-cost natural carbohydrate materials used for the removal of heavy metal ions from aqueous solutions. The objective of this research is to enhance understanding of the process and mechanisms of copper ion adsorption by these biopolymer gel particles at multiple size scales, with the aim of guiding the next generation of biosorbent design for water purification applications.

First, the equilibrium adsorption capability of copper ions from copper sulfate solution onto chitosan gel nanoparticles, calcium-alginate gel microbeads, chitosan/alginate combination particles and large alginate gel beads at fixed pH was studied. Results show that the adsorption behavior of chitosan and alginate in the low concentration region follows the Langmuir isotherm. Chitosan gel nanoparticles exhibit a minor increase in adsorption capacity compared to other forms of chitosan. Alginate has significantly higher capacity than chitosan, which can be attributed to a comparatively higher density

of adsorption sites. Combination particles consisting of alginate microbeads coated with chitosan nanoparticles possess an intermediate maximum adsorption capacity, corresponding to the weight ratio of the alginate and chitosan.

Also, adsorption kinetics of copper ions onto calcium-alginate gel microbeads, chitosan/alginate combination particles and large alginate gel beads were investigated. It was observed that the adsorption kinetics of large alginate gel beads was much faster than that of alginate microbeads and combination particles. The adsorption of copper ions on to combination particles was slightly faster than on to plain alginate microbeads. A pseudo-second order kinetic model successfully predicted the adsorption behavior over the whole range of studies, indicating that chemisorption is the rate controlling step and the chemisorption reaction is second order.

Moreover, the adsorption behavior of fixed-bed columns packed with large alginate gel beads was studied by varying the column size and volumetric flow rate. The column had shorter active life at a higher flow rate, or at a smaller size. The Thomas model, Adams-Bohart model and Yoon-Nelson model successfully fit experimental data, allowing prediction of the breakthrough time.

# Acknowledgement

First and foremost, I would like to express my sincere gratitude to my advisor, Dr. Nina Shapley, for her continuous support to my Ph.D study and research, for her help and guidance throughout this project. I really appreciate her wisdom, patience, and kindness. I have learned a lot from her immense knowledge, optimism and enthusiasm.

None of the experiments in this dissertation would have been possible without the expertise of Dr. Elizabeth McCandlish and Dr. Brian Buckley from Chemical Analytical Core Laboratory in Environmental and Occupational Health Sciences Institute. They were very pleasure to work with, and provided me lots of excellent data on the ICP/MS testing. And I also want to thank Dr. Rajesh Patel from Core Imaging Laboratory in the Department of Pathology. He was very patient, and always managed to find the best way to take TEM images of my samples.

I am very fortunate to be in Dr. Nina Shapley's group with a wonderful group of people. I am glad I could have the opportunity to get to know and work with numbers of colleagues and undergraduate students: Kristin Steeley, Kapil Deshpande, Zhoubo Li, Shiwen Sun, Jackie Ho, Adam Cham, Jenna Lo, Eric Somers, Louis Ruggieri and Nhan Pham. I especially want to acknowledge Jackie Ho, one of the undergraduate students working in our lab. He is very smart, reliable and hardworking. He inspired me and helped me a lot on the equilibrium experiments.

I would also like to thank my parents. They were always supporting me and encouraging me with their best wishes.

Finally, I would like to thank my husband Fei Xiang for his love and unwavering support. He was always there cheering me up and stood by me through the good times and bad.

# Table of Contents

<b>ABSTRACT OF THE DISSERTATION .....</b>	<b>ii</b>
<b>Acknowledgement .....</b>	<b>iv</b>
<b>List of Tables .....</b>	<b>ix</b>
<b>List of Figures.....</b>	<b>xi</b>
<b>Chapter 1 Introduction.....</b>	<b>1</b>
1.1 Significance/Motivation.....	1
1.2 Background .....	4
1.2.1 Chitosan and alginate .....	4
1.2.2 Equilibrium adsorption isotherms.....	10
1.2.3 Adsorption kinetics .....	11
1.2.4 Fixed-bed column .....	15
<b>Chapter 2 Methodology.....</b>	<b>20</b>
2.1 Particle synthesis.....	20
2.1.1 Materials .....	20
2.1.2 Preparation of chitosan nanoparticles .....	21
2.1.3 Preparation of calcium-alginate gel microbeads.....	22
2.1.4 Preparation of chitosan/alginate combination particles (weight ratio 1:0.45) .	22
2.1.5 Preparation of large calcium-alginate gel beads .....	23
2.2 Particle characterization.....	24
2.2.1 Zetasizing .....	24
2.2.2 TEM imaging .....	24
2.2.3 Laser diffraction.....	25
2.2.4 Microscope imaging.....	25
2.3 Equilibrium adsorption experiment .....	26
2.4 Adsorption kinetics experiment .....	28
2.5 Fixed-bed column experiment .....	29
<b>Chapter 3 Equilibrium Study of Copper Ion Adsorption by Chitosan Nanoparticles, Calcium-Alginate Gel Microbeads, Large Calcium-Alginate Gel Beads and Chitosan/Alginate Combination Particles .....</b>	<b>31</b>
3.1 Introduction.....	31
3.2 Experimental methods .....	32

3.2.1 Materials .....	32
3.2.2 Preparation of particles .....	33
3.2.3 Particle characterization .....	36
3.2.4 Equilibrium adsorption experiment .....	38
3.3 Results and discussion .....	40
3.3.1 Particle Characterization .....	40
3.3.2 Particle adsorption capability .....	48
3.4 Summary .....	63
<b>Chapter 4 Kinetics Study of Copper Ion Adsorption by Calcium-Alginate Gel Microbeads, Large Calcium-Alginate Gel Beads and Chitosan/Alginate Combination Particles .....</b>	<b>66</b>
4.1 Introduction .....	66
4.2 Experimental Methods .....	67
4.2.1 Particle synthesis .....	67
4.2.2 Adsorption experiment .....	68
4.3 Results and Discussion .....	69
4.4 Summary .....	78
<b>Chapter 5 Copper Ion Removal by Fixed-Bed Columns .....</b>	<b>80</b>
5.1 Introduction .....	80
5.2 Experimental Methods .....	81
5.2.1 Preparation of large calcium-alginate gel beads .....	81
5.2.2 Fixed-bed column experimental procedures .....	81
5.3 Results and Discussion .....	83
5.3.1 Fixed-bed column adsorption results .....	83
5.3.2 Model comparison .....	91
5.4 Summary .....	105
<b>Chapter 6 Rheology of a Concentrated Bimodal Suspension Containing Rigid and Soft Particles .....</b>	<b>107</b>
6.1 Introduction .....	107
6.2 Experimental Methods .....	114
6.2.1 Materials .....	114
6.2.2 Rheological test .....	116
6.3 Results and Discussion .....	117



6.3.1 Monomodal suspension .....	117
6.3.2 Bimodal suspension .....	120
6.3.3 Model design.....	131
6.3 Summary .....	134
<b>Chapter 7 Conclusion and Future Work .....</b>	<b>136</b>
7.1 Conclusion .....	136
7.2 Future work.....	142
<b>Acknowledgement of Previous Publications.....</b>	<b>144</b>
<b>References .....</b>	<b>145</b>

# List of Tables

Table 2-1. ICPMS procedure. ....	27
Table 3-1. Number weighted diameter, volume weighted diameter, intensity weighted diameter and Z-average diameter of chitosan nanoparticles prepared with 2 mg/mL chitosan solution and 0.25 mL TPP, 0.7 mL TPP and 1.0 mL TPP, respectively. ....	46
Table 3-2. Swelling ratio, $Q_{\max}$ (calculated based on both wet mass and dry mass), $K_s$ and correlation coefficients of chitosan nanoparticles prepared with 2 mg/mL chitosan solutions and 1.0 mL TPP or 0.7 mL TPP, chitosan nanoparticles prepared with 4 mg/mL chitosan solution and 1.0 mL TPP, calcium-alginate gel microbeads and large calcium-alginate gel beads in the low $\text{Cu}^{2+}$ concentration region (0.5-50 mM). ....	53
Table 3-3. Literature values for equilibrium adsorption capacity of compared with the results of this study. ....	56
Table 3-4. $K_F$ , $1/n$ and correlation coefficients of linear Freundlich adsorption isotherms for 1 mg/mL, 2 mg/mL, 4 mg/mL chitosan nanoparticles and calcium-alginate gel microbeads in the high $\text{Cu}^{2+}$ concentration region (50 mM-1M). ....	58
Table 3-5. Experimental adsorption capability and estimated adsorption capabilities ( $Q_{\max}$ ) calculated by binding models. ....	60
Table 3-6. Adsorption capacity and affinity of chitosan nanoparticles (prepared with 2 mg/mL chitosan solution and 0.7 mL TPP), calcium-alginate gel microbeads and alginate-chitosan combination particles in the low $\text{Cu}^{2+}$ concentration region (0.5-50 mM). ....	61
Table 4-1. Parameters of adsorption kinetics models. ....	77
Table 4-2. Literature values of pseudo-second order adsorption kinetics of copper ions on to various adsorbents compared with the results of this study. (The values of $k_2$ of this study were recalculated based on dry mass) ....	78
Table 5-1. Operation parameters of large columns and small columns at flow rates of 0.1 mL/min, 0.25 mL/min and 1 mL/min. ....	91
Table 5-2. Statistical data of the Thomas model fit to large columns and small columns at the flow rates of 0.1 mL/min, 0.25 mL/min and 1 mL/min. ....	96
Table 5-3. Statistical data of the Adams-Bohart model fit to the large columns and small columns at the flow rates of 0.1 mL/min, 0.25 mL/min and 1 mL/min. ....	101

Table 5-4. Statistical data of the Yoon-Nelson model fit to the large columns and small columns at the flow rates of 0.1 mL/min, 0.25 mL/min and 1 mL/min.....	103
--	-----

# List of Figures

Figure 1-1. Chemical structure of chitosan, showing glucosamine subunits and protonated amine groups [19] .....	5
Figure 1-2. Formation of chitosan chelates with copper ion (a) “bridge model” (b) “pendant model”[31].....	7
Figure 1-3. Cross-linking of chitosan with tripolyphosphate (TPP)[19]. .....	8
Figure 1-4. Chemical structure of alginate showing mannuronic acid (M) and guluronic acid (G) subunits [37]. .....	9
Figure 2-1. Schematic view of syringe pump, needle, and cross-linking bath for bead production.[40].....	23
Figure 2-2. Schematic view of fixed-bed column experiment.....	30
Figure 3-1. Diameter of chitosan nanoparticles produced at three synthesis solution concentrations (1 mg/mL, 2 mg/mL and 4 mg/mL, prepared with varying amounts of TPP). .....	41
Figure 3-2. Size distribution of alginate microbeads measured by laser diffraction spectroscopy.....	42
Figure 3-3. Zeta potential of chitosan nanoparticles produced at three synthesis solution concentrations (1 mg/mL, 2 mg/mL and 4 mg/mL prepared with varying amounts of TPP). .....	43
Figure 3-4. TEM image of chitosan nanoparticles prepared with 2 mg/mL chitosan solution and 0.25 mL TPP, stained with copper sulfate solution. Diameter range: approximately 18 - 244 nm. ....	44
Figure 3-5. TEM image of chitosan nanoparticles prepared with 2 mg/mL chitosan solution and 0.7 mL TPP, stained with copper sulfate solution. Diameter range: approximately 36 - 240 nm. ....	45
Figure 3-6. TEM image of chitosan nanoparticles prepared with 2 mg/mL chitosan solution and 1.0 mL TPP, stained with copper sulfate solution. Diameter range: approximately 28 -226 nm. ....	45
Figure 3-7. TEM images of calcium-alginate gel microbeads coated with chitosan nanoparticles prepared with 2 mg/mL chitosan solution and 0.7 mL TPP, stained with	

copper sulfate solution. The weight ratio of calcium-alginate gel microbeads to chitosan nanoparticles is 1:0.45. ....	47
Figure 3-8. Microscope image of a large calcium-alginate gel bead at 5x magnification.	47
Figure 3-9. Adsorption isotherms of chitosan nanoparticles prepared with 2 mg/mL chitosan solution and 1.0 mL TPP or 0.7 mL TPP, and chitosan nanoparticles prepared with 4 mg/mL chitosan solution and 1.0 mL TPP in the low $\text{Cu}^{2+}$ concentration region (0.5-50 mM). ....	50
Figure 3-10. Adsorption isotherms of 2 mg/mL chitosan nanoparticles prepared with 1.0 mL TPP and 0.7 mL TPP, 4 mg/mL chitosan nanoparticles prepared with 1.0 mL TPP, calcium-alginate gel microbeads and large calcium-alginate gel beads in the low $\text{Cu}^{2+}$ concentration region (0.5-50 mM). ....	51
Figure 3-11. Linear adsorption isotherms of chitosan nanoparticles prepared with 2 mg/mL chitosan solution and 1.0 mL TPP or 0.7 mL TPP, chitosan nanoparticles prepared with 4 mg/mL chitosan solution and 1.0 mL TPP, calcium-alginate gel microbeads and large calcium-alginate gel beads in the low $\text{Cu}^{2+}$ concentration region (0.5-50 mM). The lines shown are Langmuir equation fits to the data. ....	52
Figure 3-12. Adsorption isotherms of chitosan nanoparticles prepared with 1 mg/mL, 2 mg/mL or 4 mg/mL chitosan solutions and 1.0 mL TPP, and calcium-alginate gel microbeads in the high $\text{Cu}^{2+}$ concentration region (50 mM-1M). The lines represent linear curve fits to the data. ....	57
Figure 3-13. Linear adsorption isotherms of chitosan nanoparticles prepared with 1 mg/mL, 2 mg/mL or 4 mg/mL chitosan solutions and 1.0 mL TPP, and calcium-alginate gel microbeads in the high $\text{Cu}^{2+}$ concentration region (50 mM-1M). The lines shown are Freundlich equation fits to the data. ....	58
Figure 3-14. Adsorption isotherms of alginate-chitosan combination particles, calcium-alginate gel microbeads and chitosan nanoparticles (prepared with 2 mg/mL chitosan solution and 0.7 mL TPP) in the low $\text{Cu}^{2+}$ concentration region (0.5-50 mM). ....	61
Figure 3-15. Estimated vs. measured adsorption capability of combination particles. ....	62
Figure 4-1. $\text{Cu}^{2+}$ adsorbed onto calcium-alginate microbeads, combination particles and large calcium-alginate gel beads over time. ....	73
Figure 4-2. Linear pseudo-first order equation fit to adsorption data of calcium- alginate microbeads, combination particles and large calcium-alginate gel beads over time. ....	74

Figure 4-3. Linear pseudo-second order equation fitted to adsorption data of calcium-alginate microbeads, combination particles and large calcium-alginate gel beads over time. ....	77
Figure 5-1. Breakthrough curves of the large fixed-bed column when the flow rate was 0.1 mL/min, 0.25 mL/min and 1 mL/min. ....	85
Figure 5-2. Breakthrough curves of the small fixed-bed column when the flow rate was 0.1 mL/min, 0.25 mL/min and 1 mL/min. ....	87
Figure 5-3. Breakthrough curves of the large column and small column at the flow rate of 0.1 mL/min.....	88
Figure 5-4. Breakthrough curves of the large column and small column at the flow rate of 0.25 mL/min.....	89
Figure 5-5. Breakthrough curves of the large column and small column at the flow rate of 1 mL/min.....	89
Figure 5-6. Linear Thomas model fit to adsorption data of the large column and small column at a flow rate of 0.1 mL/min. ....	94
Figure 5-7. Linear Thomas model fit to adsorption data of the large column and small column at a flow rate of 0.25 mL/min. ....	95
Figure 5-8. Linear Thomas model fit to adsorption data of the large column and small column at a flow rate of 1 mL/min. ....	95
Figure 5-9. Predicted breakthrough curves of the large column at 0.1 mL/min, 0.25 mL/min and 1 mL/min flow rate by the Thomas model.....	97
Figure 5-10. Predicted breakthrough curves of the small column at 0.1 mL/min, 0.25 mL/min and 1 mL/min flow rate by the Thomas model.....	97
Figure 5-11. Linear Adams-Bohart model fit to adsorption data of the large column at flow rates of 0.1 mL/min, 0.25 mL/min and 1 mL/min.....	100
Figure 5-12. Linear Adams-Bohart model fit to adsorption data of the small column at flow rates of 0.1 mL/min, 0.25 mL/min and 1 mL/min.....	100
Figure 5-13. Linear Yoon-Nelson model fit to adsorption data of the large column at flow rates of 0.1 mL/min, 0.25 mL/min and 1 mL/min. ....	102
Figure 5-14. Linear Yoon-Nelson model fit to adsorption data of the small column at flow rates of 0.1 mL/min, 0.25 mL/min and 1 mL/min.....	103

Figure 6-1. Size distribution of PMMA (25 vv% ) and alginate (25 vv% ) bimodal suspension measured by laser diffraction spectroscopy. ....	116
Figure 6-2. Relative viscosity of PMMA monomodal suspensions with particle volume fraction varying from 10% to 50%, and shear rate ranging from $5 \text{ s}^{-1}$ to $200 \text{ s}^{-1}$ . ....	118
Figure 6-3. Relative viscosity of alginate monomodal suspensions with particle volume fraction varying from 10% to 50% and shear rate ranging from $5 \text{ s}^{-1}$ to $200 \text{ s}^{-1}$ . ....	119
Figure 6-4. Average relative viscosity data of PMMA suspensions and alginate suspensions with particle volume fraction varying from 10% to 50%. ....	120
Figure 6-5. Relative viscosity of PMMA/alginate bimodal suspensions where the bulk particle volume fraction was fixed at 50% and the shear rate varied from $5 \text{ s}^{-1}$ to $200 \text{ s}^{-1}$ . ....	123
Figure 6-6. Relative viscosity of PMMA/alginate bimodal suspensions where the volume fraction of PMMA was fixed at 40%, and the shear rate varied from $5 \text{ s}^{-1}$ to $200 \text{ s}^{-1}$ . ...	125
Figure 6-7. Relative viscosity of PMMA/alginate bimodal suspensions where the volume fraction of PMMA was fixed at 45%, and the shear rate varied from $5 \text{ s}^{-1}$ to $200 \text{ s}^{-1}$ . ...	125
Figure 6-8. Relative viscosity of PMMA/alginate bimodal suspensions where the particle volume fraction of alginate beads was fixed at 10%, and the shear rate varied from $5 \text{ s}^{-1}$ to $200 \text{ s}^{-1}$ . ....	127
Figure 6-9. Intensity of shear dependence of PMMA/alginate bimodal suspensions with varied bulk concentration $\phi$ and relative volume fraction of small particles $k$ . $\blacktriangle$ : $\phi = 45\%$ , $\blacklozenge$ : $\phi = 50\%$ , $\bigcirc$ : $\phi = 51\%$ , $\bullet$ : $\phi = 52\%$ , $\square$ : $\phi = 55\%$ , $*$ : $\phi = 60\%$ . ....	129
Figure 6-10. Estimated relative viscosity of PMMA/alginate bimodal suspensions by Qi's model vs. experimental data where the bulk concentration $\phi$ was fixed at 50% and the relative volume fraction of small particles $k$ was varied. ....	130
Figure 6-11. Estimated relative viscosity of alginate monomodal suspensions by modified Maron-Pierce-Kitano model vs. experimental data. ....	131
Figure 6-12. Estimated relative viscosity of PMMA/alginate bimodal suspensions by new model vs experimental data when bulk concentration $\phi$ was fixed at 50% and relative volume fraction of small particles $k$ was varied. ....	133
Figure 6-13. Comparison of estimated relative viscosity of PMMA/alginate bimodal suspensions by Qi's model, new model and experimental data when bulk concentration $\phi$ was fixed at 50% and relative volume fraction of small particles $k$ was varied. ....	133

## **Chapter 1 Introduction**

### **1.1 Significance/Motivation**

Clean water is currently a leading environmental concern. Water purification is emerging as a critical need as resources become increasingly limited. Common toxic waterborne contaminants include bacteria, viruses, organic solvents and heavy metal ions, which are often found in industrial chemical waste streams. The presence of heavy metals in water has led to a serious environmental problem. For example, copper is one of the most widely used metals, which often appears in metal-bearing industrial effluents. For humans, copper is an essential element and the body can regulate its level homeostatically, but large, acute doses can be harmful, even producing fatal effects.

Conventional methods to remove heavy metal ions from industrial effluents include adsorption, precipitation, filtration, and electrochemical treatment. Most of these methods are expensive and incapable of removing trace levels of heavy metal ions[1, 2]. Adsorption is an effective and economical separation process that can be employed in water purification. In recent years, much active research has been performed on novel adsorbents and has explored various configurations of adsorbents to maximize their adsorptive capacity, but few of them incorporate nanotechnology.



Recent EPA (Environmental Protection Agency) publications highlight the potential of nanomaterials[3], which possess very high surface area to mass ratios, to contribute to the development of cost-effective and environmentally benign water purification technologies. Improvements in the capacity and speed of removing heavy metal ions from industrial wastewater can potentially offer huge benefits in water supply and recycling, as well as improving industrial efficiency and lowering costs. Typical equilibrium adsorption times for metal ions in microscale sorbents are several hours, while it is likely that nanoscale sorbents can accelerate the adsorption kinetics. However, the promise of nanotechnology has not yet been applied in the area of water purification, since the supply of synthetic nanomaterials, such as carbon nanotubes, is limited, and there is some concern regarding environmental fate and toxicity of nanomaterials.

On both of these criteria, polysaccharides derived from natural marine extracts are an excellent choice for producing nanomaterials for water purification systems. In this research, we use chitosan and alginate, which are highly abundant, edible and biocompatible, as nano/micro scale biosorbents, to seek enhanced understanding of the process and mechanisms of metal ion adsorption, with the aim of guiding the next generation of water purification system design.

In this study, Chapter 2 provides the methodology of particle synthesis, particle characterization, equilibrium adsorption experiment, kinetics experiment, and fixed-bed column adsorption experiment. In Chapter 3, equilibrium adsorption of copper ions onto chitosan gel nanoparticles, calcium-alginate gel microbeads, chitosan/alginate

combination particles and large alginate gel beads was investigated. Particles were synthesized and characterized by TEM and zetasizing. The amount of copper ions adsorbed from copper sulfate solution on to different types of particles was measured at fixed pH by ICP/MS. Langmuir isotherm and Freundlich isotherm models were fit to experimental adsorption data, in order to assess particles' adsorption capacity and affinity of adsorptive sites to copper ions. Adsorption mechanisms were discussed, and adsorption capacities of different particles were compared.

In Chapter 4, in order to explore adsorption kinetics, the amount of copper ions adsorbed from copper sulfate solution on to calcium-alginate gel microbeads, chitosan/alginate combination particles and large gel alginate beads over different time periods was obtained. Experimental data were compared to pseudo-first order and pseudo-second order kinetic models, by which pseudo rate constants were estimated and the potential rate-controlling step was clarified.

After optimizing biosorbent choice by analyzing equilibrium adsorption data and adsorption kinetics of particles, this work was then extended to Chapter 5, in which the adsorption study in a continuous system was performed. Copper sulfate solution was pumped into two sizes of fixed-bed columns at varied volumetric flow rate. Copper ion concentration in the effluent was measured at multiple time points. Continuous adsorption data were fit with the Thomas model, Adams-Bohart model and Yoon-Nelson model, and fixed-bed column operation breakthrough curves and adsorption coefficients

were obtained. The adsorption performance of fixed-bed columns was investigated in order to provide specific information for novel water purification system design.

Chapter 6 focuses on the rheology of a concentrated bimodal suspension containing rigid and soft particles. This project studies the rheological properties of PMMA/alginate bimodal suspensions, with the aim to provide insights into particle migration and separation in complex flow, and therefore aids the further design and loading of fixed-bed columns. In this study, the relative viscosities of bimodal suspensions consisting of rigid, large PMMA particles and soft, small alginate gel beads with varied relative particle volume fraction and total bulk concentration were measured in a parallel plate viscometer. The rheological properties of rigid/soft particle bimodal suspensions were discussed and a recent model for bimodal suspension viscosity was adapted for rigid/soft bimodal suspensions. Finally, in Chapter 7, conclusions and potential future work are listed.

## **1.2 Background**

### **1.2.1 Chitosan and alginate**

Natural carbohydrate biopolymers such as chitosan and alginate are receiving increasing attention due to their extraordinary affinity to heavy metal ions. Particularly in gel

particle form, the uptake is comparable to or even beyond that of commercial ion exchange resins. In addition, the materials are abundant, biocompatible and environmentally friendly, making them potential biosorbents for the removal of pollutants from wastewater [4-14].

Chitosan has been studied extensively over the last decade due to its unique properties in adsorbing heavy metal ions from industrial chemical waste streams. It is a promising biopolymer obtained cost-effectively by the derivation of chitin, which is a natural material found widely in crustacean shells. Chitosan is composed of poly( $\beta$ -1-4)-2-amino-2-deoxy-D-glucopyranose, and the chemical structure is shown in Figure 1-1. In acidic solutions ( $\text{pH} < 6.5$ ) chitosan is positively charged, due to the prevalence of amine groups which become protonated at low pH. Chitosan has been shown to effectively remove metals such as chromium [4-7], copper [4, 8-10], mercury [11, 12] and lead [13, 14] from aqueous solutions. Additional applications to which chitosan is particularly well-suited include drug delivery [15], flocculation [16] and antimicrobial treatment [17, 18].

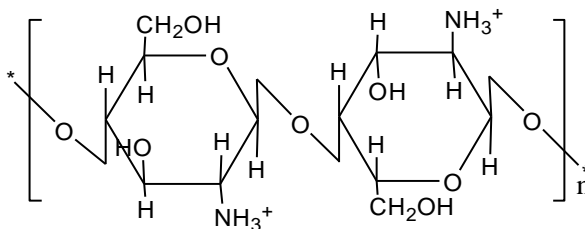


**Figure 1-1.** Chemical structure of chitosan, showing glucosamine subunits and protonated amine groups [19]

Chitosan contains several reactive groups which interact with metal ions through various mechanisms depending on the ion, the pH, and solution composition [20, 21]. The amine groups of the chitosan are generally recognized as the main active sites for metal ion adsorption, while hydroxyl groups (especially in the C-3 position) may contribute to adsorption as well [21]. Possible adsorption mechanisms of metal ion uptake by chitosan include chelation, ion exchange/electrostatic attraction and formation of ternary complexes. Chelation is the most widely indicated binding mechanism to describe transition metal ion adsorption by chitosan. During chelation, the nitrogen atoms in amine groups of chitosan can create dative covalent bonds with the copper ions. Some hydroxyl groups may also release protons to and participate in the coordination. Therefore, rings of association are formed involving the nitrogen atoms of non-protonated amine groups and the oxygen atoms of the hydroxyl groups of chitosan[21, 22]. Protonation and chelation of amine groups compete during adsorption in aqueous solutions ( $\text{pH} < 6.5$ ). Chelation of metal ions by chitosan is either classified as the “bridge model” or the “pendant model,” depending on the binding pattern as shown in Figure 1-2. In the “bridge model,” metal ions are bound with two amine groups from the same chain or from different chains, via inter- or intramolecular complexation [23-26], as opposed to the “pendant model,” in which the metal ion is bound to only one amine group in a pendant fashion, and hydroxyl groups and pairs of oxygen atoms in water molecules may be involved in the coordination [27-31].

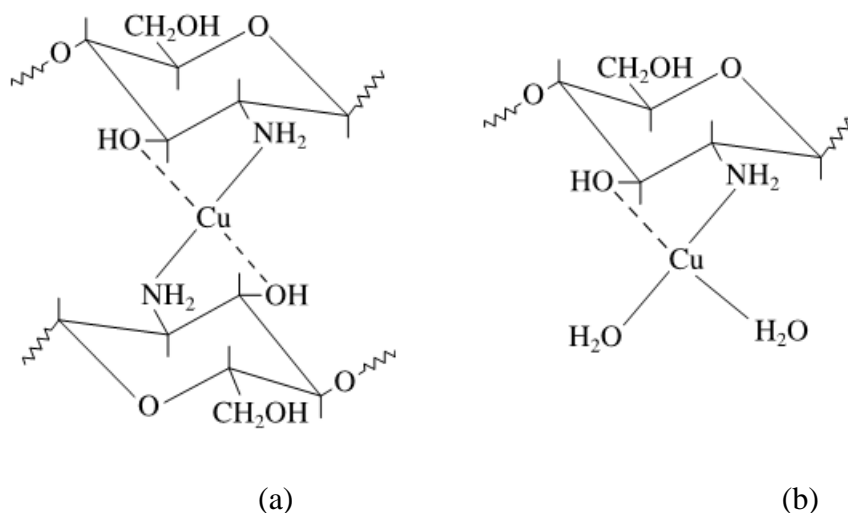


**Figure 1-2.** Formation of chitosan chelates with copper ion (a) “bridge model” (b) “pendant model”[31]

Chemical and physical modifications of chitosan have been commonly used to increase the stability of the polymer in acid solution and improve its adsorption capacities. Chemical modifications such as cross-linking are used to great effect. According to Hsien and Rorrer [32], an increase in the adsorption capacity of chitosan after a cross-linking process is explained by the increase in space among chitosan chains, which is responsible for an improvement in the accessibility of the amine groups to the metallic ions by lowering the crystallinity and thus freeing the entangled polymer chains. The flexible nature of the polymer chain allows for the special structure during complexation of the metal ion [33]. Tripolyphosphate (TPP) is a non-toxic polyanion that is suitable for water purification. The protonated amine groups in chitosan interact with the negatively charged counterion, TPP, through an electrostatic interaction creating ionic cross-linked networks [19, 34], which can prevent the dissolution of chitosan when metal adsorption is performed in acidic solutions as shown in Figure 1-3.

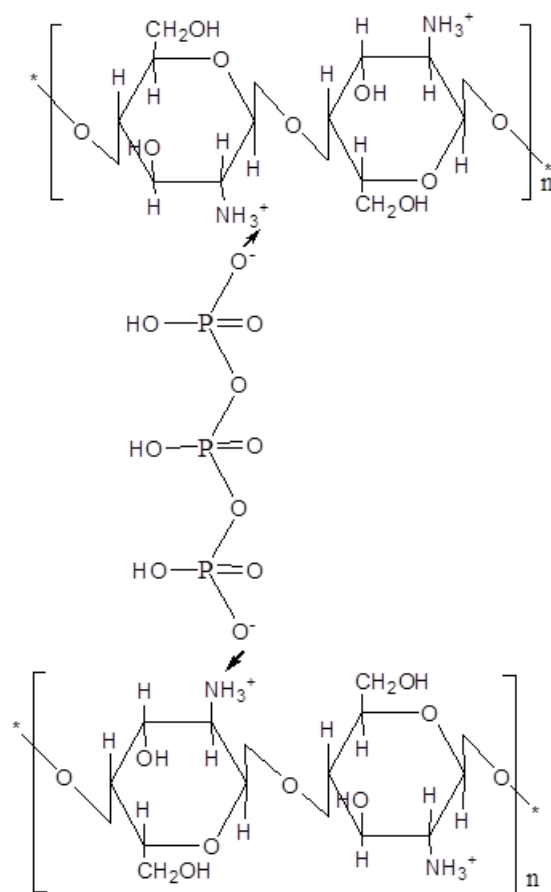


**Figure 1-3.** Cross-linking of chitosan with tripolyphosphate (TPP)[19].

Alginate is a linear copolymer formed from mannuronic acid (M) and guluronic acid (G) subunits as presented in Figure 1-4, and is produced widely in algae and certain bacteria. Alginates are used in diverse fields, such as the pharmaceutical industry [35, 36] and the food industry [37], as well as for biomedical purposes such as drug delivery [38], enzyme encapsulation for sensing [39] and contrast agent development for diagnostic imaging [40]. Alginates are also proven to be excellent materials for water purification. Much research has demonstrated that calcium-alginate gel beads can remove heavy metals from industrial wastewater.

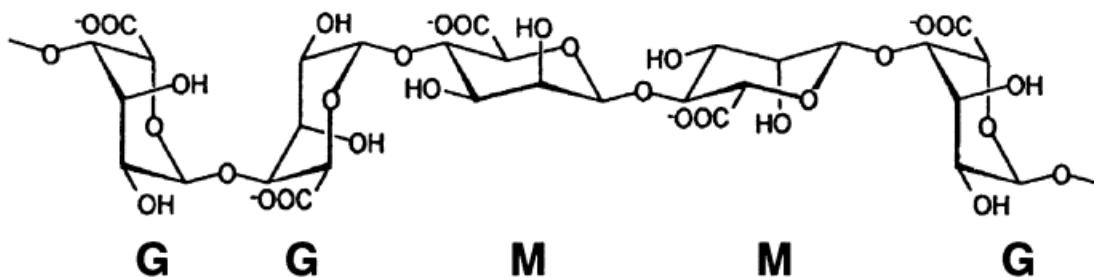


**Figure 1-4.** Chemical structure of alginate showing mannuronic acid (M) and guluronic acid (G) subunits [37].

The main binding mechanism of metal ions to calcium-alginate gel beads consists of sorption and ion exchange. In aqueous solution (at  $\text{pH} > 3.4$ ), alginate is negatively charged, due to the prevalence of carboxyl groups in both G and M subunits, where the carboxyl groups become deprotonated except at very low pH. In the gelation process, calcium cations cooperatively interact with blocks of G and M residues to form ionic cross-links between different polymer chains. The calcium cations can be replaced by ionic adsorbates such as lead [41], zinc [41, 42], mercury [42], cadmium [42], copper [43], manganese [43] and chromium [44]. Four guluronic acid (G) blocks packing together with the cations strongly coordinated in cavities between the chains is the commonly known “egg-box” model [45] for alginate cross-linking. In addition to that, recent studies have explored new hypotheses of cation binding and alginate cross-linking [46-48] which involve only one or two G and M blocks forming a binding site. Rodrigues and Lagoa suggest that the binding mechanism and the number of binding sites depend on the cation availability in the solution [49].



### 1.2.2 Equilibrium adsorption isotherms

It is important to correlate equilibrium adsorption data between metal ions and particles in order to assess the particles' capacity for metal adsorption. The effectiveness of adsorbents is often evaluated by fitting experimental adsorption data with the Langmuir and Freundlich isotherm equations, which relate  $Q$  (mg/g), the quantity of metal adsorbed per unit mass of adsorbent, to  $C_e$ (mg/L), the equilibrium metal ion concentration in the solution after adsorption.

The Langmuir model [50] is the best known and most widely applied adsorption isotherm. It has excellent agreement with a wide variety of experimental data and is represented as follows:

$$Q = \frac{Q_{\max} K_s C_e}{1 + K_s C_e} \quad (1-1)$$

The linear form of the Langmuir isotherm can be described as:

$$\frac{C_e}{Q} = \frac{C_e}{Q_{\max}} + \frac{1}{Q_{\max} K_s} \quad (1-2)$$

where  $Q_{\max}$  (mg/g) is the maximum adsorption capacity of adsorbent at monolayer coverage, and  $K_s$  (L/mg) is the Langmuir adsorption equilibrium constant related to the affinity of adsorptive sites for adsorbate at dilute concentration. This constant corresponds to the initial slope of the isotherm curve. The Langmuir isotherm assumes that the adsorption layer is a monolayer and the adsorption occurs at specific homogeneous adsorption sites resulting in an identical energy of adsorption at each site.

It is also assumed that the intermolecular attractive force decreases rapidly with the distance from the adsorption sites.

The Freundlich isotherm [51] predicts that the adsorption capacity of the adsorbent increases as a power law with an increase in adsorbate concentration. It is usually applied to multilayer adsorption and assumes an exponentially decaying distribution of the energy of adsorption sites. The Freundlich isotherm is an empirical equation presented as:

$$Q = K_F C_e^{\frac{1}{n}} \quad (1-3)$$

The linear form of the Freundlich equation can be expressed as:

$$\log Q = \frac{1}{n} \log C_e + \log K_F \quad (1-4)$$

where  $K_F$  and  $n$  are Freundlich constants. The value of  $1/n$  indicates the adsorption intensity. Moreover, adsorption sites become more heterogeneous on the surface as the value of  $1/n$  approaches zero.

### 1.2.3 Adsorption kinetics

In the design of a water purification system, the study of the adsorption kinetics of the adsorbent is essential since the kinetics affect the efficiency and in-service life of the system directly. In addition, the adsorption kinetics of an adsorbent can provide a better understanding of the adsorption mechanism and insight into the potential rate controlling steps, such as mass transport and chemical reaction processes. To achieve those goals, kinetic models have been used to analyze experimental data. It is worthy to notice that the

complete kinetics model needs to consider not only the diffusion equations, but also boundary conditions, including the adsorption isotherm equation that controls the equilibrium at the solid–liquid interface and the reaction kinetic equations[21]. Therefore, the system of equations is too complex to solve and simple kinetic models such as first- or second-order rate equations are not applicable. To simplify the solution method, only the rate controlling step is considered to contribute to the kinetic rate. In a well-mixed batch system, the influence of mass transfer resistance is negligible. Chemical reaction is most likely to be the potential rate controlling step. This hypothesis can be confirmed by fitting a pseudo-first-order equation or a pseudo-second-order equation to experimental data.

The chemical reaction of alginate and copper ions may be described as following equation[52]:



If the reaction has a first-order mechanism,

$$\frac{d[CaA]_t}{dt} = -k_1[CaA]_t \quad (1-6)$$

where  $[CaA]_t$  is the number of unreacted adsorption sites on calcium alginate at time  $t$ , that can be substituted by the total number of sites  $[CaA]_0$  subtracted by the number of occupied sites on calcium alginate  $[CaA]_r$  at time  $t$ , then

$$\frac{d[CaA]_r}{dt} = k_1([CaA]_0 - [CaA]_r) \quad (1-7)$$

Since the number of reacted adsorption sites on calcium alginate is proportional to the amount of copper loaded on alginate, assuming all sites are occupied at equilibrium, the equation becomes to the pseudo-first order chemisorption kinetic rate equation of Lagergren[53], expressed as:

$$\frac{dq_t}{dt} = k_1(q_e - q_t) \quad (1-8)$$

in which  $q_e$  (mg/g) is the amount of copper ions adsorbed onto unit mass of particles at equilibrium, and  $q_t$  (mg/g) is the amounts of copper ions adsorbed onto unit mass of particles at time  $t$ , and  $k_1$  is the rate constant of the pseudo-first order kinetic model ( $\text{min}^{-1}$ ).

After integrating from  $t = 0$  to  $t = t$  and  $q_t = 0$  to  $q_t = q_t$  and applying boundary conditions, the equation becomes:

$$q_t = q_e(1 - e^{-k_1 t}) \quad (1-9)$$

This equation can be transformed to a linear form:

$$\ln(q_e - q_t) = \ln(q_e) - k_1 t \quad (1-10)$$

where  $q_e$  can be obtained from experimental data. The straight-line plots of  $\ln(q_e - q_t)$  against  $t$  were used to determine the rate constant  $k_1$ .

The equation applicable to experimental results generally differs from a true first-order equation in two ways[54]:

- a. The parameter  $q_e - q_t$  does not represent the number of available sites, since  $q_e$  depends on the solution concentration. In other words, the assumption of full occupation of adsorption sites at equilibrium is illegitimate.
- b. The parameter  $\ln(q_e)$  is an adjustable parameter which is often not found equal to the intercept of a plot of  $\ln(q_e - q_t)$  against  $t$ , whereas in a true first-order adsorption reaction  $\ln(q_e)$  should be equal to the intercept of a plot of  $\ln(q_e - q_t)$  against  $t$ .

The pseudo-first-order kinetic model has been used extensively to describe the adsorption of metal ions onto adsorbents.

Similar to the pseudo-first order equation, the pseudo-second order chemisorption kinetic rate equation is expressed as:

$$\frac{dq_t}{dt} = k_2(q_e - q_t)^2 \quad (1-11)$$

where  $q_e$  (mg/g) is the amount of copper ions adsorbed on to a unit mass of particles at equilibrium, and  $q_t$  (mg/g) is the amounts of copper ions adsorbed on to a unit mass of particles at time  $t$ , and  $k_2$  is the rate constant of the pseudo-second order kinetic model (g/mg min).

After integrating from  $t = 0$  to  $t = t$  and  $q_t = 0$  to  $q_t = q_t$  and applying boundary conditions, the integrated form is:

$$\frac{1}{q_e - q_t} = \frac{1}{q_e} + k_2 t \quad (1-12)$$

which can be rearranged to obtain a linear form:

$$\frac{t}{q_t} = \frac{1}{k_2 q_e^2} + \frac{1}{q_e} t \quad (1-13)$$

If pseudo-second order kinetics is applicable, the plot of  $t/q_t$  against  $t$  will present a linear relationship, and equilibrium capacity  $q_e$  and rate constant  $k_2$  could be determined by the slope and intercept. The pseudo-second order kinetic model has been the most widely used model for the adsorption of metal ions from wastewater[55], and is in agreement with a chemisorption mechanism being the rate controlling step.

#### 1.2.4 Fixed-bed column

Although much research has been done and many data have been obtained from different equilibrium adsorption systems, these data are difficult to apply to fixed-bed columns, which are extensively used in industry. The major problem in equilibrium studies is that they are batch contact systems, whose isotherms cannot give accurate scale-up data in fixed-bed systems since a flow column is not at equilibrium; uneven flow patterns may occur in fixed-beds column system. A model is needed in designing columns to study recycling and regeneration of adsorbents, and to predict how long they will last before regeneration or replacement becomes necessary.

The Thomas model[56] is one of the most widely used models to evaluate column performances. The Thomas model was derived from the mass conservation equation in a continuous flow system, which demands that the solute entering a layer  $dx$  of the fixed-bed column in time  $\delta t$  be accounted for as follows:

$$cu\delta t = (c + \frac{\partial c}{\partial x} dx)u\delta t + mdx \frac{\partial c}{\partial t} \delta t + dx \frac{\partial q}{\partial t} \delta t \quad (1-14)$$

in which  $c$  (mmol/mL) is the concentration of solution,  $u$  (mL/min) is the flow rate,  $x$  (g) is the mass of the adsorbent contained therein, indicating the distance from the input end of the fixed-bed column,  $q$  (mmol/mg) is the concentration of adsorbed material, and  $m$  (mL/g) is the free space or the pore volume of the adsorbent. Therefore,

$$\frac{\partial c}{\partial x} + \frac{m}{u} \frac{\partial c}{\partial t} + \frac{1}{u} \frac{\partial q}{\partial t} = 0 \quad (1-15)$$

For constant flow rate, the equation could be rewritten as,

$$\frac{\partial c}{\partial x} + m \frac{\partial c}{\partial V} + \frac{\partial q}{\partial V} = 0 \quad (1-16)$$

where  $V$  (mL) is the volume of the outflow.

Assuming that adsorption rate is determined by the chemical reaction, i.e. the diffusion is not a rate-determining factor, and equilibrium adsorption follows the Langmuir isotherm, and the adsorption obeys pseudo-second order reversible reaction kinetics, the expression of the Thomas model was obtained after a series of complicated derivation steps,

$$\frac{C_t}{C_0} \approx \frac{1}{1 + \exp\left[\frac{k_{Th}}{u}(Q_0 M - C_0 V_{eff})\right]} \quad (1-17)$$

where  $C_0$  (mg/L) is the initial concentration of adsorbate,  $C_t$  (mg/L) is the concentration of adsorbate in the effluent at time  $t$ ,  $k_{Th}$  (mL/mg min) is the Thomas rate constant,  $u$  (mL/min) is the flow rate,  $Q_0$  (mg/g) is the equilibrium adsorbate uptake on to a unit mass

of adsorbent,  $M$  (g) is the mass of adsorbent in fixed-bed column, and  $V_{eff}$  (mL) is the volume of treated solution at time  $t$ .

The Thomas model could be linearized to the following form:

$$\ln\left(\frac{C_0}{C_t} - 1\right) = \frac{k_{Th} Q_0 M}{u} - \frac{k_{Th} C_0 V_{eff}}{u} \quad (1-18)$$

Plotting  $\ln\left(\frac{C_0}{C_t} - 1\right)$  against  $V_{eff}$ ,  $k_{Th}$  and  $Q_0$  can be assessed by the slope and intercept.

The Thomas model is mainly used to predict the breakthrough curve and to estimate the maximum adsorption  $Q_0$ .

The Adams–Bohart model[57] is another widely applied model for fixed-bed column adsorption. Adams and Bohart proposed a relationship between  $C/C_0$  and  $t$  in a continuous flowing system for gas adsorption on carbon. It assumes that the rate-limiting step is a chemical reaction on the surface, and the adsorption process follows a pseudo second order irreversible reaction. The adsorption reaction rate is  $k_{AB}qc$ .

Considering a selected portion of adsorbent, the residual adsorption capacity decreases at a rate given by following equation,

$$\frac{\partial c}{\partial x} = -\frac{k_{AB}}{u} qc \quad (1-19)$$

where  $q$  is residual adsorption capacity (mg/L),  $c$  is the solution concentration at time  $t$  and the distance from inflow entrance  $x$  (m),  $u$  (m/min) is the superficial flow rate, and  $k_{AB}$  (mL/mg min) is the Adams-Bohart rate constant.



After integration, the linear form of the Adams-Bohart model can be written as:

$$\ln\left(\frac{C_0}{C_t} - 1\right) = \ln(e^{k_{AB}Q_0Z/u} - 1) - k_{AB}C_0t \quad (1-20)$$

where  $C_0$  (mg/L) is initial concentration of adsorbate,  $C_t$  (mg/L) is the concentration of adsorbate in the effluent at time  $t$ ,  $Q_0$  (mg/L) is the equilibrium adsorbate uptake on to a unit volume of adsorbent, and  $Z$  (m) is the height of the fixed-bed column. The Adams-Bohart model is mostly used to describe the initial part of the breakthrough curve in a fixed-bed column system. One advantage of the Adams-Bohart model is that it indicates the breakthrough time straightforwardly.

In addition to the Thomas model and the Adams-Bohart model, Yoon and Nelson developed a simple model to describe the adsorption of adsorbate gases on to activated charcoal in 1984[58]. They denoted  $Q$  as the probability of adsorption and  $P$  as the probability of breakthrough. In other words,  $Q$  is the concentration percentage of the inflow that gets adsorbed and  $P$  is the concentration percentage of the inflow that flows out of the column. This model assumed that the rate of decrease in the probability of adsorption for each adsorbate molecule is proportional to  $Q$  and  $P$ , shown as:

$$-\frac{dQ}{dt} = k_{YN}QP \quad (1-21)$$

Since  $P=1-Q$ , the following equation was obtained:

$$\int \frac{dQ}{Q} + \int \frac{dQ}{1-Q} = -\int k_{YN}dt \quad (1-22)$$

After integration, the equation became:

$$\ln\left(\frac{Q}{1-Q}\right) = k_{YN}(\tau - t) \quad (1-23)$$

where  $k_{YN}$  ( $\text{min}^{-1}$ ) is the rate constant and  $\tau$  is a constant. Noting that when  $Q=0.5$ ,  $\tau=t$ .

Therefore,  $\tau$  is the time required for 50% adsorbate breakthrough. Plugging  $Q = \frac{1-C_t}{C_0}$

into the equation, the linear form of the Yoon-Nelson model is expressed as:

$$\ln\left(\frac{C_t}{C_0 - C_t}\right) = k_{YN}t - \tau k_{YN} \quad (1-24)$$

The Yoon-Nelson model is always used to predict 50% adsorbate breakthrough time.

## Chapter 2 Methodology

### 2.1 Particle synthesis

#### 2.1.1 Materials

Low molecular weight chitosan (CAS #9012-76-4) and sodium tripolyphosphate (TPP) (CAS #7758-29-4, technical grade) were both purchased from Sigma-Aldrich (St. Louis, MO). The chitosan had a deacetylation fraction of 90.85% and molecular weight range of 50 to 190 kDa. More specifically, the acquired batch had a viscosity of 185 cP (for a concentration of 1 w/w in 1 w/w acetic acid solution) (all data provided by supplier). 99%+ Copper (II) sulfate pentahydrate was obtained from Acros Organics (CAS #7758-99-8). Water used for all experiments was acquired from a Milli-Q water system.

Sodium alginate (alginic acid, sodium salt, CAS #9005-38-3) was obtained from Acros Organics (Morris Plains, NJ). It had a molecular weight range of 450 to 550 kDa and a viscosity of 485 cP (for a 1% w/w solution) (data provided by supplier). Furthermore, the sodium alginate contained 65-75% guluronic acid (G) subunits and 25-35% mannuronic acid (M) subunits. Calcium chloride dihydrate FCC/USP (CAS #10035-04-8), sodium chloride (CAS #7647-14-5) and isooctane (CAS #540-84-1) were obtained from Fisher Scientific (Pittsburgh, PA). 1,6 dibromohexane (CAS #629-03-8) and Span-80 (CAS #1338-43-8) were purchased from Sigma-Aldrich (St. Louis, MO).

### **2.1.2 Preparation of chitosan nanoparticles**

The method of ionic gelation, where chitosan was ionically cross-linked with TPP, was used to synthesize the nanoparticles in dilute solution. Chitosan was dissolved in water with acetic acid 1.75 times the mass of chitosan to obtain 0.1 wt% (1 mg/ml) chitosan solution, 0.2 wt% (2 mg/mL) chitosan solution, or 0.4 wt% (4 mg/mL) chitosan solution for nanoparticle synthesis. TPP was dissolved in water to a concentration of 0.1 wt%, 0.2 wt%, and 0.4 wt%. In general, 1 mL of TPP was added dropwise to 5 mL of the chitosan solution of equal concentration under magnetic stirring to create a mixture of 5:1 volume ratio chitosan:TPP. The mixture was stirred further for 30 minutes before sitting an additional 24 hours to reach equilibrium. It was then centrifuged for 30 minutes at 48,400 g (20,000 rpm) (Avanti J-E, Beckman Coulter, Brea, CA). The wet mass of the collected particles produced from one batch ranged from 0.15g to 0.35g.

A smaller concentration of TPP was also used in the experiments for chitosan nanoparticles synthesized from the 2 mg/mL solution. 0.7 mL of TPP solution and 0.3 mL DI water were added to 5 mL of chitosan solution following the 5:1 volume ratio of chitosan:TPP solutions described above. These TPP-lean particles were produced in order to observe the effect of the degree of cross-linking on the properties of the nanoparticles and the resulting adsorption capability.

### **2.1.3 Preparation of calcium-alginate gel microbeads**

Three solutions were prepared: i) aqueous 2 wt% alginate solution; ii) an oil solution consisting of 69.5% (v/v) isooctane 29.5%(v/v) 1,6 dibromohexane and 1 wt% Span-80 surfactant; iii) calcium chloride solution with concentrations of 0.1M calcium chloride and 0.5 M sucrose in water. An emulsion was formed by blending equal weight amounts of the alginate solution with the oil solution at 20,000 rpm for 10 minutes (Ultra-Turrax T-25 blender, IKA Works, Staufen, Germany). The flask containing solutions was immersed in ice water during blending to prevent overheating of the mixture. The calcium chloride solution was added slowly immediately afterward to cross-link the alginate beads under magnetic stirring conditions. The emulsions were then separated in a separatory funnel with acetone washing. The alginate suspension was extracted and centrifuged at 6000 rpm at 4 °C. The supernatant was removed and the resulting pellets are collected as alginate beads. They were stored in DI water until sieving was performed. The alginate beads used in the experiments were smaller than 38  $\mu\text{m}$  in diameter.

### **2.1.4 Preparation of chitosan/alginate combination particles (weight ratio 1:0.45)**

The chitosan and alginate particles were prepared as mentioned previously. For the experiments, 2 mg/mL was selected as the chitosan synthesis concentration. The mass ratio of calcium-alginate gel microbeads to chitosan nanoparticles was 1:0.45. A small amount <2 mL of chitosan nanoparticle suspension in DI water was mixed with the

corresponding weight of alginate beads in a vial on a stir plate. When the mixture was equilibrated, the combination particles were centrifuged at 48,400 g for 20 minutes and then were ready to be used for adsorption experiments once the supernatant was removed.

### 2.1.5 Preparation of large calcium-alginate gel beads

Sodium alginate was dissolved in water at a concentration of 2 wt%. Sodium chloride was added into the 2 wt% alginate solution to make 0.2 M concentration in order to promote the formation of homogenous beads[59]. A bath of 0.1 M  $\text{CaCl}_2$  was prepared, and NaCl was also added to the bath to yield a 0.075 M concentration. Using a syringe pump equipped with a 5 cc syringe and a 30G 1/2 needle angled downward, the alginate solution was dropped into the bath of  $\text{CaCl}_2$  and NaCl solution from a height of 12 cm at a volumetric flow rate of 0.10 mL/min. The setup is shown in Figure 2-1. The bath was stirred manually and the beads were allowed to equilibrate for a minimum of 15 min to allow the cross-linking to complete. A vacuum pump was used to collect completed alginate gel beads. Subsequently, beads were stored in deionized water until being used.

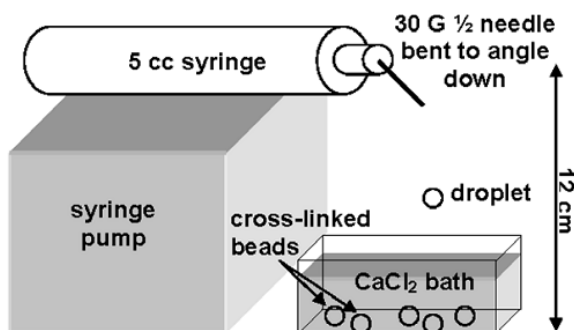


**Figure 2-1.** Schematic view of syringe pump, needle, and cross-linking bath for bead production.[40]

## **2.2 Particle characterization**

### **2.2.1 Zetasizing**

The size and zeta potential distributions of the chitosan nanoparticles were characterized. After the first centrifugation, the solids were suspended in water followed by sonication (Misonix 3000, Qsonica, Newtown, CT). The size analysis provided the size distribution of the nanoparticles. Dynamic light scattering was performed by a Malvern zetasizer model Nano ZS-90 (Malvern Instruments Ltd., Malvern, UK) to measure the size. Phase analysis light scattering was used to accomplish the zeta analysis. (From [www.malvern.com](http://www.malvern.com)) Zeta potential indicates the strength of electrostatic interparticle interactions. High zeta potentials confer stability, where the suspension resists aggregation.

### **2.2.2 TEM imaging**

The chitosan nanoparticles and chitosan/alginate combination particles were viewed with a TEM (Philips CM12, Andover, MA). 3 mL of 50mM copper sulfate solution was used as a stain solution and added to the particle pellet after centrifugation. The nanoparticles were sonicated to uniformity and soaked in copper sulfate solution for several days under magnetic stirring until equilibrium was reached and then were placed on to imaging grids (Cat. #FCF300-CU from Electron Microscopy Sciences, Hatfield, PA). The grids were

subjected to glow discharge treatment before sample loading in order to increase the hydrophilicity of the grid surface.

### **2.2.3 Laser diffraction**

Alginate microbead suspensions were analyzed using a Beckman-Coulter LS-13 320 Laser Diffraction apparatus. Samples were run for combined obscuration and polarization intensity differential scattering (PIDS) analysis. A refractive index of 1.37 was input for alginate, based on measurements of the refractive index of alginate slabs. The unit was thoroughly rinsed between samples; acetone or isopropyl alcohol was used if cleaning was required. Samples were stored in glass vials and sonicated before processing and analyzed immediately after processing.

### **2.2.4 Microscope imaging**

The large calcium-alginate gel beads were observed under an optical microscope using the Zeiss Axio Lab.A1. The image was recorded with AxioVision software under 5x magnification.



## 2.3 Equilibrium adsorption experiment

To obtain chitosan nanoparticles loaded with copper ions, 3 mL of copper sulfate solution (an excess amount used to favor adsorption) was added to the wet pellet obtained from centrifugation of the synthesized nanoparticles. According to the study by Schmuhl *et al.*, [4] the pH of the copper sulfate solution does not affect the adsorption capacity of chitosan nanoparticles when it is above 3.0. Therefore, the experimental pH was fixed at 3.5 in order to lie within the region of pH independence and also to avoid disturbance by copper hydroxide formation at high pH. The mixture was sonicated to uniformity in the same centrifuge tube and was left under magnetic stirring for one week. Then, the particles were centrifuged once again at 48,400 g (20,000 rpm) for 20-30 minutes. The resulting solid was then weighed and resuspended in 1 mL of water, to aid in its dissolution for the inductively coupled plasma mass spectrometer (ICP/MS) experiments described below. For calcium-alginate gel microbeads and combination particles, the process was the same except that a lower centrifuge speed of 10,000 rpm was used. For large calcium-alginate gel beads, the sonication and centrifuging steps could be skipped. After stirring for one week, the supernatant solution was poured out and 1 mL of DI water was added into the samples.

The mass of copper ions adsorbed to the chitosan nanoparticles and alginate beads was measured by inductively coupled plasma mass spectrometry (ICP/MS). The solids weighed between 8 and 300 mg and were digested in 50 mL conical (VWR Scientific, Radnor, PA) centrifuge tubes. To each tube, 2 mL of concentrated nitric acid were added

(EMD OmniTrace Ultra High Purity, VWR Scientific, Radnor, PA) and the samples were allowed to react at least overnight. After equilibrating the pressure, they were subsequently digested using a MARSX microwave sample digester (CEM Corp., Mathews, NC). A 300W power program was applied (Table 2-1).

**Table 2-1.** ICPMS procedure.

Step	Duty cycle	Heating time	Cooling time (approximate)
1.	75	5	10
2.	100	5	10
3.	100	5	20
4.	100	10	20

After digestion, samples were removed and cooled before the final dilution to 50 mL using DI water (MilliQ Ultrapure De-ionized, Millipore Corp., Billerica, MA) was made. To measure these samples in the optimum analytical concentration range they were re-diluted by a factor of 2857 in 5% OmniTrace nitric acid by volume.

Samples were analyzed for Cu using an X5 (Thermo Electron, MA) inductively coupled plasma mass spectrometer (ICP/MS). An  $m/z$  ratio of 65 was used for quantitation and no isobaric interferences were observed. ICP/MS precision is determined by many factors, including isotopic abundance that determines sensitivity, spectral background (molecular isobars), isobaric interference from concomitant elements and instrument drift. Taking into account all factors, when instrument drift is reasonable the uncertainty estimate for these samples analyzed for copper is roughly 8-12% RSD. For elements such as Ag with few molecular isobars and no concomitant elemental interferences, the precision can be as low as 0.5% for replicate measurements from a single sample and

within about 7% for a single sample measured throughout an analytical run. For samples requiring digestion/or dissolution the homogeneity of the sample and dissolved solids will also contribute to the overall reproducibility of the measurement.

## **2.4 Adsorption kinetics experiment**

Calcium-alginate gel microbeads, chitosan/alginate combination particles and large calcium-alginate gel beads were put into 15 mL test tubes, yielding 12 tubes with calcium-alginate gel microbeads, 12 tubes with chitosan/alginate combination particles, and 12 tubes with large calcium-alginate gel beads. Each tube contained around 0.2 g (wet mass) of particles. For calcium-alginate gel microbeads and chitosan/alginate combination particles, 3 mL of 1 mM copper sulfate solution was added into each tube, and then the samples were sonicated to uniformity in the same tube and left under magnetic stirring for 10, 20, 30, 40, 50, 70, 90, 120, 240, 360, 480 and 1440 minutes, respectively. Afterward, the samples were centrifuged at 48,400 g for 10 minutes. After removing the supernatant fluid, pellets were collected and weighed and then transferred to big centrifuge tubes. 1 mL of DI water was added to each centrifuge tube and the samples were sonicated again until all the particles were suspended uniformly in the centrifuge tubes. For large calcium-alginate gel beads, there was no need to centrifuge samples. After adding 3 mL of 1 mM copper sulfate solution into each tube, the samples were stirred on a magnetic stirring plate for 10, 20, 30, 40, 50, 70, 90, 120, 240, 360, 480 and 1440 minutes respectively. Then the solution was poured out. The large beads were

transferred to big centrifuge tubes and their mass was recorded. The amount of copper ions adsorbed on to the calcium-alginate gel microbeads, chitosan/alginate combination particles and large calcium-alginate gel beads were measured by inductively coupled plasma mass spectrometry (ICP/MS) at each time point.

## **2.5 Fixed-bed column experiment**

In this experiment, tube connectors with the same size ends were used as the fixed-bed columns. Since the wall of tube connectors is translucent, the color change of packed particles could be observed. After packing alginate gel beads into it, nylon meshes (Spectrum Laboratories, Inc. CA) were adhered by silicon glue onto both ends to trap particles inside. The pore size of the meshes is 300  $\mu\text{m}$  with 50% open area, and the thickness of the meshes is 200  $\mu\text{m}$ . It took 24 hours until the silicon glue was fully dried. To minimize possible wall and axial dispersion effects in the fixed-bed column, the bed length-to-particle diameter ratio must be greater than 20[60]. Two sizes of the column were used in the experiment. The large column has an internal diameter of 1/2 inch (1.27 cm) and column height of 6.4 cm, and the small column has internal diameter of 1/4 inch (0.635 cm) and column height of 4.8 cm. The diameter of the alginate beads was around 1 mm. Therefore, the bed length-to-particle diameter ratio for both large column and small column was greater than 20.

The solution containing 1mM  $\text{CuSO}_4$  was pumped into the fixed-bed column by a syringe pump (New Era Pump Systems, Farmingdale, NY) with volumetric flow rate varied at 0.1 mL/min, 0.25 mL/min and 1 mL/min. The setup was shown in Figure 2-2. To be consistent with equilibrium experiments, the pH of  $\text{CuSO}_4$  solution was fixed at 3.5. Adsorption experiments were carried out at room temperature. The outflow was sampled at 5 minutes, 10 minutes, 20 minutes, 30 minutes, 40 minutes, 60 minutes, 80 minutes, 120 minutes, 150 minutes, 180 minutes, 210 minutes, 240 minutes, 300 minutes, 360 minutes and 480 minutes. The copper ion concentration in collected liquid samples was tested by inductively coupled plasma mass spectrometry (ICP/MS).

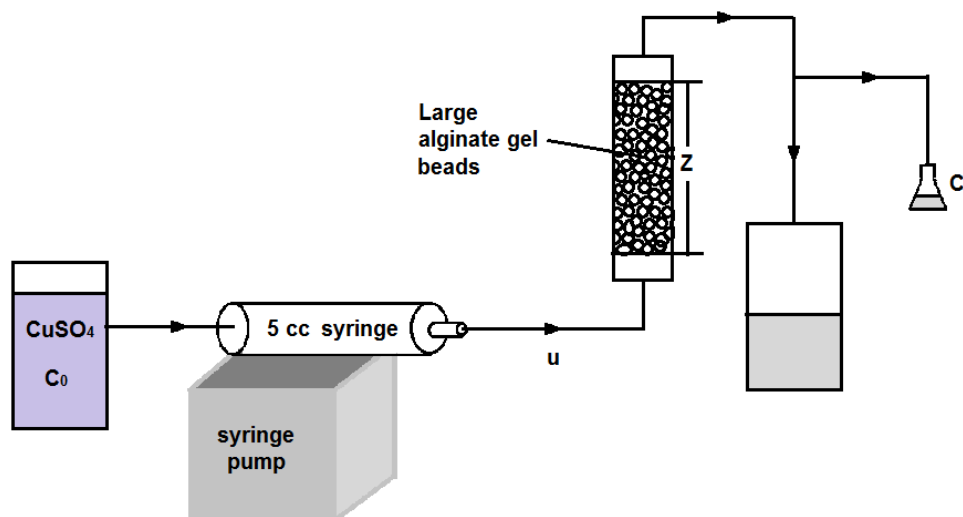


**Figure 2-2.** Schematic view of fixed-bed column experiment.

## **Chapter 3 Equilibrium Study of Copper Ion Adsorption by Chitosan Nanoparticles, Calcium-Alginate Gel Microbeads, Large Calcium-Alginate Gel Beads and Chitosan/Alginate Combination Particles**

### **3.1 Introduction**

Conventional methods to remove heavy metal ions from industrial effluents include adsorption, precipitation, filtration, and electrochemical treatment. Most of these methods are expensive and incapable of removing trace levels of heavy metal ions[1, 2]. Adsorption is an effective and economical separation process that could be employed in water purification. To evaluate an adsorbent, the equilibrium adsorption capability and affinity to adsorbate are the most important factors to consider. In recent years, much active research has been performed on novel adsorbents and has explored various configurations of adsorbents to maximize their adsorptive capacity, particularly incorporating nanoparticles. The unique advantages of nanoparticles are their small size, large surface area and the quantum size effect, which theoretically increases the adsorption capacity for nanoparticle adsorbents[3].

Natural carbohydrate biopolymers such as chitosan and alginate are receiving increasing attention due to their extraordinary affinity to heavy metal ions. Particularly in gel particle form, the uptake is comparable to or even beyond that of commercial ion exchange resins. In addition, the materials are abundant, biocompatible and

environmentally friendly, making them potential biosorbents for the removal of pollutants from wastewater [4-14].

In this chapter, chitosan gel nanoparticles, calcium-alginate gel beads, chitosan/alginate combination particles and large calcium-alginate gel beads were formed and characterized by zetasizing, TEM and microscope imaging. The equilibrium adsorption capability of chitosan nanoparticles, calcium-alginate gel beads, chitosan/alginate combination particles and large calcium-alginate gel beads for  $\text{Cu}^{2+}$  from copper sulfate solutions at fixed pH has been explored. Experimental data were fitted to the Langmuir isotherm and Freundlich isotherm equations, and the binding mechanisms were discussed.

## **3.2 Experimental methods**

### **3.2.1 Materials**

Low molecular weight chitosan (CAS #9012-76-4) and sodium tripolyphosphate (TPP) (CAS #7758-29-4, technical grade) were both purchased from Sigma-Aldrich (St. Louis, MO). The chitosan had a deacetylation fraction of 90.85% and molecular weight range of 50 to 190 kDa. More specifically, the acquired batch had a viscosity of 185 cP (for a concentration of 1 w/w in 1 w/w acetic acid solution) (all data provided by supplier).

99%+ Copper (II) sulfate pentahydrate was obtained from Acros Organics (CAS #7758-99-8). Water used for all experiments was acquired from a Milli-Q water system.

Sodium alginate (alginic acid, sodium salt, CAS #9005-38-3) was obtained from Acros Organics (Morris Plains, NJ). It had a molecular weight range of 450 to 550 kDa and a viscosity of 485 cP (for a 1% w/w solution) (data provided by supplier). Furthermore, the sodium alginate contained 65-75% guluronic acid (G) subunits and 25-35% mannuronic acid (M) subunits. Calcium chloride dihydrate FCC/USP (CAS #10035-04-8), sodium chloride (CAS #7647-14-5) and isooctane (CAS #540-84-1) were obtained from Fisher Scientific (Pittsburgh, PA). 1,6 dibromohexane (CAS #629-03-8) and Span-80 (CAS #1338-43-8) were purchased from Sigma-Aldrich (St. Louis, MO).

### **3.2.2 Preparation of particles**

#### **(1) Chitosan nanoparticles**

The method of ionic gelation, where chitosan was ionically cross-linked with TPP, was used to synthesize the nanoparticles in dilute solution. Chitosan was dissolved in water with acetic acid 1.75 times the mass of chitosan to obtain 0.1 wt% (1 mg/mL) chitosan solution, 0.2 wt% (2 mg/mL) chitosan solution, or 0.4 wt% (4 mg/mL) chitosan solution for nanoparticle synthesis. TPP was dissolved in water to a concentration of 0.1 wt%, 0.2 wt%, and 0.4 wt%. In general, 1 mL of TPP was added dropwise to 5 mL of the chitosan solution of equal concentration under magnetic stirring to create a mixture of 5:1 volume ratio chitosan:TPP. The mixture was stirred further for 30 minutes before sitting an



additional 24 hours to reach equilibrium. It was then centrifuged for 30 minutes at 48,400 g (20,000 rpm) (Avanti J-E, Beckman Coulter, Brea, CA). The wet mass of the collected particles produced from one batch ranged from 0.15g to 0.35g.

A smaller concentration of TPP was also used in the experiments for chitosan nanoparticles synthesized from the 2 mg/mL solution. 0.7 mL of TPP solution and 0.3 mL DI water were added to 5 mL of chitosan solution following the 5:1 volume ratio of chitosan:TPP solutions described above. These TPP-lean particles were produced in order to observe the effect of the degree of cross-linking on the properties of the nanoparticles and the resulting adsorption capability.

## (2) Calcium-alginate gel microbeads

Before synthesizing calcium-alginate gel microbeads, three solutions were prepared: i) aqueous 2 wt% alginate solution; ii) an oil solution consisting of 69.5% (v/v) isooctane 29.5%(v/v) 1,6 dibromohexane and 1 wt% Span-80 surfactant; iii) calcium chloride solution with concentrations of 0.1M calcium chloride and 0.5 M sucrose in water. An emulsion was formed by blending equal weight amounts of the alginate solution with the oil solution at 20,000 rpm for 10 minutes (Ultra-Turrax T-25 blender, IKA Works, Staufen, Germany). The flask containing solutions was immersed in ice water during blending to prevent overheating of the mixture. The calcium chloride solution was added slowly immediately afterward to cross-link the alginate beads under magnetic stirring conditions. The emulsions were then separated in a separatory funnel with acetone washing. The alginate suspension was extracted and centrifuged at 6000 rpm at 4 °C. The

supernatant was removed and the resulting pellets are collected as alginate beads. They were stored in DI water until sieving was performed. The alginate beads used in the experiments were smaller than 38  $\mu\text{m}$  in diameter.

### (3) Chitosan/alginate combination particles

To make chitosan/alginate combination particles, chitosan and alginate particles were prepared as mentioned previously. For the experiments, 2 mg/mL was selected as the chitosan synthesis concentration. The mass ratio of calcium-alginate gel microbeads to chitosan nanoparticles was 1:0.45. A small amount <2 mL of chitosan nanoparticle suspension in DI water was mixed with the corresponding weight of alginate beads in a vial on a stir plate. When the mixture was equilibrated, the combination particles were centrifuged at 48,400 g for 20 minutes and then were ready to be used for adsorption experiments once the supernatant was removed.

### (4) Large calcium-alginate gel beads

When making large calcium-alginate gel beads, sodium alginate was dissolved in water at a concentration of 2 wt%. Sodium chloride was added into the 2 wt% alginate solution to make 0.2 M concentration in order to promote the formation of homogenous beads[59]. A bath of 0.1 M  $\text{CaCl}_2$  was prepared, and NaCl was also added to the bath to yield a 0.075 M concentration. Using a syringe pump equipped with a 5 cc syringe and a 30G 1/2 needle angled downward, the alginate solution was dropped into the bath of  $\text{CaCl}_2$  and NaCl solution from a height of 12 cm at a volumetric flow rate of 0.10 mL/min. The setup is shown in Figure 2-1. The bath was stirred manually and the beads were allowed

to equilibrate for a minimum of 15 min to allow the cross-linking to complete. Vacuum pump was used to collect completed alginate gel beads. And beads were stored in deionized water until being used.

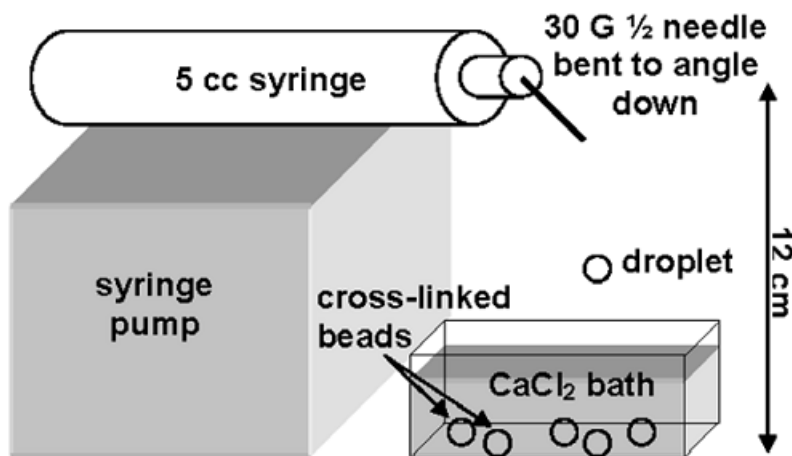


Figure 2-1. Schematic view of syringe pump, needle, and cross-linking bath for bead production.[40]

### 3.2.3 Particle characterization

The size and zeta potential distributions of the chitosan nanoparticles were characterized. After the first centrifugation, the solids were suspended in water followed by sonication (Misonix 3000, Qsonica, Newtown, CT). The size analysis provided the size distribution of the nanoparticles. Dynamic light scattering was performed by a Malvern zetasizer model Nano ZS-90 (Malvern Instruments Ltd., Malvern, UK) to measure the size. Phase analysis light scattering was used to accomplish the zeta analysis. (From [www.malvern.com](http://www.malvern.com)) Zeta potential indicates the strength of electrostatic interparticle

interactions. High zeta potentials confer stability, where the suspension resists aggregation.

The chitosan nanoparticles and chitosan/alginate combination particles were viewed with a TEM (Philips CM12, Andover, MA). 3 mL of 50mM copper sulfate solution was used as a stain solution and added to the particle pellet after centrifugation. The samples were sonicated to uniformity and soaked in copper sulfate solution for several days under magnetic stirring until equilibrium was reached and then were placed on to imaging grids (Cat. #FCF300-CU from Electron Microscopy Sciences, Hatfield, PA). The grids were subjected to glow discharge treatment before sample loading in order to increase the hydrophilicity of the grid surface.

Alginate microbead suspensions were analyzed using a Beckman-Coulter LS-13 320 Laser Diffraction apparatus. Samples were run for combined obscuration and polarization intensity differential scattering (PIDS) analysis. A refractive index of 1.37 was input for alginate, based on measurements of the refractive index of alginate slabs. The unit was thoroughly rinsed between samples; acetone or isopropyl alcohol was used if cleaning was required. Samples were stored in glass vials and sonicated before processing and analyzed immediately after processing.

The large calcium-alginate gel beads were observed under an optical microscope using the Zeiss Axio Lab.A1. Images were taken with AxioVision software under 5x magnification.

### 3.2.4 Equilibrium adsorption experiment

To obtain chitosan nanoparticles loaded with copper ions, 3 mL of copper sulfate solution (an excess amount used to favor adsorption) was added to the wet pellet obtained from centrifugation of the synthesized nanoparticles. According to the study by Schmuhl *et al.*, [4] the pH of the copper sulfate solution does not affect the adsorption capacity of chitosan nanoparticles when it is above 3.0. Therefore, the experimental pH was fixed at 3.5 in order to lie within the region of pH independence and also to avoid disturbance by copper hydroxide formation at high pH. The mixture was sonicated to uniformity in the same centrifuge tube and was left under magnetic stirring for one week. Then, the particles were centrifuged once again at 48,400 g (20,000 rpm) for 20-30 minutes. The resulting solid was then weighed and resuspended in 1 mL of water, to aid in its dissolution for the inductively coupled plasma mass spectrometer (ICP/MS) experiments described below. For alginate beads, the process was the same except that a lower centrifuge speed of 10,000 rpm was used. For large calcium-alginate gel beads, the sonication and centrifuging steps could be skipped. After stirring for one week, the supernatant solution was poured out and 1 mL of DI water was added into samples.

The mass of copper ions adsorbed to the chitosan nanoparticles and alginate beads was measured by inductively coupled plasma mass spectrometry (ICP/MS). The solids weighed between 8 and 300 mg and were digested in 50 mL conical (VWR Scientific, Radnor, PA) centrifuge tubes. To each tube, 2 mL of concentrated nitric acid were added (EMD OmniTrace Ultra High Purity, VWR Scientific, Radnor, PA) and the samples were

allowed to react at least overnight. After equilibrating the pressure, they were subsequently digested using a MARSX microwave sample digester (CEM Corp., Mathews, NC). A 300W power program was applied (Table 2-1).

**Table 2-1.** ICPMS procedure.

Step	Duty cycle	Heating time	Cooling time (approximate)
1.	75	5	10
2.	100	5	10
3.	100	5	20
4.	100	10	20

After digestion, samples were removed and cooled before the final dilution to 50 mL using DI water (MilliQ Ultrapure De-ionized, Millipore Corp., Billerica, MA) was made. To measure these samples in the optimum analytical concentration range they were re-diluted by a factor of 2857 in 5% OmniTrace nitric acid by volume.

Samples were analyzed for Cu using an X5 (Thermo Electron, MA) inductively coupled plasma mass spectrometer (ICP/MS). An  $m/z$  ratio of 65 was used for quantitation and no isobaric interferences were observed. ICP/MS precision is determined by many factors, including isotopic abundance that determines sensitivity, spectral background (molecular isobars), isobaric interference from concomitant elements and instrument drift. Taking into account all factors, when instrument drift is reasonable the uncertainty estimate for these samples analyzed for copper is roughly 8-12% RSD. For elements such as Ag with few molecular isobars and no concomitant elemental interferences, the precision can be as low as 0.5% for replicate measurements from a single sample and

within about 7% for a single sample measured throughout an analytical run. For samples requiring digestion/or dissolution the homogeneity of the sample and dissolved solids will also contribute to the overall reproducibility of the measurement.

### **3.3 Results and discussion**

#### **3.3.1 Particle Characterization**

##### *(1) Size*

The size of chitosan nanoparticles, as represented by the Z-average diameter, was measured by dynamic light scattering and is shown in Figure 3-1. Comparing the data from chitosan nanoparticles prepared with 5.0 mL of 1 mg/mL, 2 mg/mL and 4 mg/mL chitosan solutions and 1.0 mL TPP solution at an equal concentration, 4 mg/mL chitosan nanoparticles have the largest size while 1 mg/mL chitosan nanoparticles have the smallest. Also, for each synthesis concentration, the size of chitosan nanoparticles increases slightly with the amount of TPP added.

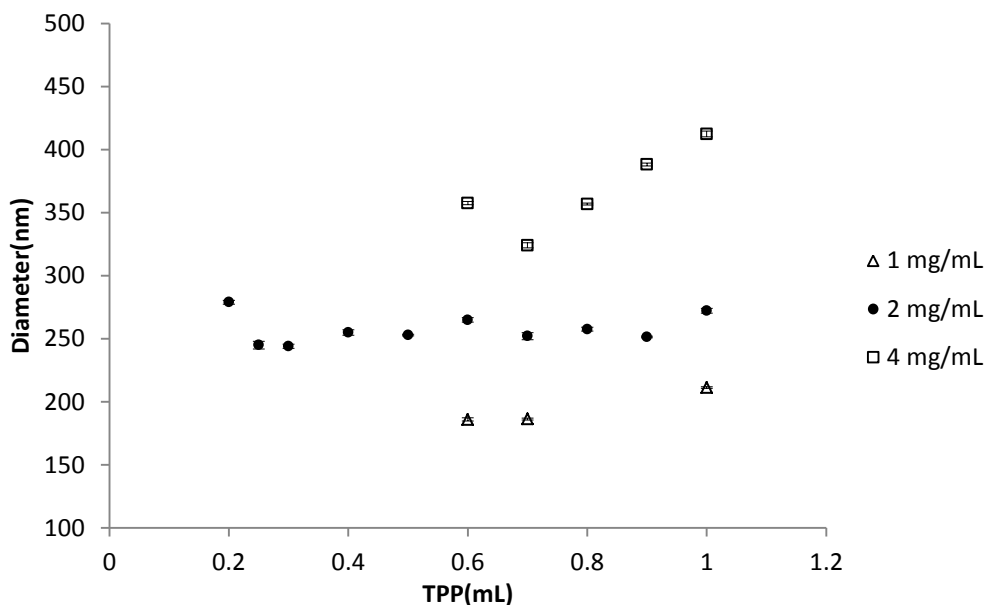


**Figure 3-1.** Diameter of chitosan nanoparticles produced at three synthesis solution concentrations (1 mg/mL, 2 mg/mL and 4 mg/mL, prepared with varying amounts of TPP).

The size distribution of the alginate microbeads was characterized by laser diffraction spectroscopy (Beckman Coulter LS-13 320). Figure 3-2 shows the size distribution of the microbeads, measured by laser diffraction spectroscopy. For the majority of the alginate microbeads, the diameter ranges from 12 - 33  $\mu\text{m}$ , with an average diameter of  $23 \pm 13 \mu\text{m}$ . According to optical microscope images we acquired, most calcium-alginate gel microbeads have roughly spherical shapes.



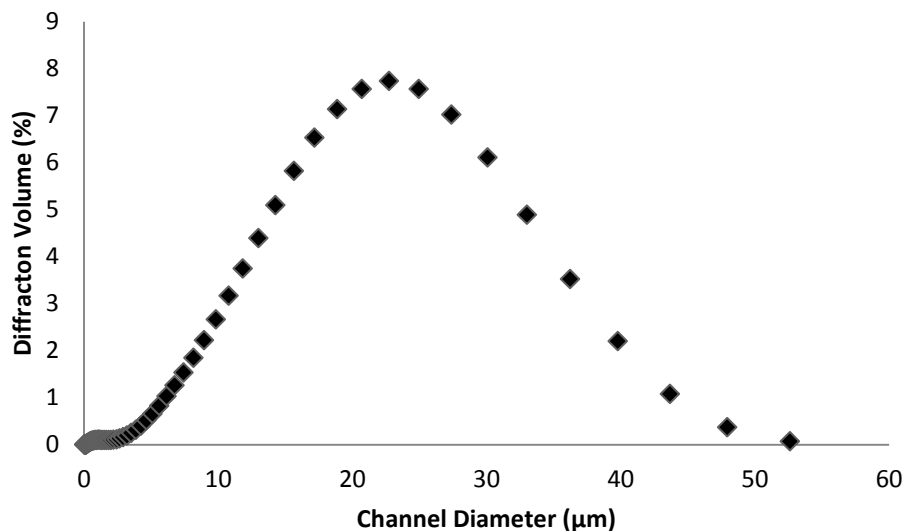


**Figure 3-2.** Size distribution of alginate microbeads measured by laser diffraction spectroscopy.

## (2) Zeta potential

Figure 3-3 reveals the zeta potential of different types of chitosan nanoparticles. Following the same trend as for the particle size, 4 mg/mL chitosan nanoparticles have the highest zeta potential while 1 mg/mL chitosan nanoparticles have the lowest. The zeta potential is related to the surface charge density and high magnitude of zeta potential denotes stability of the nanoparticles in suspension. For chitosan nanoparticles, the positive zeta potential results from the presence of protonated amine groups. When negatively charged TPP reacts with positively charged chitosan, the net zeta potential decreases. Therefore, the higher the zeta potential, the lower the fraction of TPP present in the nanoparticle. Zeta potential results suggest that the fraction of TPP present in the nanoparticle decreases as the synthesis solution concentration increases from 1 mg/mL to 4 mg/mL. TPP can form up to five links with amine groups on the chitosan, and the average number of links may also vary with the synthesis solution concentration. The

zeta potential of chitosan nanoparticles increases with the amount of TPP added and then decreases, where the chitosan/TPP ratio with the maximum zeta potential depends on the synthesis solution concentration. It is believed that these results arise from differences in the cross-linking reaction rate and degree of cross-linking as the concentration is varied.

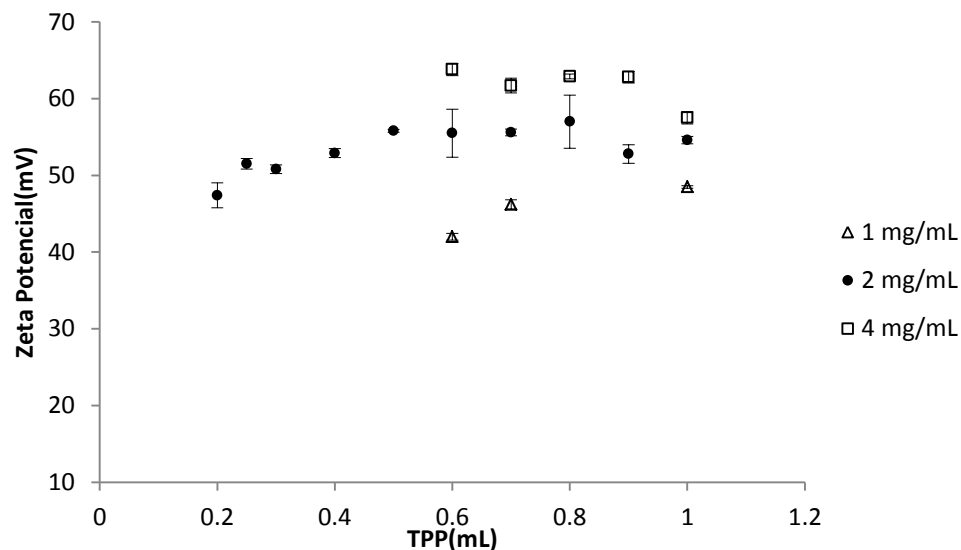


**Figure 3-3.** Zeta potential of chitosan nanoparticles produced at three synthesis solution concentrations (1 mg/mL, 2 mg/mL and 4 mg/mL prepared with varying amounts of TPP).

### (3) Imaging

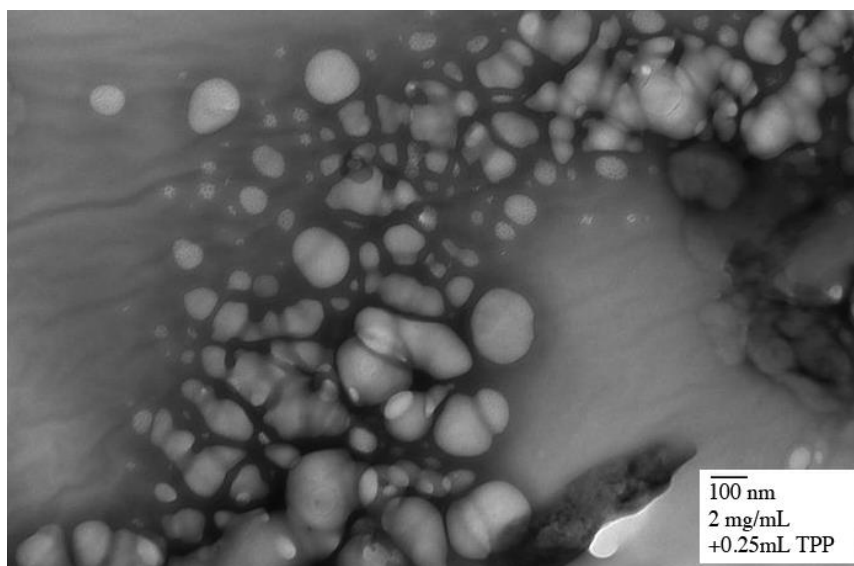
To further confirm the size and spherical shape of the chitosan nanoparticles, TEM images were acquired in this research.

Figure 3-4,

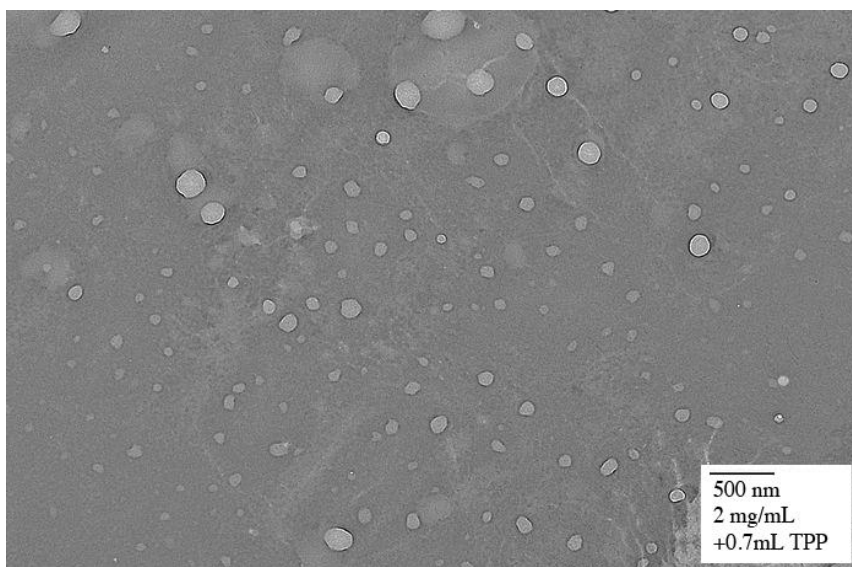
Figure 3-5 and

Figure 3-6 present TEM images of 2 mg/mL chitosan nanoparticles prepared with 0.25 mL TPP, 0.7 mL TPP and 1.0 mL TPP, respectively. Most nanoparticles exhibit a spherical shape without aggregation and their diameter ranges from 20 nm to 240 nm. By analyzing these images, the number weighted diameter, volume weighted diameter and intensity weighted diameter are obtained and listed in

Table 3-1. In general, the values are smaller than the Z-average diameters obtained by zetasizing. The difference is attributed to the presence of nanoparticle aggregates suspended in the samples for zetasizing but flowing off of the TEM grids without adhesion.



**Figure 3-4.** TEM image of chitosan nanoparticles prepared with 2 mg/mL chitosan solution and 0.25 mL TPP, stained with copper sulfate solution. Diameter range: approximately 18 - 244 nm.



**Figure 3-5.** TEM image of chitosan nanoparticles prepared with 2 mg/mL chitosan solution and 0.7 mL TPP, stained with copper sulfate solution. Diameter range: approximately 36 - 240 nm.

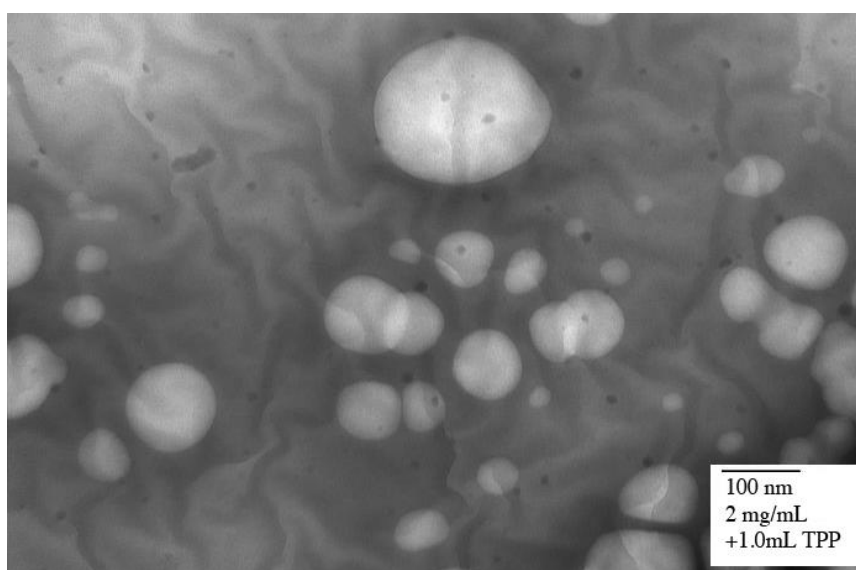
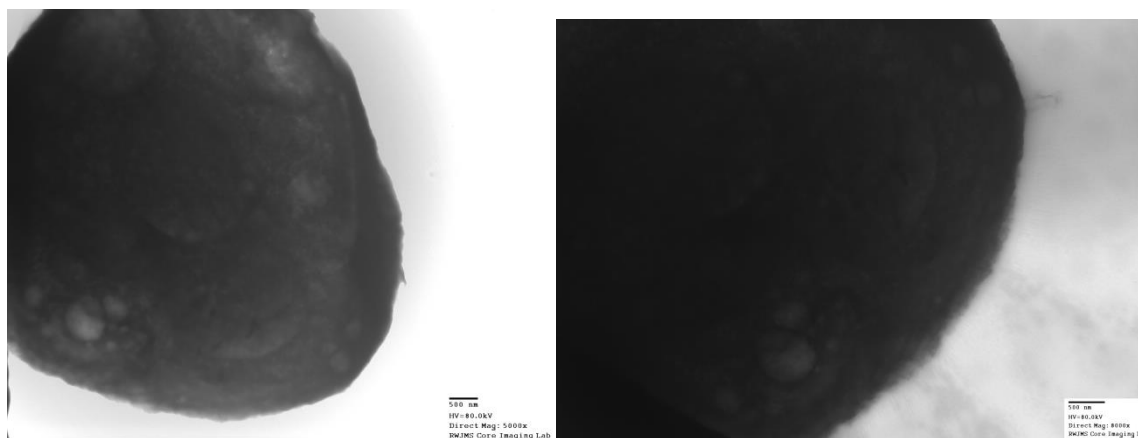


**Figure 3-6.** TEM image of chitosan nanoparticles prepared with 2 mg/mL chitosan solution and 1.0 mL TPP, stained with copper sulfate solution. Diameter range: approximately 28 - 226 nm.

**Table 3-1.** Number weighted diameter, volume weighted diameter, intensity weighted diameter and Z-average diameter of chitosan nanoparticles prepared with 2 mg/mL chitosan solution and 0.25 mL TPP, 0.7 mL TPP and 1.0 mL TPP, respectively.

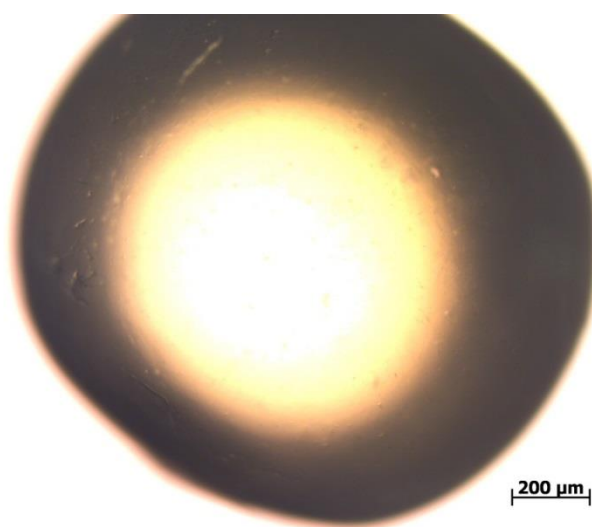
Concentration	Number weighted Diameter	Volume Weighted Diameter	Intensity Weighted Diameter	Z-Average Diameter
2 mg/mL (0.25 mL TPP)	72.9	149.2	195.5	245
2 mg/mL (0.7 mL TPP)	80.5	163.6	223.7	252.1
2 mg/mL (1.0 mL TPP)	85.6	148.9	209.5	272.3

Figure 3-7 exhibits TEM images of calcium-alginate gel microbeads coated with 2 mg/mL chitosan nanoparticles prepared with 0.7 mL TPP. The mass ratio of calcium-alginate gel microbeads to chitosan nanoparticles is 1:0.45. The approximate diameter of the calcium-alginate gel microbead shown in the images is measured at 9  $\mu\text{m}$ . The images show that the chitosan nanoparticles attached to the calcium-alginate gel microbeads evenly but did not fully cover the entire surface. Based on the mass ratio and incomplete surface coverage, the combination particles are expected to have a strongly negative charge of only slightly lower magnitude than that of the alginate microbeads alone. Although the alginate microbeads studied here are too large for zeta potential measurements to be obtained by zetasizing instruments, alginate nanoparticles typically exhibit values of approximately -30 mV [61].



**Figure 3-7.** TEM images of calcium-alginate gel microbeads coated with chitosan nanoparticles prepared with 2 mg/mL chitosan solution and 0.7 mL TPP, stained with copper sulfate solution. The weight ratio of calcium-alginate gel microbeads to chitosan nanoparticles is 1:0.45.

Figure 3-8 exhibits a microscope image of a large calcium-alginate gel bead under 5x magnification. From the image it can be seen that the large calcium-alginate gel bead has a spherical shape, and the approximate diameter of the large calcium-alginate gel bead shown in the image is around 1 mm.



**Figure 3-8.** Microscope image of a large calcium-alginate gel bead at 5x magnification.

### 3.3.2 Particle adsorption capability

It is important to correlate equilibrium adsorption data between metal ions and particles in order to assess the particles' capacity for metal adsorption. The effectiveness of adsorbents is often evaluated by fitting experimental adsorption data with the Langmuir and Freundlich isotherm equations, which relate  $Q$  (mg/g), the quantity of metal adsorbed per unit mass of adsorbent, to  $C_e$ (mg/L), the equilibrium metal ion concentration in the solution after adsorption.

The Langmuir model [50] is the best known and most widely applied adsorption isotherm. It has excellent agreement with a wide variety of experimental data and is represented as follows:

$$Q = \frac{Q_{\max} K_s C_e}{1 + K_s C_e} \quad (3-1)$$

The linear form of the Langmuir isotherm can be described as:

$$\frac{C_e}{Q} = \frac{C_e}{Q_{\max}} + \frac{1}{Q_{\max} K_s} \quad (3-2)$$

where  $Q_{\max}$  (mg/g) is the maximum adsorption capacity of adsorbent at monolayer coverage, and  $K_s$  (L/mg) is the Langmuir adsorption equilibrium constant related to the affinity of adsorptive sites for adsorbate at dilute concentration. This constant corresponds to the initial slope of the isotherm curve. The Langmuir isotherm assumes that the adsorption layer is a monolayer and the adsorption occurs at specific homogeneous adsorption sites resulting in an identical energy of adsorption at each site.

It is also assumed that the intermolecular attractive force decreases rapidly with the distance from the adsorption sites.

The Freundlich isotherm [51] predicts that the adsorption capacity of the adsorbent increases as a power law with an increase in adsorbate concentration. It is usually applied to multilayer adsorption and assumes an exponentially decaying distribution of the energy of adsorption sites. The Freundlich isotherm is an empirical equation presented as:

$$Q = K_F C_e^{\frac{1}{n}} \quad (3-3)$$

The linear form of the Freundlich equation can be expressed as:

$$\log Q = \frac{1}{n} \log C_e + \log K_F \quad (3-4)$$

where  $K_F$  and  $n$  are Freundlich constants. The value of  $1/n$  indicates the adsorption intensity. Moreover, adsorption sites become more heterogeneous on the surface as the value of  $1/n$  approaches zero.

The equilibrium adsorptive capability of chitosan nanoparticles and calcium-alginate gel microbeads for  $\text{Cu}^{2+}$  from copper sulfate solutions was investigated through adsorption isotherms whose parameters include  $Q$  (mg/g), the quantity of  $\text{Cu}^{2+}$  adsorbed per unit mass of adsorbent, and  $C_e$  (mg/L), the equilibrium  $\text{Cu}^{2+}$  concentration in the solution after adsorption.

The experimental data  $Q$  and  $C_e$  of 2 mg/mL chitosan nanoparticles prepared with 1.0 mL TPP or 0.7 mL TPP and 4 mg/mL chitosan nanoparticles prepared with 1.0 mL TPP in



the low  $\text{Cu}^{2+}$  concentration region (0.5-50 mM) are plotted in Figure 3-9. It was observed that the adsorption capabilities of all of the chitosan nanoparticles increase rapidly when the equilibrium solution concentration of  $\text{Cu}^{2+}$  is dilute and then reach maximum values. The Langmuir coefficients fit from the experimental data are shown in Table 3-2, along with the swelling ratio of the particles (ratio of wet mass to dry mass). It is worthy to notice that the swelling ratio of calcium-alginate microbeads did not indicate the total amount of water contained inside the microbeads, since there is water trapped between particles after centrifuge. The high correlation coefficients confirm that the Langmuir adsorption equation can be considered an accurate model of the adsorption behavior for all of the chitosan nanoparticles in the low concentration region.

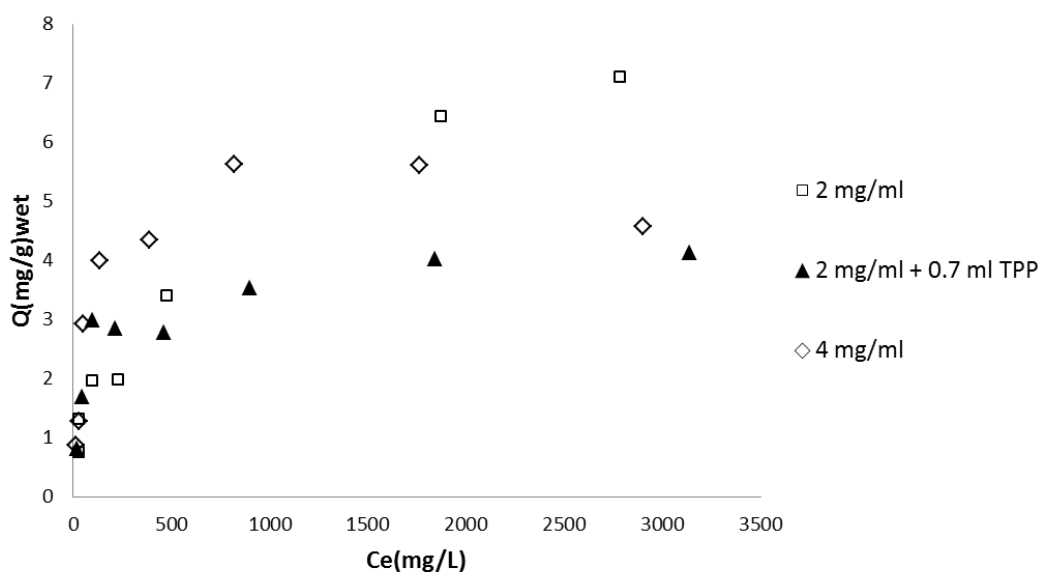


**Figure 3-9.** Adsorption isotherms of chitosan nanoparticles prepared with 2 mg/mL chitosan solution and 1.0 mL TPP or 0.7 mL TPP, and chitosan nanoparticles prepared with 4 mg/mL chitosan solution and 1.0 mL TPP in the low  $\text{Cu}^{2+}$  concentration region (0.5-50 mM).

The adsorption capability of calcium-alginate gel microbeads and large calcium-alginate gel beads were compared with that of chitosan nanoparticles in Figure 3-10 and Table 3-2. The high correlation coefficient in Table 3-2 confirms that the Langmuir adsorption equation can be applied to adsorption isotherms for calcium-alginate gel microbeads and large calcium-alginate gel beads in the low concentration region as well. The figure and table illustrate that the adsorption isotherms of calcium-alginate gel microbeads and large calcium-alginate gel beads have a similar trend to those of chitosan nanoparticles, and both calcium-alginate gel microbeads and large calcium-alginate gel beads have a significantly greater maximum adsorption capability value than all types of chitosan nanoparticles examined, and calcium-alginate gel microbeads have higher maximum adsorption capability value than large calcium-alginate gel beads.

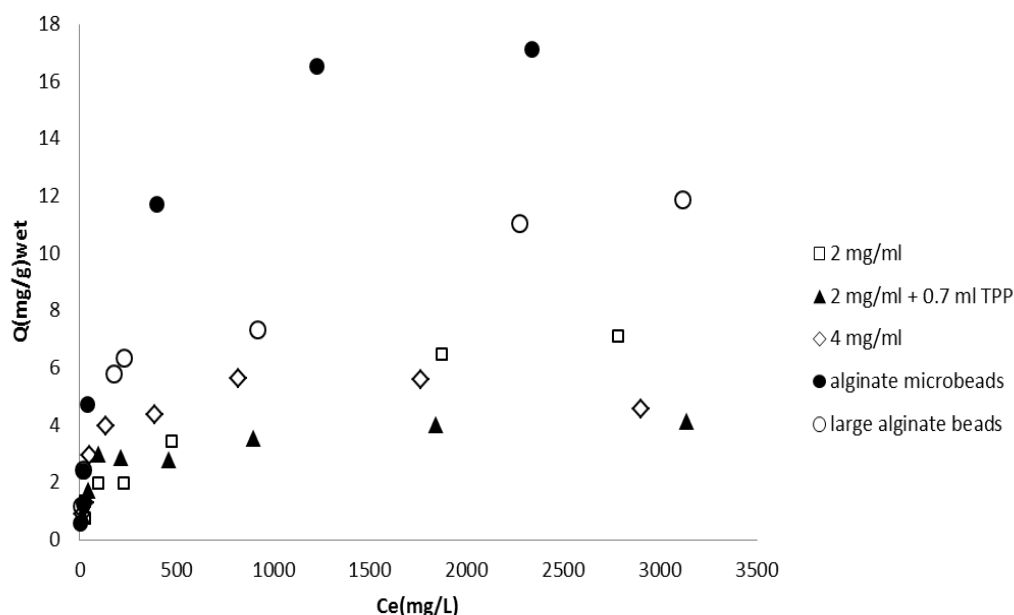


**Figure 3-10.** Adsorption isotherms of 2 mg/mL chitosan nanoparticles prepared with 1.0 mL TPP and 0.7 mL TPP, 4 mg/mL chitosan nanoparticles prepared with 1.0 mL TPP, calcium-alginate gel microbeads and large calcium-alginate gel beads in the low  $\text{Cu}^{2+}$  concentration region (0.5-50 mM).

In addition, the experimental data  $Q$  and  $C_e$  are plotted as specific adsorption ( $C_e/Q$ ) against the equilibrium concentration ( $C_e$ ) in Figure 3-11, in which all adsorption isotherms display linear behavior as expected. Since the presence of high proportions of water in chitosan nanoparticles, calcium-alginate gel microbeads and large calcium-alginate gel beads may affect the value of  $Q_{max}$ , the maximum quantity of  $\text{Cu}^{2+}$  adsorbed per unit mass of adsorbent,  $Q_{max}$  is calculated based on both wet mass and dry mass and presented in Table 3-2.  $K_s$  and correlation coefficients are independent of the adsorbent mass and are also shown in Table 3-2. All of the calculated  $Q_{max}$  (wet) values are consistent with the experimental maximum adsorption capability data.

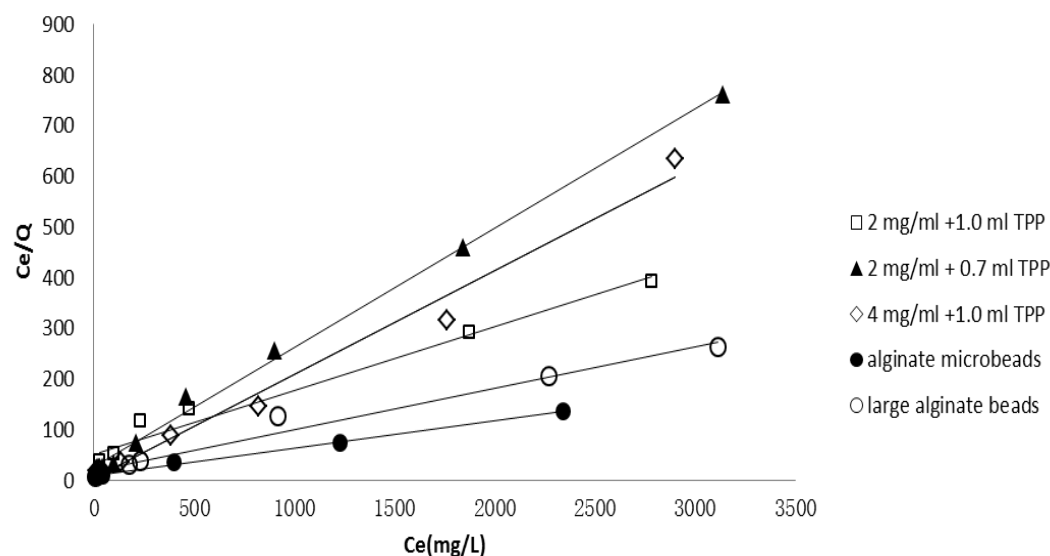


**Figure 3-11.** Linear adsorption isotherms of chitosan nanoparticles prepared with 2 mg/mL chitosan solution and 1.0 mL TPP or 0.7 mL TPP, chitosan nanoparticles prepared with 4 mg/mL chitosan solution and 1.0 mL TPP, calcium-alginate gel microbeads and large calcium-alginate gel beads in the low  $\text{Cu}^{2+}$  concentration region (0.5–50 mM). The lines shown are Langmuir equation fits to the data.

**Table 3-2.** Swelling ratio,  $Q_{\max}$  (calculated based on both wet mass and dry mass),  $K_s$  and correlation coefficients of chitosan nanoparticles prepared with 2 mg/mL chitosan solutions and 1.0 mL TPP or 0.7 mL TPP, chitosan nanoparticles prepared with 4 mg/mL chitosan solution and 1.0 mL TPP, calcium-alginate gel microbeads and large calcium-alginate gel beads in the low  $\text{Cu}^{2+}$  concentration region (0.5-50 mM).

	Swelling ratio	$Q_{\max}$ wet (mg/g)	$Q_{\max}$ dry (mg/g)	$K_s$ (L/mg)	$R^2$
<b>2mg/mL (1.0 TPP)</b>	14.14	7.93	112.36	0.0025	0.9684
<b>2mg/mL (0.7 TPP)</b>	18.44	4.24	78.13	0.0088	0.9966
<b>4mg/mL (1.0 TPP)</b>	12.00	4.87	58.48	0.0740	0.9853
<b>alginate microbeads</b>	16.53	18.32	303.03	0.0063	0.9967
<b>large calcium-alginate beads</b>	13.33	12.17	162.27	0.0048	0.9775

According to the experimental data, the maximum adsorption capacity  $Q_{\max}$  varies with the synthesis concentration of chitosan nanoparticles. 2 mg/mL chitosan nanoparticles prepared with 1.0 mL TPP have the highest adsorption capacity among the three types of chitosan nanoparticles in the experimental low concentration region. The fact that 2 mg/mL chitosan nanoparticles prepared with 0.7 mL TPP have smaller adsorption capacity than the nanoparticles with more cross-linking is illuminated by Ngah's study, which identified a potential new site in chitosan cross-linked with TPP for the adsorption of copper [62]. The copper ion forms a complex with the deprotonated phosphate group on the TPP, according to infrared spectroscopy measurements. The presence of an additional adsorption site on the TPP would mean that cross-linking, which attaches on the functional amine group, would not reduce the uptake of copper as significantly as initially expected.

Another noticeable trend among the values in Table 3-2 is the correlation of higher adsorption affinity coefficient  $K_s$  with a lower amount of TPP per unit mass of the

nanoparticles. The value of  $K_s$  increases by a factor of three or four when only 0.7 mL TPP is added to the 2 mg/mL chitosan solution during synthesis instead of 1 mL TPP.  $K_s$  increases by almost a factor of 30 between 2 mg/mL and 4 mg/mL chitosan nanoparticles, where the 4 mg/mL nanoparticles have a consistently higher zeta potential. The higher zeta potential for the 4 mg/mL nanoparticles arises due to a larger number of protonated amine groups per unit mass, which suggests that a smaller ratio of negatively charged TPP to positively charged chitosan is present in the 4 mg/mL nanoparticles compared to the 2 mg/mL nanoparticles. The association of binding affinity with a lower proportion of TPP suggests that the amine groups on the chitosan have higher affinity for the  $\text{Cu}^{2+}$  ions and are the preferred adsorption sites compared with the phosphate groups on the TPP.

Moreover, although 4 mg/mL chitosan nanoparticles have the highest affinity for  $\text{Cu}^{2+}$  in very dilute concentration among all chitosan nanoparticles and alginate gel beads, they also have the lowest adsorption capacity. This interesting phenomenon can be explained by the “pore-blockage” mechanism, which suggests that metal ions with a high affinity for adsorption sites do not completely penetrate the particles. Rorrer and Hsien described a situation where cadmium ions adsorb on or near the surface of the nanoparticle but were not able to fully penetrate the nanoparticle interior [32]. The cadmium ions occupied the amine sites on the surface and blocked further penetration into the particle due to the accumulation of metal ions at the surface. In this case, it is likely that  $\text{Cu}^{2+}$  ions are adsorbed on to the surface of 4 mg/mL chitosan nanoparticles in the low concentration region very quickly because of their strong binding affinity, and then the

diffusion of  $\text{Cu}^{2+}$  slows down significantly due to the large diameter of the nanoparticles and the repulsion from other adsorbed ions. When the  $\text{Cu}^{2+}$  adsorption approaches equilibrium, adsorption sites inside the 4 mg/mL chitosan nanoparticles may not be fully occupied.

In addition, the experimental data indicates that calcium-alginate microbeads have higher maximum adsorption capacity and affinity for  $\text{Cu}^{2+}$  in very dilute concentration than large calcium-alginate beads. This observation likely arises from their different degrees of cross-linking. Comparing the synthesis processes, the calcium-alginate microbeads were made from an emulsion, so that the alginate was dispersed well inside a droplet and reacted with calcium chloride cross-linker sufficiently during slow, dropwise addition, while the large calcium-alginate beads were synthesized by droplets falling into a calcium chloride bath, where only the surface of the droplets contacted with calcium chloride directly and cross-linking was rapid. Once cross-linking occurred, the outer layer of the large alginate beads became a gel network and increased diffusion resistance to calcium chloride. Therefore, the overall cross-linking degree of large calcium-alginate gel beads is lower than that of alginate microbeads, leading to relatively smaller amount of adsorption sites compared to alginate microbeads, since the copper ion adsorption mechanism for alginate is ion exchange. Moreover, the adsorption sites exposed on the microbeads' surface are a higher fraction of all the sites than the sites on the large calcium-alginate beads' surface because of their micro-scale size (high surface to volume ratio), resulting in the fact that the calcium-alginate gel microbeads have higher affinity for  $\text{Cu}^{2+}$  in very dilute concentration than large calcium-alginate gel beads.

Compared with literature values [8-10] listed in Table 3-3, chitosan nanoparticles cross-linked with TPP are found to be comparable and competitive with other forms of chitosan particles and microparticles including those synthesized from chemically modified chitosan. It was initially assumed that the nanoparticles' large surface area would allow an increased equilibrium adsorption capacity for metal ions. Based on the  $Q_{max}$  values obtained from the Langmuir isotherm, nanoparticles exhibit a minor increase in equilibrium adsorption capacity over the previously mentioned chitosan derivatives. Instead, the adsorption kinetics may be the property most affected by the nanoscale dimensions of the particles, and time-dependent measurements are currently underway.

**Table 3-3.** Literature values for equilibrium adsorption capacity of compared with the results of this study.

Source	Form	$Q_{max}$ (dry) (mg/g)	pH	Size
Findon <i>et al.</i> , 1993 [8]	Raw flakes	38.4	4.2	
Ng <i>et al.</i> , 2002 [9]	Raw flakes	77.6	3.5	
Ngah <i>et al.</i> , 2002 [10]	Cross-linked beads	59.7	6	< 250 $\mu$ m
This study	2 mg/mL (0.7 mL TPP)	78.1	3.5	~ 200 nm
	2 mg/mL (1.0 mL TPP)	112.4		
	4 mg/mL	58.5		

In the high concentration region (50mM-1M), adsorption isotherms of both chitosan nanoparticles and calcium-alginate gel microbeads present similar linearly increasing behavior, as presented in Figure 3-12, which is very different from the trends observed in dilute copper sulfate solution, and cannot be described by the Langmuir model.

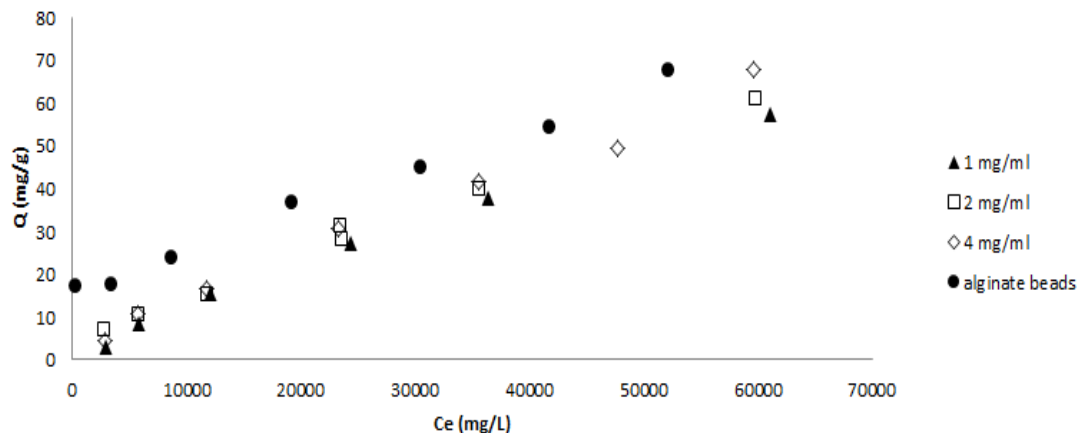


**Figure 3-12.** Adsorption isotherms of chitosan nanoparticles prepared with 1 mg/mL, 2 mg/mL or 4 mg/mL chitosan solutions and 1.0 mL TPP, and calcium-alginate gel microbeads in the high  $\text{Cu}^{2+}$  concentration region (50 mM-1M). The lines represent linear curve fits to the data.

However, the Freundlich model fits the adsorption isotherms of both chitosan nanoparticles and calcium-alginate gel microbeads in the high concentration regime very well, with all correlation coefficients close to 0.99. Figure 3-13 illustrates the linear form of the Freundlich isotherm.  $K_F$ ,  $1/n$  and correlation coefficients are calculated and exhibited in Table 3-4. The values of  $1/n$  indicate that the adsorption intensity of chitosan nanoparticles, especially of 1 mg/mL chitosan nanoparticles, is stronger than that of calcium-alginate gel microbeads. In addition, the adsorption sites on chitosan nanoparticles are relatively more homogeneous than on calcium-alginate gel microbeads in the high concentration region. Both chitosan nanoparticles and calcium-alginate gel microbeads exhibit unusual adsorption behavior in the high concentration region, since the Freundlich model is usually applied to extremely dilute systems in the literature. It is likely that in addition to chemisorption, physisorption occurs when the concentration of copper ions in the solution is high. More ions may bind to existing complexes or there may be mild precipitation on the chitosan. The high concentration regime is not studied



as often as the low concentration regime, and therefore the adsorption behavior is not as well established.

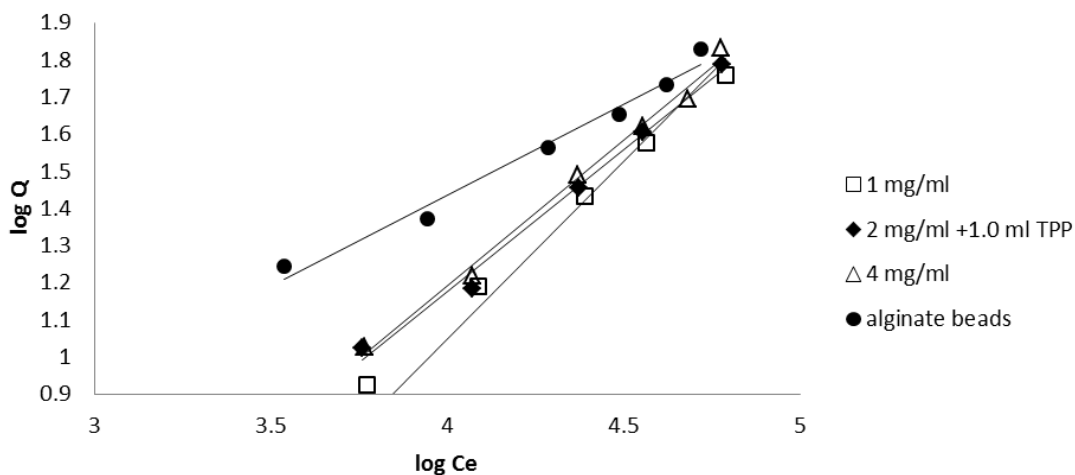


**Figure 3-13.** Linear adsorption isotherms of chitosan nanoparticles prepared with 1 mg/mL, 2 mg/mL or 4 mg/mL chitosan solutions and 1.0 mL TPP, and calcium-alginate gel microbeads in the high  $\text{Cu}^{2+}$  concentration region (50 mM-1M). The lines shown are Freundlich equation fits to the data.

**Table 3-4.**  $K_F$ ,  $1/n$  and correlation coefficients of linear Freundlich adsorption isotherms for 1 mg/mL, 2 mg/mL, 4 mg/mL chitosan nanoparticles and calcium-alginate gel microbeads in the high  $\text{Cu}^{2+}$  concentration region (50 mM-1M).

	$K_F$ [mg/g (mg/L) <sup>n</sup> ]	1/n	$R^2$
1 mg/mL	0.0017	0.9568	0.9790
2 mg/mL	0.0124	0.7717	0.9880
4 mg/mL	0.0115	0.7828	0.9929
alginate beads	0.3063	0.4876	0.9800

The adsorption isotherms of all the chitosan nanoparticles and calcium-alginate gel microbeads showed similar behavior over a wide range of concentration of the copper sulfate solution.

In both the low and high concentration ranges, calcium-alginate gel microbeads have a higher maximum adsorption capability value than that of chitosan nanoparticles. This difference in adsorption capacity can be explained by the distinct binding mechanisms with copper ions. The chelation mechanism is the presumed dominant mechanism accounting for the interaction between the copper ions and chitosan [21], while the bonds between copper ions and alginate are formed by electrostatic attraction and chemical bonding on the carboxylate groups according to Siew *et al.* [46]. In addition, calcium-alginate gel microbeads and chitosan nanoparticles may have different numbers of adsorption sites per unit mass, as estimated by the following calculation.

The maximum mass of copper ions adsorbed due to each binding mechanism can be estimated though the following equation:

$$adsorption(mg / g) = \frac{M_{Cu}}{M_{subunit} \times N} \times d \times 1000mg / g \quad (3-5)$$

where  $M_{subunit}$  (g/mol) is the molar weight of the polymer's subunit and  $N$  is the number of subunits needed to form an adsorption site. For instance,  $N=2$  in the "bridge model," and  $N=1$  in the "pendant model." Therefore, the denominator gives the molar weight of the binding sites.  $M_{Cu}$  (g/mol) is the molar weight of copper. The parameter  $d$  is the active fraction of the polymer. For chitosan,  $d$  is the degree of deacetylation, while, for alginate,  $d$  is the fraction of potential site-subunits in alginate. For example, in the traditional "egg-box" assumption,  $d$  is the fraction of guluronic acid (G) present, since only G blocks are involved in the formation of "egg-box" sites, while for the more recent hypotheses,  $d=1$  because both G and M residues contribute to the binding sites. Since large calcium-alginate gel beads are insufficiently cross-linked, their experimental maximum adsorption

capacity is not able to indicate the real binding mechanism. Therefore, only chitosan nanoparticles and alginate microbeads were discussed here.

Comparing the experimental data with approximate calculations based on binding models, as presented in Table 3-5, the “bridge model,” which involves two amine groups in every complex ( $N=2$ ), is a suitable description of the chitosan adsorption mechanism in this research. Also, the concept that a single subunit is involved in each copper ion binding site would be the best hypothesis for the calcium-alginate gel microbeads, in contrast to the four subunits required by the “egg-box” model. According to such calculations, calcium-alginate gel microbeads have more binding sites than chitosan gel nanoparticles per unit mass.

**Table 3-5.** Experimental adsorption capability and estimated adsorption capabilities ( $Q_{\max}$ ) calculated by binding models.

Binding model		Estimated data $Q_{\max}$ (mg/g)	Experimental data $Q_{\max}$ (mg/g)
Chitosan	Bridge model	180	78 - 112
	Pendant model	361	
Alginate	N=1	366	303
	N=2	183	
	N=4 (“egg-box”)	64	

The adsorption isotherm of alginate-chitosan combination particles exhibits similar behavior to that of chitosan nanoparticles and alginate microbeads in the low concentration region, as shown in Figure 3-14. It displays linear behavior and follows the Langmuir model very well as expected. Presented in Table 3-6, the combination particles have an intermediate value of the maximum adsorption capacity  $Q_{\max}$  and a value of the

affinity coefficient  $K_s$  similar to that of alginate beads, likely due to the fact that calcium-alginate gel microbeads are dominant in the combination particles.

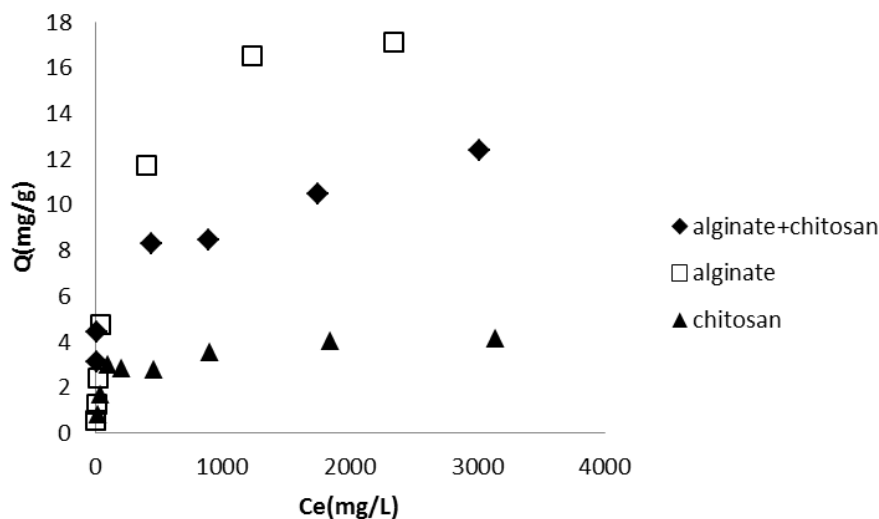


**Figure 3-14.** Adsorption isotherms of alginate-chitosan combination particles, calcium-alginate gel microbeads and chitosan nanoparticles (prepared with 2 mg/mL chitosan solution and 0.7 mL TPP) in the low  $\text{Cu}^{2+}$  concentration region (0.5-50 mM).

**Table 3-6.** Adsorption capacity and affinity of chitosan nanoparticles (prepared with 2 mg/mL chitosan solution and 0.7 mL TPP), calcium-alginate gel microbeads and alginate-chitosan combination particles in the low  $\text{Cu}^{2+}$  concentration region (0.5-50 mM).

	$Q_{\text{max}}$ (wet) (mg/g)	$K_s$ (L/mg)	$R^2$
Chitosan nanoparticles	4.24	0.0088	0.9966
Alginate microbeads	18.32	0.0063	0.9967
Combination Particles	12.63	0.0061	0.9779

Based on the alginate-chitosan weight ratio and single-particle data, the adsorption capabilities of combination particles are estimated and compared with experimental data from combination particles in Figure 3-15. The comparison shows that the experimental

data are consistent with estimated data in the low concentration region, which indicates that chitosan nanoparticles and alginate microbeads adsorb copper ions independently in the combination particles. The presence of chitosan nanoparticles attached to the surface of alginate microbeads does not appear to affect the copper ion adsorption by either type of particles. Therefore, a mass fraction weighted average provides a convenient method to predict the adsorption capacity of alginate-chitosan combination particles with a specific weight ratio.

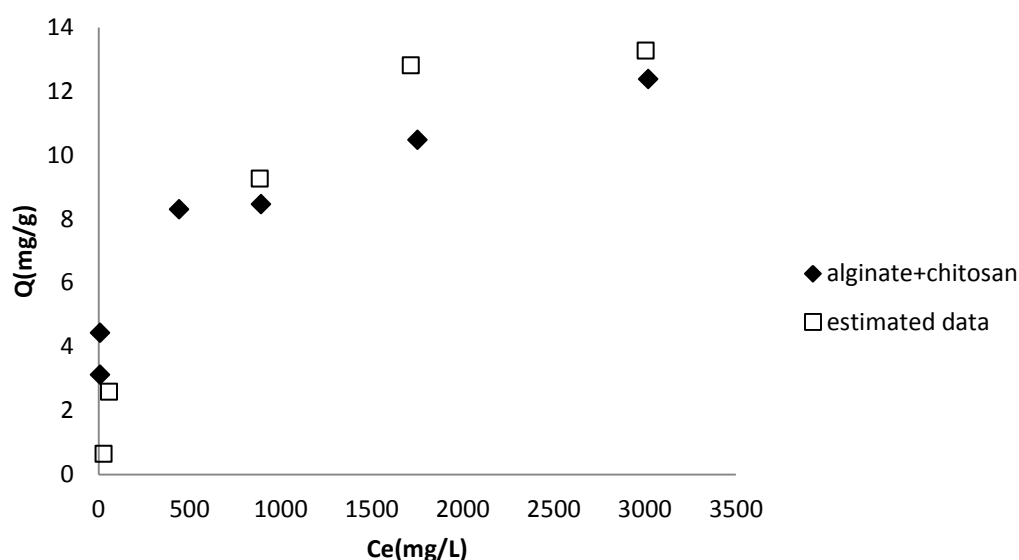


**Figure 3-15.** Estimated vs. measured adsorption capability of combination particles.

From the equilibrium adsorption capability study, both chitosan nanoparticles and calcium-alginate microbeads have demonstrated efficacy in the removal of heavy metal ions from aqueous solution. Our preliminary ongoing work shows that chitosan nanoparticles may have faster kinetics than calcium-alginate microbeads. Benefitting from the rapid kinetics of chitosan nanoparticles and the high adsorption capacity of

alginate, alginate-chitosan combination particles can be considered a promising biosorbent that will perform effectively and efficiently in multi-ion circumstances. The results of this study can potentially contribute to the development of cost-effective and environmentally benign water purification technologies.

### **3.4 Summary**

Chitosan gel nanoparticles were synthesized from three solution concentrations by ionic cross-linking with TPP and were characterized by zetasizing and TEM. The equilibrium adsorption capability of the chitosan nanoparticles, calcium-alginate gel microbeads and large calcium-alginate gel beads to adsorb copper ions from copper sulfate solution at fixed pH has been explored. Equilibrium adsorption properties of chitosan nanoparticles have similar trends to those of calcium-alginate gel microbeads and large calcium-alginate gel beads, and the adsorption capacity varies with the synthesis concentration of chitosan nanoparticles.

Adsorption for both chitosan nanoparticles and alginate microbeads occurs differently in a low concentration (0.5-50 mM) copper sulfate solution and a high concentration solution (50mM-1 M). The Langmuir isotherm fits the low concentration region well. In contrast, approximately linearly increasing adsorption was observed at high solution concentrations.

Key results comparing the adsorption properties of several types of chitosan nanoparticles for copper ions suggest that the phosphate groups in the cross-linker TPP can provide additional adsorption sites that have lower affinity than amine groups for copper ions. Exceptionally high affinity between copper ions and chitosan nanoparticles may result in the pore blockage phenomenon, where the interior of the particle becomes inaccessible, and consequently limits the adsorption capacity of particles. In addition, calcium-alginate microbeads have higher maximum adsorption capacity and affinity for  $\text{Cu}^{2+}$  in very dilute concentration than large calcium-alginate beads due to their higher crosslinking degree.

From a comparison between the experimental data and approximate calculations estimating the maximum adsorption capacity of the materials, the most probable adsorption mechanisms could be identified. The “bridge model” can be considered a reasonable description of the chitosan/metal ion binding pattern. Also, adsorption sites of alginate are most likely to be formed by only one mannuronate or guluronate block, in contrast to the four guluronate subunits required by the “egg-box” model. Comparing the two biopolymers, in both the low and high concentration ranges, calcium-alginate gel microbeads have a higher maximum adsorption capacity than that of chitosan nanoparticles, likely due to the higher estimated density of adsorption sites present in alginate compared to chitosan with the properties of the experimental system.

Alginate-chitosan combination particles were also observed, which have an intermediate value of the maximum adsorption capacity  $Q_{max}$ , and identical value of the affinity

coefficient  $K_s$  to that of alginate microbeads in part because of structural similarity to alginate beads. The adsorption capabilities of combination particles can be predicted by the weight ratio of calcium-alginate gel microbeads and chitosan gel nanoparticles. Benefitting from the rapid kinetics of chitosan nanoparticles and the high adsorption capacity of alginate, alginate-chitosan combination particles are likely to perform effectively and efficiently in multi-ion systems as a novel, environmentally friendly biosorbent.



## **Chapter 4 Kinetics Study of Copper Ion Adsorption by Calcium-Alginate Gel Microbeads, Large Calcium-Alginate Gel Beads and Chitosan/Alginate Combination Particles**

### **4.1 Introduction**

In the design of a water purification system, the study of the adsorption kinetics of the adsorbent is essential since it affects the efficiency and in-service life of the system directly. In addition, knowledge of the adsorption kinetics of adsorbent can provide a better understanding of the adsorption mechanism and insight into the potential rate controlling steps, such as mass transport and chemical reaction processes. To achieve those goals, kinetics models have been used to analyze experimental data. It is worthy to notice that the complete kinetics model needs to consider not only the diffusion equations, but also boundary conditions, including the adsorption isotherm equation that controls the equilibrium at the solid–liquid interface and the reaction kinetic equations[21]. Therefore, the system of equations is too complex to solve and simple kinetic models such as first- or second-order rate equations are not applicable. To simplify the solution method, only the rate controlling step is considered to contribute to the kinetic rate. In a well-mixed batch system, the influence of mass transfer resistance is negligible. Chemical reaction is mostly likely to be the potential rate controlling step. This hypothesis can be confirmed by fitting pseudo-first-order equation and pseudo-second-order equation to experimental data.

In the previous study, it was found that the adsorption process of copper ions on to chitosan gel nanoparticles was too rapid to be captured by our limited experimental methods, resulting from their nanoscale size and high affinity to copper ions. Therefore, in this chapter, only the adsorption kinetics of copper ions on to calcium-alginate gel microbeads, chitosan/alginate combination particles and large calcium-alginate gel beads from the last chapter are discussed. Besides, since the adsorption rate increases with the increase of initial concentration of the adsorbate, several concentration of copper sulfate solution was tested in preliminary experiments. The result showed that 1 mM copper sulfate solution was the most suitable concentration for the investigation of adsorption kinetics of particles, because it provided more accurate data that could describe the entire adsorption process, compared to other higher initial concentrations of solutions. The amount of copper ions adsorbed on to calcium-alginate gel microbeads, chitosan/alginate combination particles and large calcium-alginate gel beads over various time periods was measured by ICP/MS. Experimental data were fitted to pseudo-first order and pseudo-second order kinetic models, by which pseudo rate constants were estimated and potential rate-controlling steps were clarified.

## **4.2 Experimental Methods**

### **4.2.1 Particle synthesis**

Calcium-alginate gel microbeads, chitosan/alginate combination particles and large calcium-alginate gel beads were synthesized by using the method presented in the previous chapter (section 3.2.2).

#### 4.2.2 Adsorption experiment

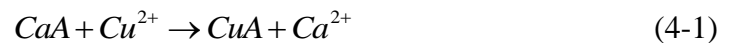
Calcium-alginate gel microbeads, chitosan/alginate combination particles and large calcium-alginate gel beads were put into 15 mL test tubes, yielding 12 tubes with calcium-alginate gel microbeads, 12 tubes with chitosan/alginate combination particles, and 12 tubes with large calcium-alginate gel beads. Each tube contained around 0.2 g (wet mass) of particles. For calcium-alginate gel microbeads and chitosan/alginate combination particles, 3 mL of 1 mM copper sulfate solution was added into each tube, and then the samples were sonicated to uniformity in the same tube and left under magnetic stirring for 10, 20, 30, 40, 50, 70, 90, 120, 240, 360, 480 and 1440 minutes, respectively. Afterward, the samples were centrifuged at 48,400 g for 10 minutes. After removing the supernatant fluid, pellets were collected and weighted and then transferred to big centrifuge tubes. 1 mL of DI water was added into each centrifuge tube and the samples were sonicated again until all the particles were suspended uniformly in the centrifuge tubes. For large calcium-alginate gel beads, there was no need to centrifuge samples. After adding 3 mL of 1 mM copper sulfate solution into each tube, the samples were stirred on a magnetic stirring plate for 10, 20, 30, 40, 50, 70, 90, 120, 240, 360, 480 and 1440 minutes, respectively. Then the solution was poured out. The large beads were transferred to a big centrifuge tubes and their mass was recorded. The amounts of copper ions adsorbed to the calcium-alginate gel microbeads, chitosan/alginate combination particles and large calcium-alginate gel beads were measured by inductively coupled plasma mass spectrometry (ICP/MS) at each time point.

The procedure of ICP/MS was presented in the previous Chapter (section 3.2.4).

### 4.3 Results and Discussion

It is often incorrect to apply simple kinetic models such as first- or second-order rate equations to an adsorption system with solid surfaces that are rarely homogeneous, because the effects of transport phenomena and chemical reactions are often experimentally inseparable. Therefore, several adsorption kinetic models such as pseudo-first and pseudo-second order kinetic models have been used to test experimental data, in order to investigate the mechanism of adsorption and to understand the adsorption kinetics and the rate limiting step during an adsorption process.

The chemical reaction of alginate and copper ions may be described by the following equation[52]:



If the reaction has a first-order mechanism,

$$\frac{d[CaA]_t}{dt} = -k_1[CaA]_t \quad (4-2)$$

where  $[CaA]_t$  is the number of unreacted adsorption sites on calcium alginate at time  $t$ , that can be substituted by the total number of sites  $[CaA]_0$  minus the number of occupied sites on calcium alginate  $[CaA]_r$  at time  $t$ , then

$$\frac{d[CaA]_r}{dt} = k_1([CaA]_0 - [CaA]_r) \quad (4-3)$$

Since the number of reacted adsorption sites on calcium alginate is proportional to the amount of copper loaded on alginate, assuming all sites are occupied at equilibrium, the equation becomes the pseudo-first order chemisorption kinetic rate equation of Lagergren[53], expressed as:

$$\frac{dq_t}{dt} = k_1(q_e - q_t) \quad (4-4)$$

where  $q_e$  (mg/g) is the amount of copper ions adsorbed on to a unit mass of particles at equilibrium. It is important to notice that the value of  $q_e$  depends on the initial concentration of solution, in contrast to the constant maximum equilibrium adsorption capacity  $Q_{max}$ .  $q_t$  (mg/g) is the amount of copper ions adsorbed on to a unit mass of particles at time  $t$ , and  $k_1$  is the rate constant of the pseudo-first order kinetic model ( $\text{min}^{-1}$ ).

After integrating from  $t = 0$  to  $t = t$  and  $q_t = 0$  to  $q_t = q_t$  and applying boundary conditions, the equation becomes:

$$q_t = q_e(1 - e^{-k_1 t}) \quad (4-5)$$

This equation can be transformed to a linear form:

$$\ln(q_e - q_t) = \ln(q_e) - k_1 t \quad (4-6)$$

where  $q_e$  can be obtained from experimental data. The straight-line plots of  $\ln(q_e - q_t)$  against  $t$  were used to determine the rate constant  $k_1$ .

The equation applicable to experimental results generally differs from a true first-order equation in two ways[54]:

- a. The parameter  $q_e - q_t$  does not represent the number of available sites, since  $q_e$  depends on the solution concentration. In other words, the assumption of full occupation of adsorption sites at equilibrium is illegitimate.
- b. The parameter  $\ln(q_e)$  is an adjustable parameter which is often not found equal to the intercept of a plot of  $\ln(q_e - q_t)$  against  $t$ , whereas in a true first-order adsorption reaction  $\ln(q_e)$  should be equal to the intercept of a plot of  $\ln(q_e - q_t)$  against  $t$ .

The pseudo-first-order kinetic model has been used extensively to describe the adsorption of metal ions onto adsorbents.

Similar to the pseudo-first order equation, the pseudo-second order chemisorption kinetic rate equation is expressed as:

$$\frac{dq_t}{dt} = k_2(q_e - q_t)^2 \quad (4-7)$$

where  $q_e$  (mg/g) is the amount of copper ions adsorbed on to a unit mass of particles at equilibrium, and  $q_t$  (mg/g) is the amount of copper ions adsorbed on to a unit mass of particles at time  $t$ , and  $k_2$  is the rate constant of the pseudo-second order kinetic model (g/mg min).

After integrating from  $t = 0$  to  $t = t$  and  $q_t = 0$  to  $q_t = q_t$  and applying boundary conditions, the integrated form is:

$$\frac{1}{q_e - q_t} = \frac{1}{q_e} + k_2 t \quad (4-8)$$

which can be rearranged to obtain a linear form:

$$\frac{t}{q_t} = \frac{1}{k_2 q_e^2} + \frac{1}{q_e} t \quad (4-9)$$

If pseudo-second order kinetics is applicable, the plot of  $t/q_t$  against  $t$  will present a linear relationship, and equilibrium capacity  $q_e$  and rate constant  $k_2$  can be determined by the slope and intercept. The pseudo-second order kinetic model has been the most widely used model for the adsorption of metal ions from wastewater[55], and is in agreement with a chemisorption mechanism being the rate controlling step.

Figure 4-1 shows the increase in the amount of copper ions adsorbed onto alginate microbeads, combination particles and large calcium-alginate gel beads over time. The adsorption occurred rapidly within the first 50 to 70 minutes for both alginate microbeads and combination particles, and then slowed down and gradually reached a plateau after three hours, indicating the approach to the equilibrium state. For large calcium-alginate gel beads, the rapid adsorption process happened within the first 40 minutes, and afterward it slowed down significantly and approached equilibrium after 70 minutes.

To test the applicability of the pseudo-first order model in the adsorption process, the values of  $\ln(q_e - q_t)$  against adsorption time  $t$  were plotted in Figure 4-2, and  $k_1$ ,  $q_e$  (exp.) and  $q_e$  (cal.) obtained based on the pseudo-first order equation were presented in Table 4-1. It can be seen that the plot is roughly linear for alginate microbeads and combination particles, but the theoretical  $q_e$  values, calculated from the intercept, do not agree with

experimental  $q_e$  values. The plot of  $\ln (q_e - q_t)$  versus time didn't show any linear relationship for large calcium-alginate gel beads. The correlation coefficient is much lower than 0.9, showing poor fit to experimental data. Therefore, the pseudo-first order kinetic model could not represent the adsorption process of copper ions on to alginate microbeads, combination particles and large calcium-alginate beads accurately.

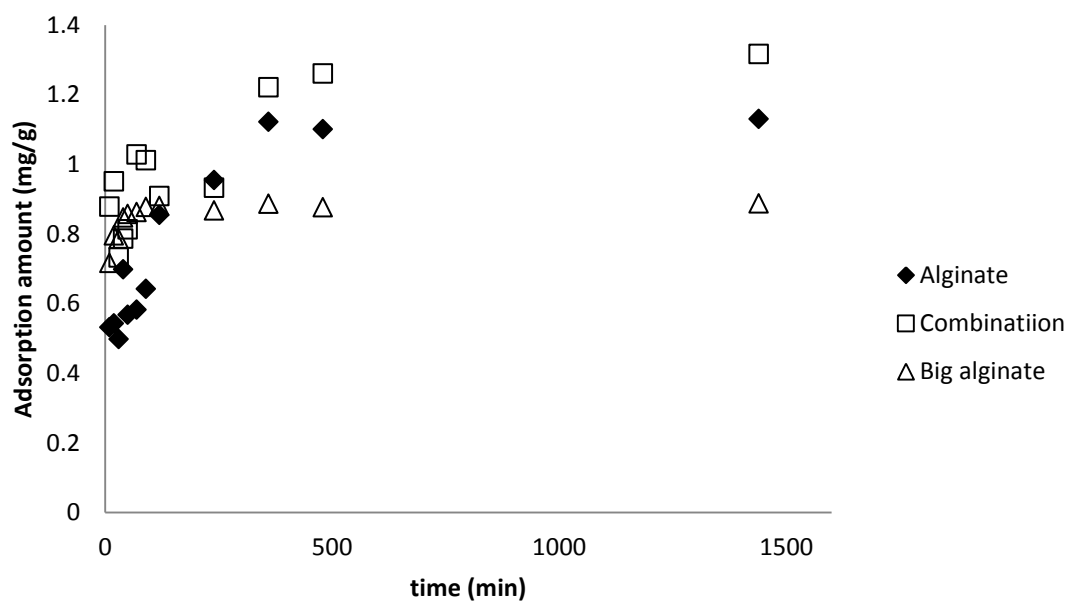


**Figure 4-1.**  $\text{Cu}^{2+}$  adsorbed onto calcium-alginate microbeads, combination particles and large calcium-alginate gel beads over time.



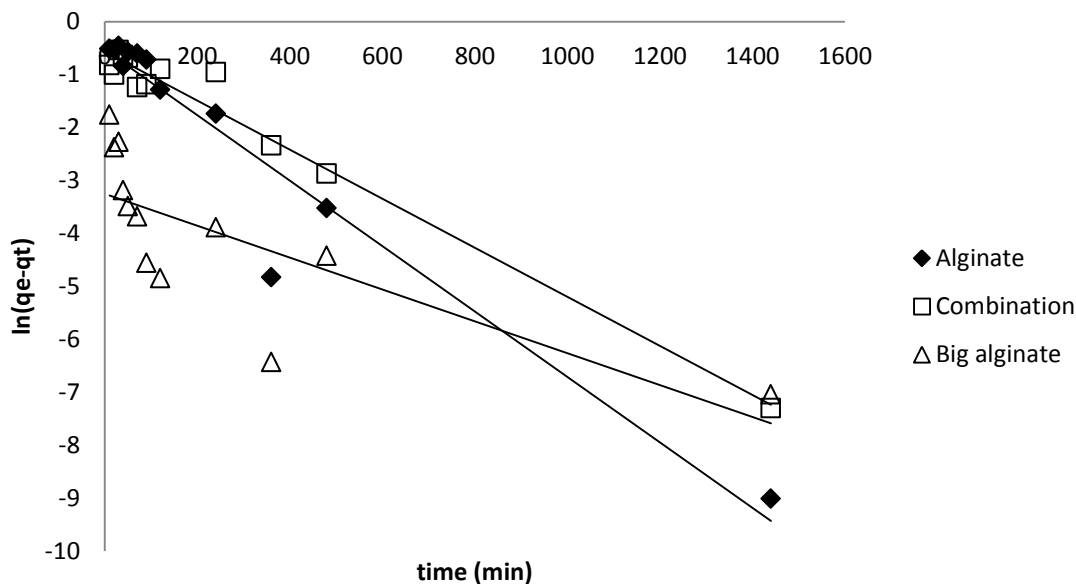


**Figure 4-2.** Linear pseudo-first order equation fit to adsorption data of calcium- alginate microbeads, combination particles and large calcium-alginate gel beads over time.

Figure 4-3 exhibits the plot of  $t/q_t$  against  $t$ , and the values of  $k_2$ ,  $q_{e(\text{exp.})}$  and  $q_{e(\text{cal.})}$  obtained from the pseudo-second order equation were presented in Table 4-1. Contrary to the pseudo-first order equation, the theoretical  $q_e$  values for all types of particles, calculated from the slope, are very close to their experimental  $q_e$  values. In addition, correlation coefficients are higher than 0.99, indicating that pseudo-second order kinetic model successfully predicts the adsorption behavior over the whole range of studies. It is confirmed that chemisorption mechanism is the rate controlling step in the adsorption process of copper ions onto alginate microbeads, combination particles and large calcium-alginate gel beads from copper sulfate solution in a batch system, and the chemisorption reaction is second order.

Comparing the pseudo-second order rate constant  $k_2$  of alginate microbeads to that of chitosan/alginate combination particles shows that the adsorption of copper ions on to

combination particles was slightly faster than on to plain alginate microbeads. These results suggest that the chitosan nanoparticles have faster adsorption kinetics than the alginate microbeads due to their nanoscale size and high affinity to copper ions. In preliminary experiments, we did not have fine enough time resolution to capture the kinetics of adsorption on to chitosan nanoparticles alone. However, the amount of alginate is dominant in chitosan/alginate combination particles in order to avoid aggregation during synthesis. Hence, the adsorption acceleration causing by the existence of chitosan nanoparticles is not very obvious for combination particles.

The adsorption of copper ions on to large calcium-alginate gel beads was much faster than on to alginate microbeads and combination particles, even though they have much larger size and smaller surface/volume ratio. This fact could be interpreted by considering the following two points. First, in a well-mixed batch system, the intra-particle diffusion resistance is negligible for alginate microbeads, confirmed by the excellent fitting to the pseudo-second order equation which has the assumption of chemical reaction being the rate limiting step. Also, most of the adsorption sites of large calcium-alginate gel beads are located on the outer layer, making copper ions easy to bind with. Hence, the relatively small surface/volume ratio will not significantly slow the adsorption process of copper ions on to large calcium-alginate gel beads. Second, for alginate microbeads and combination particles, even though they may have more adsorption sites exposed to copper ions in solution, the pore-blockage effect may occur due to their high affinity to copper ions, as discussed in Chapter 3. The copper ions adsorbed on the particles' surface in the beginning may repel surrounding copper ions and slow down further adsorption

considerably. The pore blockage effect could be considered as an additional mass transfer resistance to copper ions, which explains the fact that the adsorption data fitting to the pseudo-second order equation of alginate microbeads and combination particles was not as perfect as that of large calcium-alginate gel beads. Therefore, the adsorption of copper ions on to alginate microbeads and combination particles was gradual, while the amount of copper loaded on to large calcium-alginate beads increased rapidly and sharply before reaching equilibrium.

Meanwhile, large calcium-alginate gel beads had smaller equilibrium adsorption capacity than alginate microbeads and combination particles. As discussed in Chapter 3, the main reason causing relatively low adsorption capacity of large calcium-alginate gel beads was their low degree of cross-linking, compared to alginate microbeads. There are fewer adsorption sites on large calcium-alginate gel beads than on alginate microbeads, leading to smaller adsorption capacity at equilibrium.

Compared with literature values[60, 62, 63] listed in Table 4-2, it was found that calcium-alginate microbeads and combination particles have comparable adsorption kinetics with other types of low-cost adsorbents, and large calcium-alginate beads have much faster adsorption kinetics than most of other adsorbents except chitosan microbeads. Considering the fact that even though the value of the rate constant  $k_2$  of chitosan microbeads is slightly bigger than that of large calcium-alginate beads, alginate has greater maximum adsorption capacity than chitosan, proved in Chapter 3. Therefore,

the large calcium-alginate beads have great potential to be used as a biosorbent in water purification.

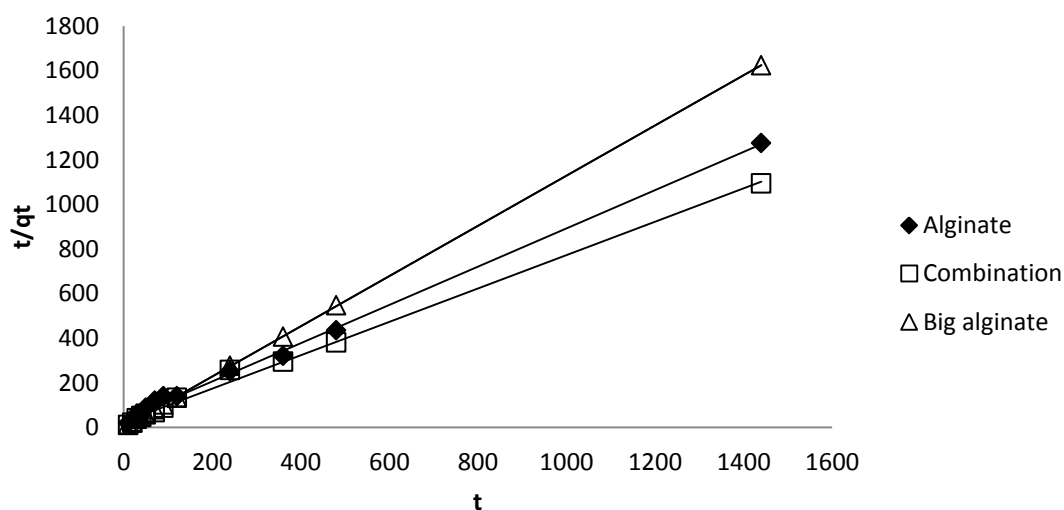


**Figure 4-3.** Linear pseudo-second order equation fitted to adsorption data of calcium-alginate microbeads, combination particles and large calcium-alginate gel beads over time.

**Table 4-1.** Parameters of adsorption kinetics models.

Kinetic models	Calcium-alginate microbeads	Combination particles	Large calcium- alginate beads
$q_{e(\text{exp.})}$ (mg/g)	1.13	1.32	0.888
<b>Pseudo-first order equation</b>			
$q_{e(\text{cal.})}$ (mg/g)	0.587	0.567	0.039
$k_1$ (min <sup>-1</sup> )	0.0062	0.0046	0.003
$r^2$	0.932	0.975	0.580
<b>Pseudo-second order equation</b>			
$q_{e(\text{cal.})}$ (mg/g)	1.165	1.336	0.888
$k_2$ (g/mg min)	0.0214	0.0227	0.4356
$r^2$	0.996	0.996	1

**Table 4-2.** Literature values of pseudo-second order adsorption kinetics of copper ions on to various adsorbents compared with the results of this study. (The values of  $k_2$  of this study were recalculated based on dry mass)

Source	Adsorbents	$k_2 \times 10^3$ (g/mg min)	pH
Karagunduz <i>et al.</i> , 2006[63]	Large calcium-alginate beads	1.23	4.0
	Shell of lentil	4.33	5.0
Aydın <i>et al.</i> , 2008[64]	wheat	18.4	6.0
	rice	3.19	6.0
Nghah <i>et al.</i> , 2010[62]	Chitosan/TPP microbeads	46.6	4.5
	Calcium-alginate microbeads	1.29	
This study	Combination particles	1.37	3.5
	Large calcium-alginate beads	32.7	

#### 4.4 Summary

In this chapter, the adsorption kinetics of copper ions on to calcium-alginate gel microbeads, chitosan/alginate combination particles and large calcium-alginate gel beads were studied. The results show that the pseudo-first order kinetic model could not represent the adsorption process accurately, while the pseudo-second order kinetic model successfully predicted the adsorption behavior over the whole range of studies. It is confirmed that chemisorption mechanism is the rate controlling step in the adsorption process of copper ions on to alginate microbeads, combination particles and large calcium-alginate gel beads from copper sulfate solution in a batch system, and the chemisorption reaction is second order.

Moreover, the adsorption of copper ions on to alginate microbeads and combination particles was gradual, while the amount of copper loaded on to large calcium-alginate beads increased quickly and sharply before reaching equilibrium. In other words, the adsorption kinetics of large calcium-alginate gel beads was much faster than that of alginate microbeads and combination particles. The adsorption of copper ions on to combination particles was slightly faster than on to plain alginate microbeads, benefitting from the presence of chitosan on the combination particles. Last but not least, large calcium-alginate gel beads had smaller equilibrium adsorption capacity than alginate microbeads and combination particles due to their low degree of cross-linking compared to alginate microbeads.

## **Chapter 5 Copper Ion Removal by Fixed-Bed Columns**

### **5.1 Introduction**

Although much research has been done and many data have been obtained from different equilibrium adsorption systems, these data are difficult to apply to fixed-bed columns, which are extensively used in industry. The major problem in equilibrium studies is that they involve batch contact systems, whose isotherms cannot give accurate scale-up data in fixed-bed systems since a flow column is not at equilibrium; uneven flow patterns may occur in fixed-bed column systems. A model is needed in designing columns to study recycling and regeneration of adsorbents, and to predict how long they will last before regeneration or replacement becomes necessary.

In this work, large calcium-alginate gel beads were chosen as the adsorbent packed into a fixed-bed column, since they have high adsorption capacity and fast adsorption kinetics compared to chitosan nanoparticles, alginate microbeads and chitosan/alginate combination particles. In addition, large calcium-alginate gel beads are easy to operate during packing, and unlikely to cause clogging or leaking of the fixed-bed columns. In order to study adsorption behavior of a fixed-bed column system, the Thomas model, Adam-Bohart model and Yoon-Nelson model were used to fit the experimental data.

## **5.2 Experimental Methods**

### **5.2.1 Preparation of large calcium-alginate gel beads**

Large calcium-alginate gel beads were synthesized by using the method presented in Chapter 3 (section 3.2.2).

### **5.2.2 Fixed-bed column experimental procedures**

In this experiment, plastic tube connectors with equal size ends were used as the fixed-bed columns. Since the wall of the tube connector is translucent, the color change of packed particles could be observed as copper was adsorbed.. After packing alginate gel beads into it, nylon meshes (Spectrum Laboratories, Inc. CA) were adhered by silicon glue on to both ends in order to trap particles inside. The pore size of the meshes is 300  $\mu\text{m}$  with 50% open area. And the thickness of the meshes is 200  $\mu\text{m}$ . After 24 hours, the silicon glue was fully dried. To minimize possible wall and axial dispersion effects in the fixed-bed column, the bed length-to-particle diameter ratio must be greater than 20[60]. Two sizes of the column were used in the experiment. The large column had an internal diameter of 1/2 inch (1.27 cm) and column height of 6.4 cm, and the small column had an internal diameter of 1/4 inch (0.635 cm) and column height of 4.8 cm. The diameter of the beads was around 1 mm. Therefore, the bed length-to-particle diameter ratio for both the large column and the small column was greater than 20.



A solution containing 1mM  $\text{CuSO}_4$  was pumped into the fixed-bed column by a syringe pump (New Era Pump Systems, Farmingdale, NY) with volumetric flow rate varied at 0.1 mL/min, 0.25 mL/min and 1mL/min. The setup is shown in Figure 2. To be consistent with equilibrium experiments, the pH of the  $\text{CuSO}_4$  solution was fixed at 3.5. Adsorption experiments were carried out at room temperature. The outflow was sampled at 5 minutes, 10 minutes, 20 minutes, 30 minutes, 40 minutes, 60 minutes, 80 minutes, 120 minutes, 150 minutes, 180 minutes, 210 minutes, 240 minutes, 300 minutes, 360 minutes and 480 minutes. The copper ion concentration in collected liquid samples was tested by inductively coupled plasma mass spectrometry (ICP/MS), the method which was introduced in Chapter 3, 3.2.4.

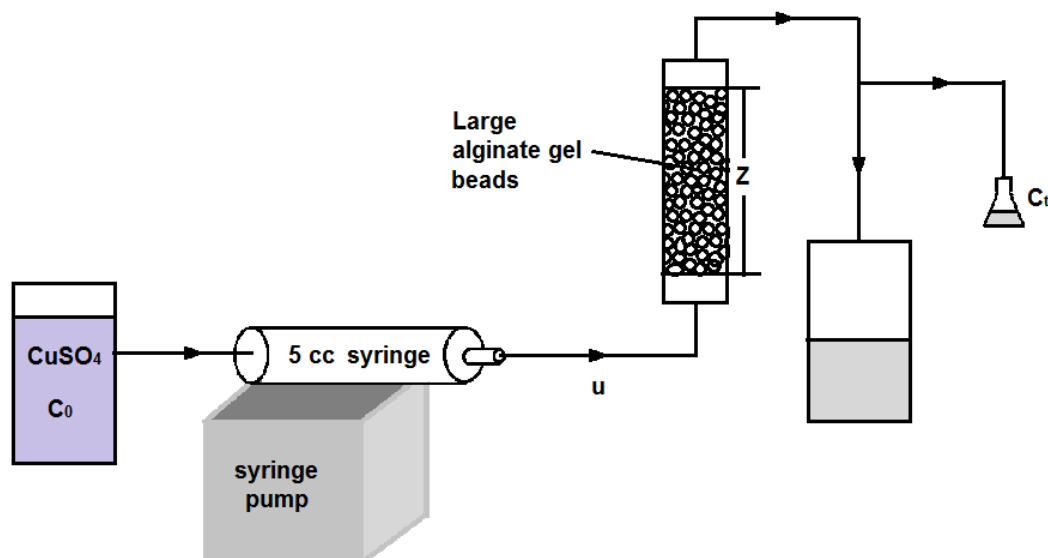


**Figure 2-2.** Schematic view of the fixed-bed column experiment.

## 5.3 Results and Discussion

### 5.3.1 Fixed-bed column adsorption results

To investigate the effect of flow rate on the adsorption behavior of fixed-bed columns, the solution containing 1mM CuSO<sub>4</sub> was induced into the fixed-bed columns with volumetric flow rate varied at 0.1 mL/min, 0.25 mL/min and 1mL/min. For the large column, it was observed that when the flow rate was high, the inlet end of column appeared to be light blue at first, and then the color of the inlet part darkened while the entire body of column gradually turned blue. When the experiment was completed, the fixed-bed column exhibited even blue color. In the case of low flow rate, however, only the inlet part of column had significant color change during operation. As the copper sulfate solution was pumped in, the inlet end became faint blue at the beginning, and then the color darkened. After 480 minutes, the flow entrance region showed bright blue color, while the rest of the column remained colorless.

In fact, the color change of columns provided visual evidence of the adsorption process inside the fixed-bed columns. When the flow rate was high, the copper/alginate contact time was short on each layer of adsorbent. Even though the copper ions adsorbed on to alginate beads near the inlet end first, there was still a large amount of copper ions carried farther down the column by flow before the adsorption reaction occurred. Therefore, the adsorption was performed relatively uniformly in the fixed-bed column. In addition, since the volume of treated solution was large under high flow rate, the fixed-

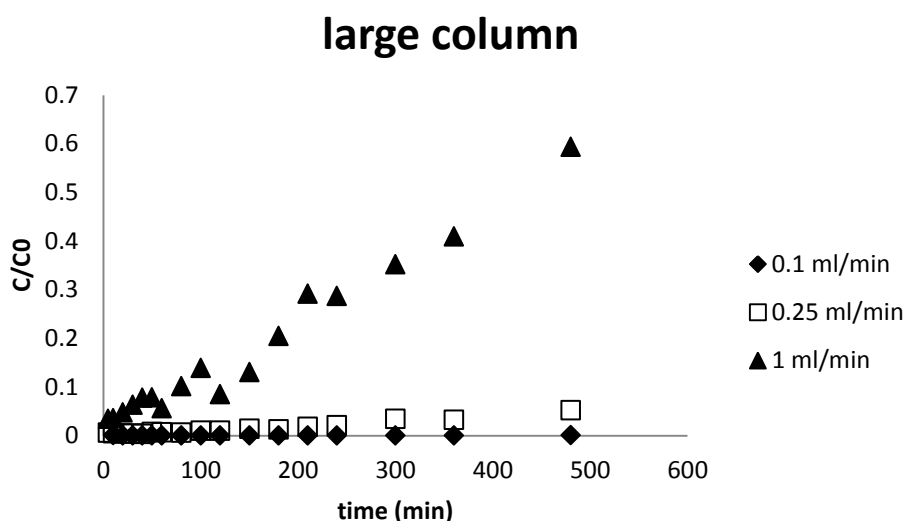
bed column might reach saturation at the end of the experiment. For the low flow rate case, there was a longer copper/alginate contact time for adsorption on each layer of adsorbent. As the solution passed through the fixed-bed column, the concentration of copper ions decreased significantly with axial position due to adsorption occurring along the way. Therefore, the adsorption rate became much lower at the outlet end of the column compared to that of the inlet end. Since the amount of solution passing through was not sufficient to saturate the entire fixed-bed column, adsorption mainly occurred near the inlet part of the column.

The difference in color change caused by flow rate in small columns was not as obvious as that in large columns. Resulting from the limited amount of adsorbent in small columns, all of the small columns turned bright blue when the experiment finished, indicating that they were close to saturation.

In order to study the breakthrough properties of fixed-bed columns, the values of concentration of the outflow  $C$  at different times were divided by the value of the initial concentration of copper sulfate solution  $C_0$ , and plotted against operating time  $t$  when the flow rate was held constant at 0.1 mL/min, 0.25 mL/min or 1 mL/min, as presented in Figure 5-1 and Figure 5-2. In this study, the allowable breakthrough concentration was considered to be 5% of the initial concentration  $C_0$ .

Figure 5-1 shows the breakthrough curves of the large fixed-bed columns. It can be seen that the values of  $C/C_0$  increased gradually with operating time for all three columns

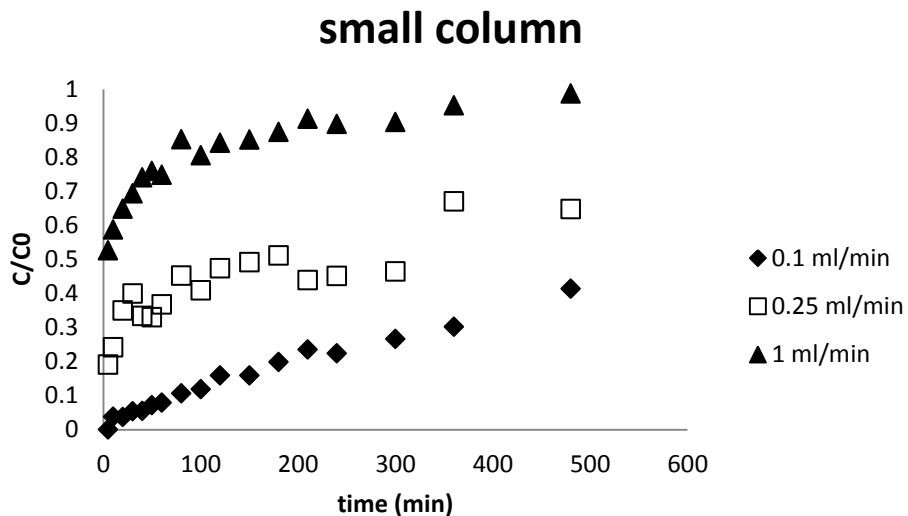
presented in Figure 5-1. The column adsorbing copper sulfate solution with 1 mL/min volumetric flow rate has the sharpest breakthrough curve among the three large columns and reached the breakthrough point after 25 minutes. The values of  $C/C_0$  for the other two columns increased very slowly. After 480 minutes, the column with 0.25 mL/min flow rate hit the breakthrough point, while the column with 0.1 mL/min flow rate was still below breakthrough when the adsorption experiments ended. None of the breakthrough curves exhibited a plateau during operation, indicating that the columns were not saturated after 480 minutes. Apparently, the column with 1 mL/min would have been saturated much sooner than the other two columns, if the operation had continued.



**Figure 5-1.** Breakthrough curves of the large fixed-bed column when the flow rate was 0.1 mL/min, 0.25 mL/min and 1 mL/min.

Figure 5-2 presents the breakthrough curves of the small fixed-bed columns. in contrast to the large columns, whose breakthrough curves showed a linear increase, the breakthrough curves of two small columns, which had high flow rate, exhibited a linear

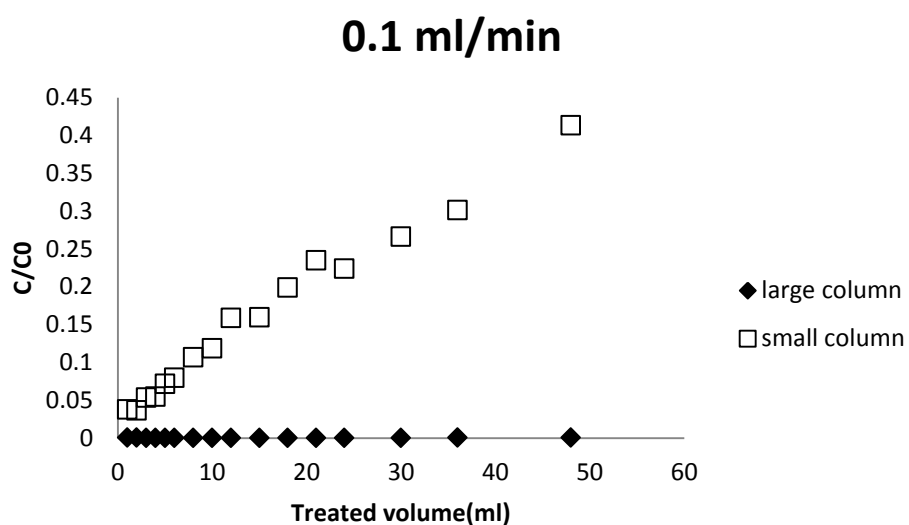
increase followed by a plateau shape. After 5 minutes of operation, the concentration of outflow from the column with 0.25 mL/min flow rate was already 20% of the inlet concentration, higher than the breakthrough concentration. For the highest flow rate column, the outflow concentration was more than 50% of the initial concentration at the very beginning of the experiment. These observations illustrated that 0.25 mL/min and higher volumetric flow rates were not suitable for small fixed-bed column operation. Since higher flow rate causes shorter residence time, when the feeding flow rate is higher than a critical value for certain fixed-bed columns, the alginate gel beads do not have sufficient time to bind with copper ions, resulting in inferior performance of the column. Comparing the breakthrough curves of the column with 0.25 mL/min and the one with 1 mL/min, it is clear that the adsorption slowed down after 180 minutes for 0.25 mL/min column, while for the 1 mL/min column, not much adsorption occurred after 80 minutes. This difference indicates a shorter column active life at a higher flow rate. The column is saturated faster at a higher flow rate because of the larger amount of copper ions fed into the column while the operation time is fixed. The breakthrough curve of the small column with 0.1 mL/min flow rate has a linearly increasing trend similar to that of the large columns. It reached breakthrough after 30 minutes of being fed with copper sulfate solution, and the adsorption kept going at a constant rate over the duration of the experiment.



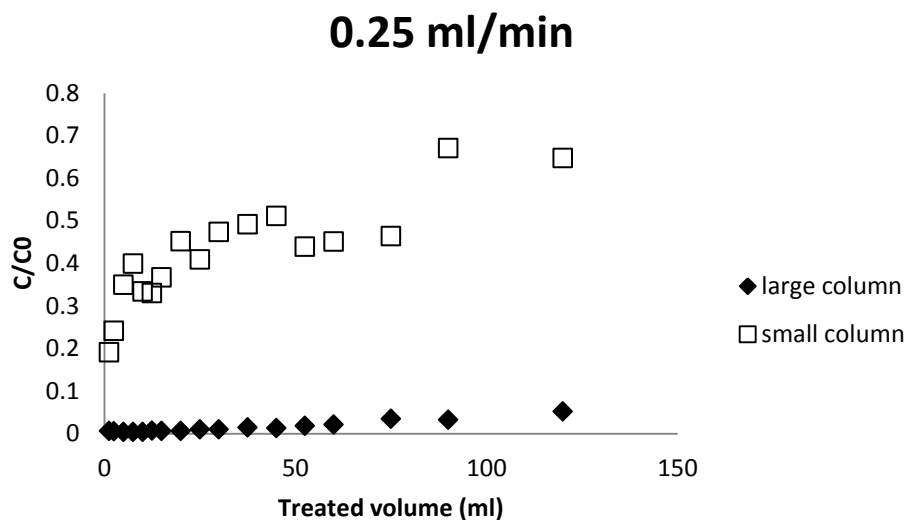
**Figure 5-2.** Breakthrough curves of the small fixed-bed column when the flow rate was 0.1 mL/min, 0.25 mL/min and 1 mL/min.

Figure 5-3, Figure 5-4 and Figure 5-5 plot the curves of  $C/C_0$  against the volume of treated solution at multiple flow rates. Figure 5-3 presents the breakthrough curves of the large column and small column at the flow rate of 0.1 mL/min. It can be seen that the small column reached breakthrough after treating 3 mL of copper sulfate solution, while the volume of treated solution before breakthrough was much greater for the large column. When the experiment was finished, the adsorption capacity of the large column was still sufficient. Figure 5-4 illustrates the breakthrough curves of the large column and small column at 0.25 mL/min flow rate. The large column successfully processed 120 mL of solution before breakthrough under this flow rate. However, 0.25 mL/min was too high for small column operation since the copper ion concentration was higher than the breakthrough concentration at the beginning of the experiment. Figure 5-5 has the breakthrough curves of large column and small column at the highest flow rate, 1 mL/min. When the flow rate was increased to 1 mL/min, the concentration of the outflow

from the large column grew to breakthrough much faster than at low flow rate. The large fixed-bed column treated 25 mL of solution in total before breakthrough. Similar with Figure 5-4, the small column presented in Figure 5-5 did not perform as well as expected. In addition, Figure 5-3, Figure 5-4 and Figure 5-5 consistently show that the breakthrough time was much longer for the large column than for the small column at the same flow rate. The difference can be explained by the fact that a larger fixed-bed column has more adsorbent available for copper ion binding, and therefore, more solution could be treated and the breakthrough time is longer.



**Figure 5-3.** Breakthrough curves of the large column and small column at the flow rate of 0.1 mL/min.



**Figure 5-4.** Breakthrough curves of the large column and small column at the flow rate of 0.25 mL/min.

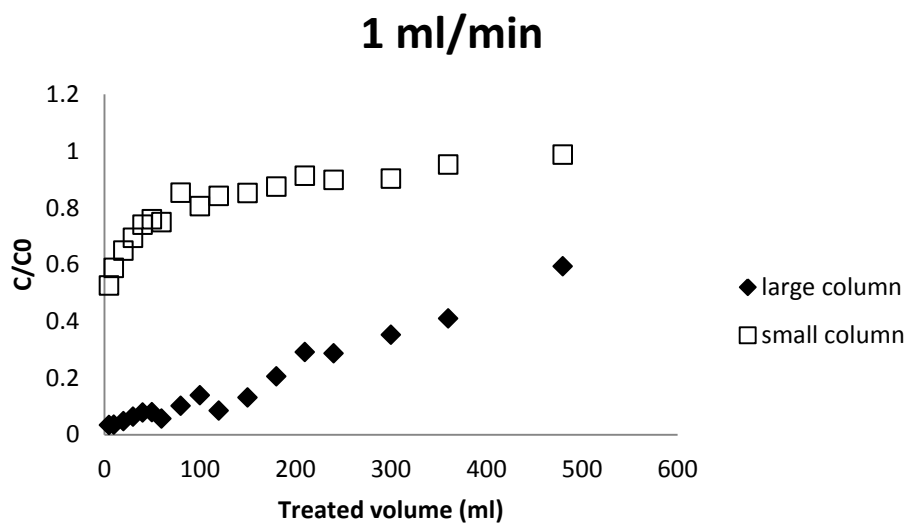


**Figure 5-5.** Breakthrough curves of the large column and small column at the flow rate of 1 mL/min.

To compare the efficiency of fixed-bed columns, the number of bed volumes (BV) was introduced and defined as:

$$BV = \text{Volume of solution treated} / \text{Volume of adsorbent} \quad (5-1)$$



In addition, void ratio and residence time were calculated by following equations:

$$\text{Void ratio} = (\text{Column volume} - \text{Particle volume}) / \text{Column volume} \quad (5-2)$$

$$\text{Residence time} = \text{Column volume} * \text{Void ratio} / \text{flow rate} \quad (5-3)$$

Table 5-1 summarized the number of bed volumes of all tested fixed-bed columns at breakthrough, and breakthrough time for each column. It shows that the large column with 0.25 mL/min flow rate has the highest BV number, which was able to treat 33.3 times as much as its own bed volume of copper sulfate solution before breakthrough. When the flow rate was increased to 1 mL/min, the BV number decreased to 7.4 for the large column, indicating lower efficiency than 0.25 mL/min fixed-bed column. Although the experiment did not give out the exact BV number of the 0.1 mL/min large column, it could be predicted that the 0.1 mL/min large column has much higher BV number than other two large columns, since the copper ion concentration of outflow was only 0.04% of initial concentration, far below the breakthrough concentration, after treating 14 times as much volume as its own bed has. The BV number decreasing with flow rate could be interpreted by the fact that the copper ions are more efficiently and fully adsorbed on to alginate beds when the copper/alginate contacting time is longer for each layer of adsorbent.

However, the BV number is not the only factor used to evaluate the fixed-bed column performance. Although the column operated at extremely low flow rate has a very high BV number, the breakthrough time will be very long, indicating low efficiency for treating the solution. Therefore, both BV number and breakthrough time should be taken into consideration in a practical application. A column with high BV number at

breakthrough and moderate breakthrough time is believed to be well-performing. In this study, the best tested fixed-bed column is the large column at 0.25 mL/min flow rate.

Comparing the BV number and breakthrough time of the small column at 0.1 mL/min, it was found that its performance resembled that of the large column which had 10 times as fast flow rate as the small column had. Considering that the small column contained roughly one tenth as many alginate particles as the large column contained, it is reasonable to deduce that the appropriate flow rate for certain fixed-bed column is proportional to the amount of adsorbent it contains.

**Table 5-1.** Operation parameters of large columns and small columns at flow rates of 0.1 mL/min, 0.25 mL/min and 1 mL/min.

	Large column			Small column		
<b>Flow rate (mL/min)</b>	0.1	0.25	1	0.1	0.25	1
<b>Particles volume (mL)</b>	3.4	3.6	3.4	0.43	0.41	0.41
<b>Void ratio</b>	0.58	0.56	0.58	0.71	0.73	0.73
<b>Residence time (min)</b>	47	18	4.7	11	4.4	1.1
<b>BV at breakthrough</b>	>> 14	33.3	7.4	6.9	N/A	N/A
<b>Breakthrough time (min)</b>	>> 480	480	25	30	N/A	N/A

### 5.3.2 Model comparison

#### (1) Thomas model

The Thomas model[56] is one of the most widely used models to evaluate column performances. The Thomas model was derived from the mass conservation equation in a

continuous flow system, which demands that the solute entering a layer  $dx$  of the fixed-bed column in time  $\delta t$  be accounted for as follows:

$$cu\delta t = (c + \frac{\partial c}{\partial x} dx)u\delta t + mdx \frac{\partial c}{\partial t} \delta t + dx \frac{\partial q}{\partial t} \delta t \quad (5-4)$$

in which  $c$  (mmol/mL) is the concentration of solution,  $u$  (mL/min) is the flow rate,  $x$  (g) is the mass of the adsorbent contained therein, indicating the distance from the input end of the fixed-bed column,  $q$  (mmol/mg) is the concentration of adsorbed material, and  $m$  (mL/g) is the free space or the pore volume of the adsorbent. Therefore,

$$\frac{\partial c}{\partial x} + \frac{m}{u} \frac{\partial c}{\partial t} + \frac{1}{u} \frac{\partial q}{\partial t} = 0 \quad (5-5)$$

For constant flow rate, the equation can be rewritten as,

$$\frac{\partial c}{\partial x} + m \frac{\partial c}{\partial V} + \frac{\partial q}{\partial V} = 0 \quad (5-6)$$

where  $V$  (mL) is the volume of the outflow.

Assuming that adsorption rate is determined by the chemical reaction, i.e. the diffusion is not a rate-determining factor, and equilibrium adsorption follows the Langmuir isotherm, and the adsorption obeys pseudo second order reversible reaction kinetics, the expression of the Thomas model was obtained after a series of complicated derivation steps,

$$\frac{C_t}{C_0} \approx \frac{1}{1 + \exp \left[ \frac{k_{Th}}{u} (Q_0 M - C_0 V_{eff}) \right]} \quad (5-7)$$

where  $C_0$  (mg/L) is initial concentration of adsorbate,  $C_t$  (mg/L) is the concentration of adsorbate in the effluent at time  $t$ ,  $k_{Th}$  (mL/mg min) is the Thomas rate constant,  $u$  (mL/min) is the flow rate,  $Q_0$  (mg/g) is the equilibrium adsorbate uptake onto unit mass

of adsorbent,  $M$  (g) is the mass of adsorbent in fixed-bed column, and  $V_{eff}$  (mL) is the volume of treated solution at time  $t$ .

The Thomas model can be linearized to the following form:

$$\ln\left(\frac{C_0}{C_t} - 1\right) = \frac{k_{Th}Q_0M}{u} - \frac{k_{Th}C_0V_{eff}}{u} \quad (5-8)$$

Plotting  $\ln\left(\frac{C_0}{C_t} - 1\right)$  against  $V_{eff}$ ,  $k_{Th}$  and  $Q_0$  can be assessed by the slope and intercept.

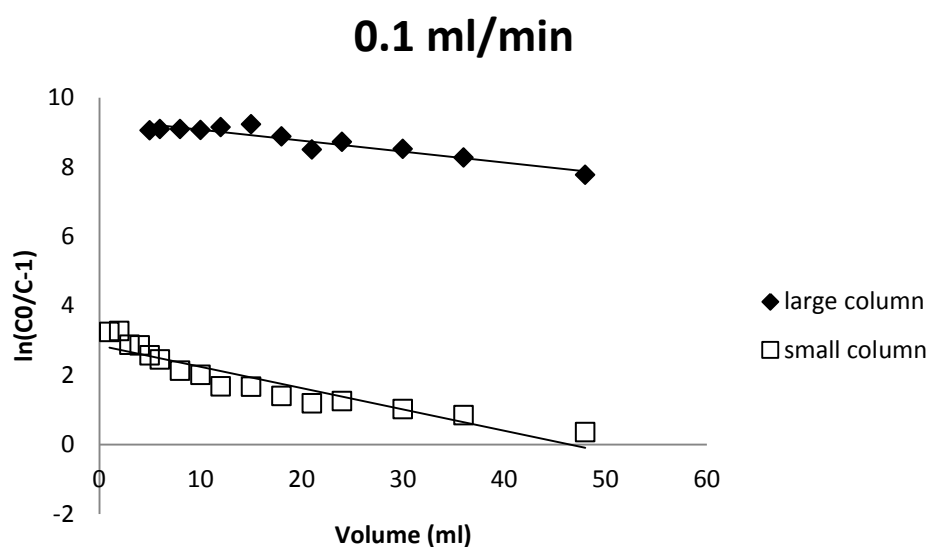
The Thomas model is mainly used to predict the breakthrough curve and estimate the maximum adsorption  $Q_0$ .

Figure 5-6, Figure 5-7 and Figure 5-8 show the plots of  $\ln\left(\frac{C_0}{C_t} - 1\right)$  against the volume of effluent  $V_{eff}$  in the large and small columns with 0.1 mL/min, 0.25 mL/min and 1 mL/min

flow rate, respectively. Linear relationships between  $\ln\left(\frac{C_0}{C_t} - 1\right)$  and  $V_{eff}$  being observed with the values of  $R^2$  mostly close to unity suggests that the Thomas model is suitable to describe copper ion adsorption on to alginate beads in a continuous fixed-bed column system. The Thomas rate constant  $k_{Th}$  and the maximum adsorption  $Q_0$  for each column were acquired from the slope and the intercept of the linear fitting and listed in Table 5-2. Because of the limited residence time in the small column with 1 mL/min flow rate, incomplete adsorption occurred in that column. Therefore, the Thomas model failed to evaluate its adsorption process.

From the statistical data presented in Table 5-2, it can be seen that the Thomas rate constant  $k_{Th}$  slightly increased with the increase of flow rate. However, regardless of the

column size and flow rate, the values of  $k_{Th}$  varied within the same scale and averaged approximately at 0.09 mL/mg min. The insensitivity of the Thomas rate constant to the flow rate supports the assumption of the chemical reaction being the rate controlling step. In addition, it was found that the values of maximum adsorption capacity  $Q_0$  for all columns with varied flow rate were smaller than equilibrium data obtained in the batch adsorption experiment, indicating that the Thomas model yielded realistic values for the fit parameters, but may somewhat underestimate the maximum adsorption capacity in a continuous fixed-bed column of alginate beads.



**Figure 5-6.** Linear Thomas model fit to adsorption data of the large column and small column at a flow rate of 0.1 mL/min.

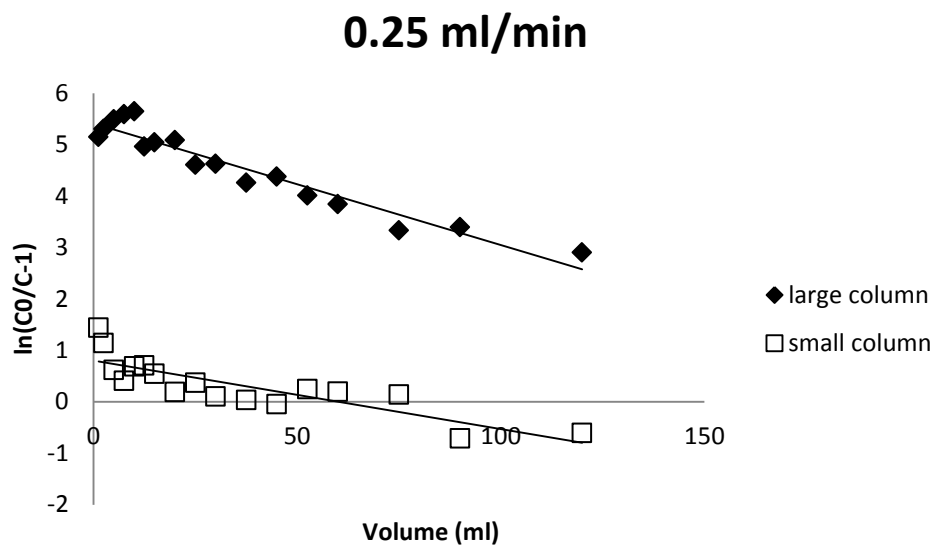


**Figure 5-7.** Linear Thomas model fit to adsorption data of the large column and small column at a flow rate of 0.25 mL/min.

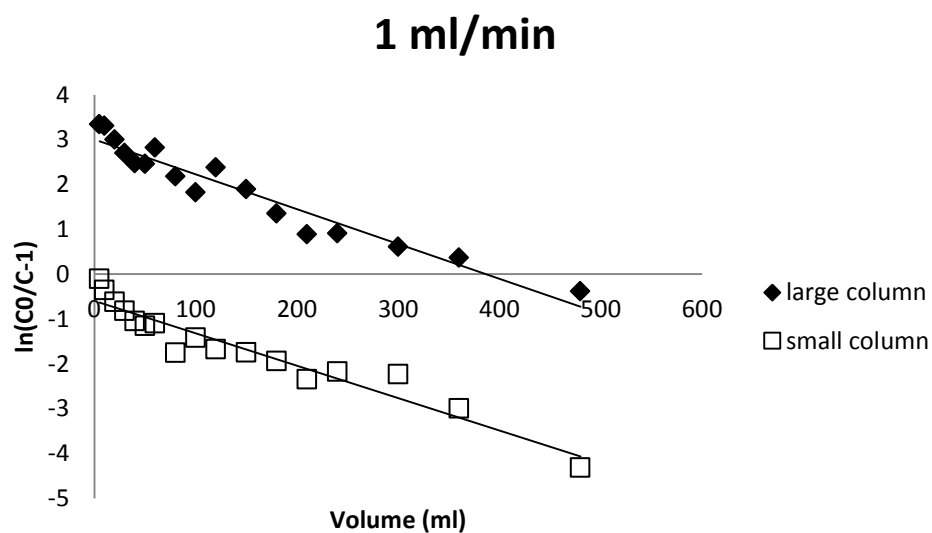


**Figure 5-8.** Linear Thomas model fit to adsorption data of the large column and small column at a flow rate of 1 mL/min.

**Table 5-2.** Statistical data of the Thomas model fit to large columns and small columns at the flow rates of 0.1 mL/min, 0.25 mL/min and 1 mL/min.

		$Q_0$ (mg/g)	$k_{Th}$ (mL/mg min)	$R^2$	Estimated Breakthrough Time (min)	Experimental Breakthrough Time (min)
Large Column	0.1 mL/min	5.35	0.049	0.89	2050	>> 480
	0.25 mL/min	3.90	0.093	0.92	420	480
	1 mL/min	6.99	0.123	0.93	10	25
Small Column	0.1 mL/min	6.56	0.097	0.87	10	30
	0.25 mL/min	8.91	0.052	0.71	N/A	N/A
	1 mL/min	N/A	0.113	0.92	N/A	N/A

The Thomas model is widely used to predict the breakthrough curve and the maximum solute uptake by the adsorbent. Figure 5-9 presents the predicted breakthrough curves of the large column with 0.1 mL/min, 0.25 mL/min and 1 mL/min flow rate, while Figure 5-10 shows the predicted breakthrough curves of the small column with 0.1 mL/min and 0.25 mL/min flow rate. By using the curves in Figure 5-9 and Figure 5-10, the volume of effluent when breakthrough occurred can be easily estimated. Assuming that the flow rate was constant, breakthrough time was calculated and listed in Table 5-2 and was found to be a good agreement with the experimental breakthrough time. In addition, the breakthrough time for the 0.1 mL/min large column was predicted by the Thomas model, even though the experimental data was not sufficient to yield that value.

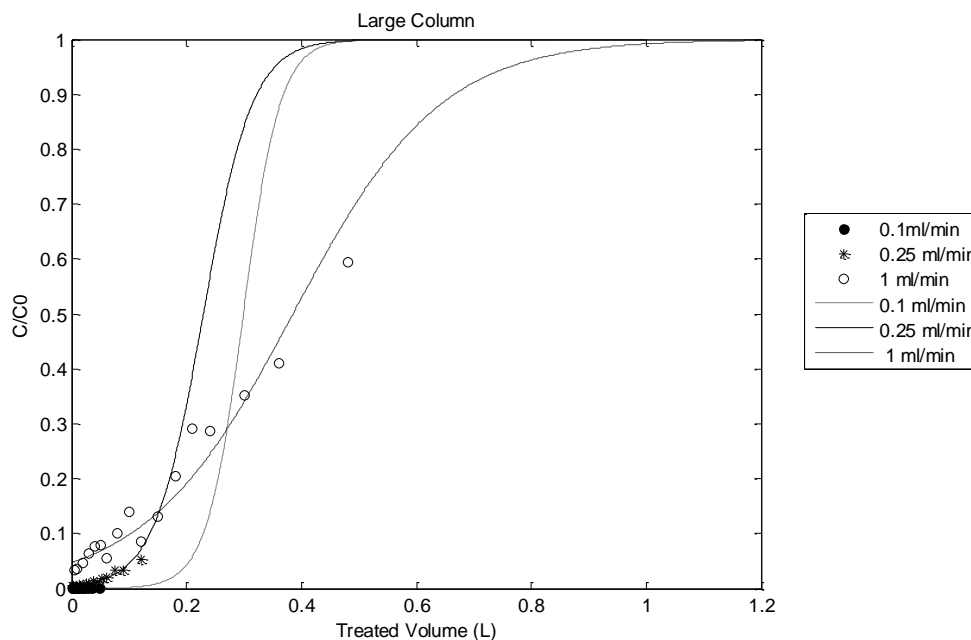


**Figure 5-9.** Predicted breakthrough curves of the large column at 0.1 mL/min, 0.25 mL/min and 1 mL/min flow rate by the Thomas model.

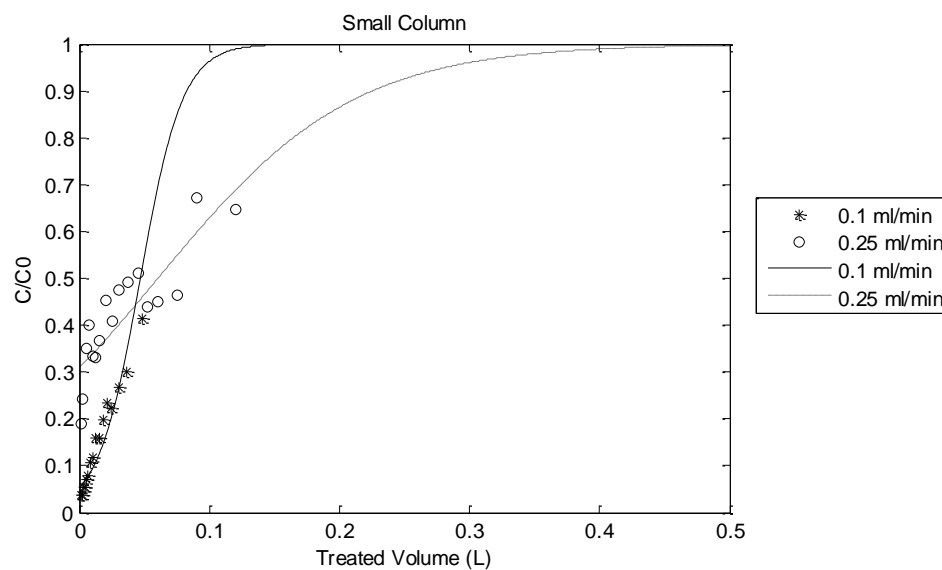


**Figure 5-10.** Predicted breakthrough curves of the small column at 0.1 mL/min, 0.25 mL/min and 1 mL/min flow rate by the Thomas model.



## (2) Adams-Bohart model

The Adams–Bohart model[57] is another widely applied model for fixed-bed column adsorption. Adams and Bohart proposed a relationship between  $C/C_0$  and  $t$  in a continuous flow system for gas adsorption on carbon. The model assumes that the rate-limiting step is chemical reaction on the surface, and the adsorption process follows pseudo-second order irreversible reaction. The adsorption reaction rate is  $k_{AB}qc$ .

Considering a selected portion of adsorbent, the residual adsorption capacity decreases at the rate given by following equation,

$$\frac{\partial c}{\partial x} = -\frac{k_{AB}}{u}qc \quad (5-9)$$

where  $q$  is residual adsorption capacity (mg/L),  $c$  is the solution concentration at time  $t$  and distance from inflow entrance  $x$  (m),  $u$  (m/min) is the superficial flow rate, and  $k_{AB}$  (mL/mg min) is the Adams-Bohart rate constant. After integration, the linear form of the Adams-Bohart model can be written as:

$$\ln\left(\frac{C_0}{C_t} - 1\right) = \ln(e^{k_{AB}Q_0Z/u} - 1) - k_{AB}C_0t \quad (5-10)$$

where  $C_0$  (mg/L) is the initial concentration of adsorbate,  $C_t$  (mg/L) is the concentration of adsorbate in the effluent at time  $t$ ,  $Q_0$  (mg/L) is the equilibrium adsorbate uptake onto unit volume of adsorbent, and  $Z$  (m) is the height of the fixed-bed column. The Adams-Bohart model is mostly used to describe the initial part of the breakthrough curve in a fixed-bed column system. One advantage of the Adams-Bohart model is that it indicates the breakthrough time straightforwardly.

The breakthrough data from column studies for large and small columns with 0.1 mL/min, 0.25 mL/min and 1 mL/min flow rate were fit to the Adams-Bohart model shown in Figure 5-11 and Figure 5-2. Since the prediction curves in Figure 5-11 and Figure 5-12 show that the large column with 1 mL/min flow rate and small columns with 0.1 and 0.25 mL/min flow rate went far beyond the breakthrough point, only the initial period adsorption data (0 to 200 minutes) were adopted when using the Adams-Bohart model to evaluate those columns. The Adams-Bohart constant  $k_{AB}$  and the equilibrium adsorbate uptake on to a unit volume of adsorbent  $Q_0$  (mg/L) were obtained from linear regression analysis, and the estimated breakthrough time was directly read from Figure 5-11 and Figure 5-12. To compare with the Thomas model,  $Q_0$  (mg/L) was converted to the equilibrium adsorbate uptake on to a unit mass of adsorbent  $Q_0$  (mg/g) based on the density of alginate gel particles and presented in Table 5-3 with other parameters. The Adams-Bohart model exhibited fairly good agreement with experimental data. Compared with the Thomas model, the Adams-Bohart model predicted a more accurate breakthrough time than the Thomas model since it only used the initial period of the data set, where the concentration of the outflow changed significantly and the samples were taken densely. The estimated maximum adsorption capacity  $Q_0$  (mg/g) was lower than equilibrium experimental data, even more so than the values from the Thomas model.

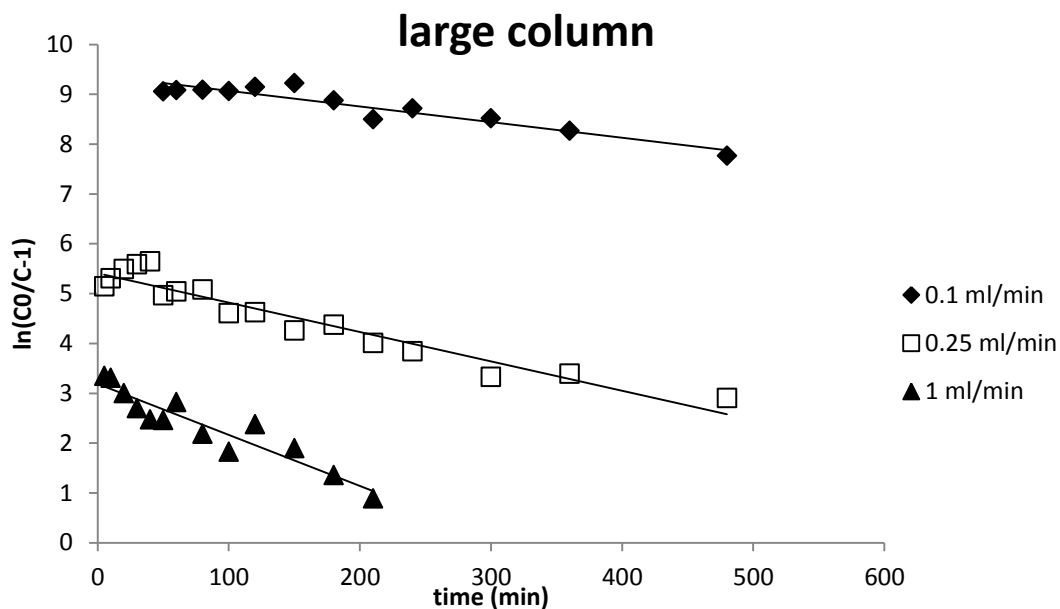


**Figure 5-11.** Linear Adams-Bohart model fit to adsorption data of the large column at flow rates of 0.1 mL/min, 0.25 mL/min and 1 mL/min.

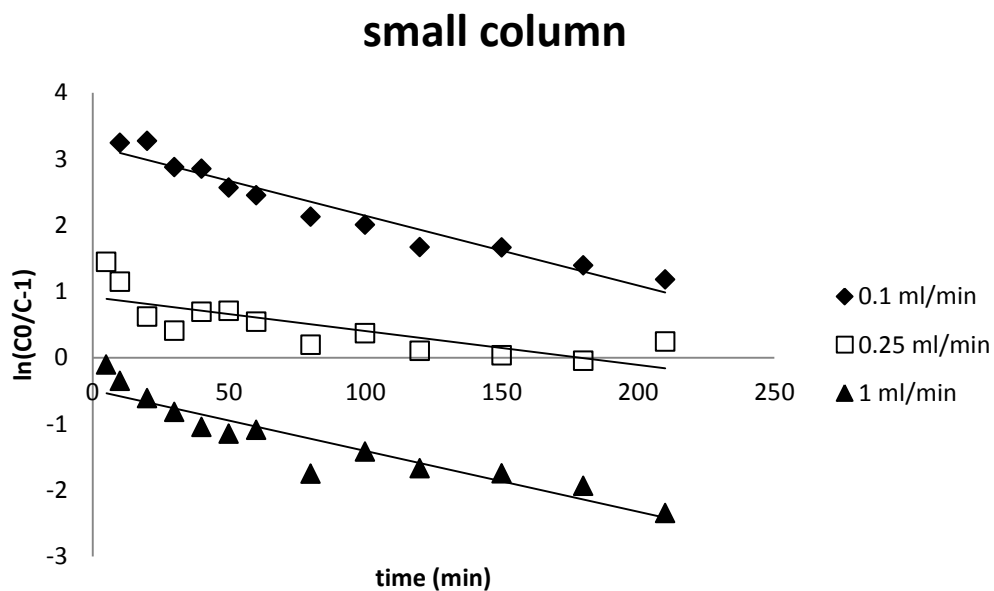


**Figure 5-12.** Linear Adams-Bohart model fit to adsorption data of the small column at flow rates of 0.1 mL/min, 0.25 mL/min and 1 mL/min.

**Table 5-3.** Statistical data of the Adams-Bohart model fit to the large columns and small columns at the flow rates of 0.1 mL/min, 0.25 mL/min and 1 mL/min.

		$Q_0$ (mg/g)	$k_{AB}$ (mL/mg min)	$R^2$	Estimated Break- through Time (min)	Experimental Break- through Time (min)
Large Column	0.1 mL/min	5.42	0.049	0.89	N/A	>> 480
	0.25 mL/min	3.90	0.093	0.92	420	480
	1 mL/min	5.69	0.162	0.88	25	25
Small Column	0.1 mL/min	4.35	0.165	0.94	25	30
	0.25 mL/min	9.08	0.080	0.62	N/A	N/A
	1 mL/min	N/A	0.145	0.87	N/A	N/A

(3) Yoon-Nelson model

Yoon and Nelson developed a simple model to describe the adsorption of adsorbate gases on to activated charcoal[58]. They denoted  $Q$  as the probability for adsorption and  $P$  as the probability for breakthrough. In other words,  $Q$  is the fraction of the inflow that gets adsorbed and  $P$  is the fraction of the inflow that flows out of the column. This model assumed that the rate of decrease in the probability of adsorption for each adsorbate molecule is proportional to  $Q$  and  $P$ , shown as:

$$-\frac{dQ}{dt} = k_{YN}QP \quad (5-11)$$

Since  $P=1-Q$ , the following equation was obtained:

$$\int \frac{dQ}{Q} + \int \frac{dQ}{1-Q} = -\int k_{YN}dt \quad (5-12)$$

After integration, the equation became:

$$\ln\left(\frac{Q}{1-Q}\right) = k_{YN}(\tau - t) \quad (5-13)$$

where  $k_{YN}$  ( $\text{min}^{-1}$ ) is the rate constant and  $\tau$  is a constant. Note that when  $Q=0.5$ ,  $\tau=t$ .

Therefore,  $\tau$  is the time required for 50% adsorbate breakthrough. Plugging  $Q = \frac{1-C_t}{C_0}$

into the equation, the linear form of Yoon-Nelson model is expressed as:

$$\ln\left(\frac{C_t}{C_0 - C_t}\right) = k_{YN}t - \tau k_{YN} \quad (5-14)$$

The Yoon-Nelson model is always used to predict 50% adsorbate breakthrough time.

In Figure 5-13 and Figure 5-14, the values of  $\ln(C_t/C_0 - C_t)$  from large and small columns were plotted against adsorption time  $t$ . The Yoon-Nelson constants  $k_{YN}$  and  $\tau$  were estimated and listed in Table 5-4. The linear relationship between  $\ln(C_t/C_0 - C_t)$  and  $t$  demonstrates that the Yoon-Nelson model is a suitable model to describe the continuous adsorption in a fixed-bed column system. In addition, the values of  $\tau$  show good agreement with the experimental 50% breakthrough times.

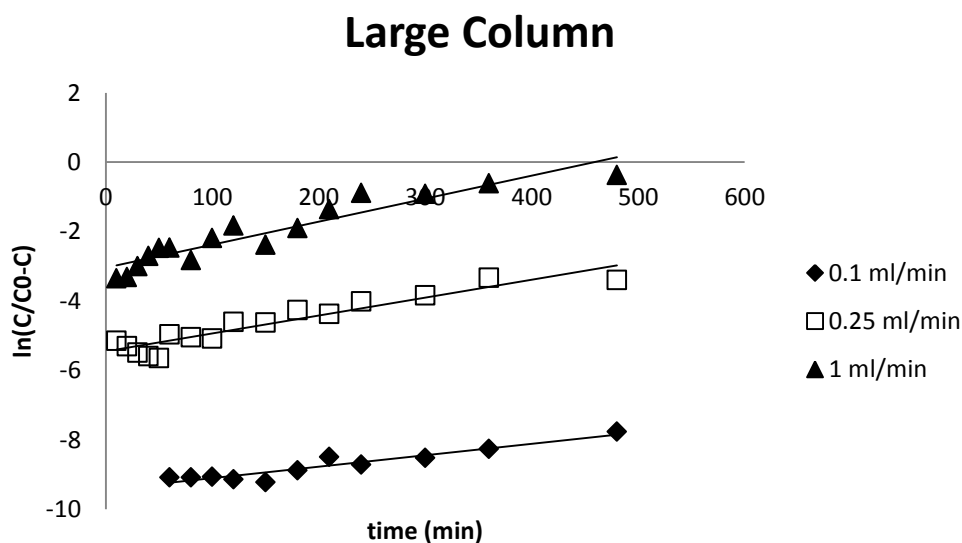


**Figure 5-13.** Linear Yoon-Nelson model fit to adsorption data of the large column at flow rates of 0.1 mL/min, 0.25 mL/min and 1 mL/min.

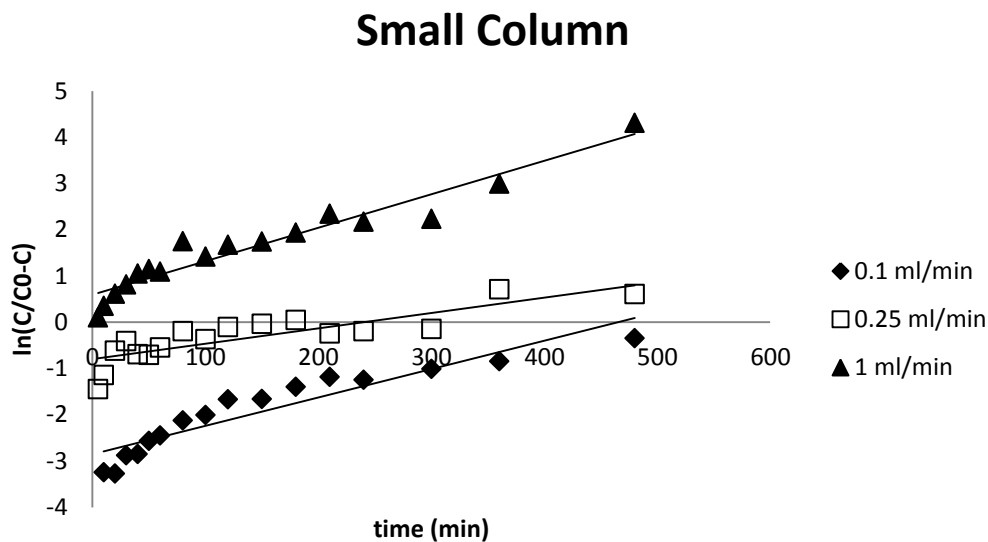


**Figure 5-14.** Linear Yoon-Nelson model fit to adsorption data of the small column at flow rates of 0.1 mL/min, 0.25 mL/min and 1 mL/min.

**Table 5-4.** Statistical data of the Yoon-Nelson model fit to the large columns and small columns at the flow rates of 0.1 mL/min, 0.25 mL/min and 1 mL/min.

		$k_{YN} \text{ (min}^{-1}\text{)}$	$\tau \text{ (min)}$	$t_{exp.} \text{ (min)}$	$R^2$
Large Column	0.1 mL/min	0.0033	2858	>> 480	0.90
	0.25 mL/min	0.0052	1049	>> 480	0.89
	1 mL/min	0.0066	461	~430	0.89
Small Column	0.1 mL/min	0.0061	468	~ 480	0.87
	0.25 mL/min	0.0033	242	~ 300	0.71
	1 mL/min	0.0072	N/A	< 5	0.92

Comparing the Thomas model and the Adams-Bohart model, which have similar forms of model equations, both the Thomas model and the Adams-Bohart model are able to estimate the maximum adsorption capacity of the adsorbent. The Thomas model was derived from a general mass conservation equation with the assumption of Langmuir isotherm and pseudo-second order reversible reaction, while the Adams-Bohart model was simply deduced from pseudo-second order irreversible adsorption kinetics.

Therefore, the comprehensive factors included in the Thomas model makes it more accurate to fit the experimental data. Besides, it was found that the values of the maximum adsorption capacity and adsorption rate constant in the continuous fixed-bed column are not consistent with those in the batch system. The values of maximum adsorption capacity calculated by both the Thomas model and the Adams-Bohart model are smaller than that in the batch system. The smaller values fit from the continuous flow experiments are not necessarily an error from the models but instead may indicate the existence of flow bypass in the fixed-bed experiment. Due to uneven flow patterns in the column, some large calcium-alginate beads may not have the chance to contact with the copper sulfate solution sufficiently, causing the underestimation of the maximum adsorption capacity by the Thomas model and the Adams-Bohart model. The bypass phenomenon may also lead to the underestimation of the pseudo-second order rate constant. In addition, since a continuous fixed-bed column is not a well-stirred system, the diffusion resistance may not be negligible. This idea conflicts with the assumption of chemisorption being the rate controlling step in the Thomas model and the Adams-Bohart model. This possible significance of diffusion resistance is supported by the fact that in spite of perfect data fitting to the pseudo-second order equation in a batch system, the values of the correlation coefficients of the experimental data fitting to the Thomas model and the Adams-Bohart model in continuous fixed-bed columns are only around 0.9.

The Yoon-Nelson model is quite simple and straightforward. It assumes that the adsorption equilibrium occurs instantaneously, and that the adsorption in a fixed-bed column is homogeneous and uniform. Despite this defective assumption, the Yoon-

Nelson model successfully gave relatively good fits to the adsorption data in this study. In fact, all three models are valuable and informative to the study of continuous fixed-bed column adsorption, since they provide prominent and unique characteristic features respectively, such as adsorption capacity (Thomas model, Adams-Bohart model), breakthrough curve without sufficient data (Thomas model), service time (Adams-Bohart model) and time for 50% breakthrough (Yoon–Nelson model).

## 5.4 Summary

In this chapter, the adsorption behavior of fixed-bed columns packed with large calcium-alginate gel beads was studied by varying the column size and volumetric flow rate. The results show that when flow rate was high, the adsorption was performed relatively uniformly in the fixed-bed column, and the fixed-bed column might reach saturation at the end of experiment. For the low flow rate case, adsorption mainly occurred near the inlet region of the column. In the aspect of breaking through, a column had shorter active life at a higher flow rate, or a smaller size.

There are two main factors to evaluate the efficiency of a fixed-bed column: BV number and breakthrough time. A column with high BV number at breakthrough and moderate breakthrough time is believed to be well-performing. Therefore, there is an optimal flow rate for a certain size of column. Below that, the breakthrough time would be too long and volume of treated solution would be deficient, while above it, the BV number would



be small and the adsorbent would not be used efficiently. In this study, the best tested fixed-bed column is the large column at 0.25 mL/min flow rate.

Moreover, the Thomas model, the Adams-Bohart model and the Yoon-Nelson model were used to fit experimental data. All three models were proven to be suitable to describe the adsorption behavior of fixed-bed columns. They also provided unique characteristic features respectively, such as adsorption capacity (Thomas model, Adams-Bohart model), breakthrough curve without sufficient data (Thomas model), service time (Adams-Bohart model) and time for 50% breakthrough (Yoon–Nelson model).

## Chapter 6 Rheology of a Concentrated Bimodal Suspension Containing Rigid and Soft Particles

### 6.1 Introduction

Suspensions play an important role in industry and in our daily lives, from drug manufacturing to painting. The rheological properties, especially the relative viscosity of suspensions, have drawn much attention over the past century. There have been many investigations trying to predict and correlate the viscosities of various suspensions with the rigid particle volume fraction and maximum packing particle volume fraction by theoretical and experimental approaches [65-74].

Two commonly used viscosity models are the Maron-Pierce-Kitano model [66, 71] and the Zarraga model [73]. The Maron-Pierce-Kitano model has a simple form to describe the relative viscosity  $\eta_r$  as a function of the volume fraction of particles  $\phi$  and the random close packing fraction  $\phi_{rcp}$  for monodisperse suspensions, shown in Equation (6-1).

$$\eta_r = \frac{\eta}{\eta_0} = \left(1 - \frac{\phi}{\phi_{rcp}}\right)^{-2} \quad (6-1)$$

The Zarraga model has a similar expression to the Maron-Pierce-Kitano model. It adjusted the power from Equation (6-1) and scaled it by  $e^{-2.34\phi}$  as seen in Equation (6-2).

$$\eta_r = \frac{e^{-2.34\phi}}{(1 - \frac{\phi}{\phi_{rcp}})^3} \quad (6-2)$$

The parameter  $\phi_{rcp}$  in Equations (6-1) and (6-2) was determined by fitting each equation to the experimental data or by measuring the value experimentally. The Maron-Pierce-Kitano model, the very similar Krieger model[68] and the Zarraga model have shown good agreement to experimental data for monomodal suspensions.

In fact, bimodal mixtures are more representative of practical particulate systems than monomodal dispersions. Bimodal suspensions are found in a variety of biological and industrial applications, such as blood flow through vessels, mineral transport through plant xylem and the manufacture of petrochemicals, polymers, ceramics, pharmaceuticals, flavors and many other products. The distinguishing feature of a bimodal suspension is that its relative viscosity depends on not only the bulk particle volume fraction and maximum packing volume fraction of the particles, but also the size ratio of the two types of particles and the relative volume fraction of the particles. Therefore, several parameters can be varied in order to enhance packing or tune the viscosity of a flow by adjusting the composition of a bimodal suspension.

Some research has been reported on the rheological properties of bimodal suspensions. Chong *et al.*[75] identified the diameter ratio of large to small spheres  $\lambda$  and volume fraction of smaller particles  $\xi\phi_v$  as two important parameters to characterize a bimodal particle mixture. They found that when  $\xi=0.25$  and the bulk volume fraction  $\phi_v$  was fixed,

the viscosity of concentrated suspensions decreased as the particle size ratio  $\lambda$  increased from 1.0 to 7.25, and there was no significant viscosity change when  $\lambda > 10$ . The investigators believed that an optimum value of  $\zeta$  existed to minimize the suspension viscosity when  $\lambda$  and  $\phi_v$  were fixed. Storms *et al.* [76] measured the viscosity of bimodally distributed poly(methylmethacrylate) (PMMA) suspensions in silicone oil at low shear rate over a large range of particle volume fractions. They observed the concentration dependence of the relative viscosity and quantitatively predicted the effect of  $\lambda$  and  $\zeta$  on the viscosity of bimodal suspensions. Chang and Powell [77] found that, for a fixed bulk volume fraction of particles, the viscosities of bimodal suspensions were always less than the viscosities of monomodal suspensions. Moreover, they provided additional experimental data for highly concentrated suspensions ( $\phi_v = 0.67$ ) showing that the bimodal size distribution of particles could have an effect not only on the shear viscosity but also on the transient properties of filled suspension systems.

Bimodal suspension systems are also known for particle size separation, owing to the action of shear-induced particle migration in a nonuniform shear flow. Larger particles tend to migrate more quickly to low stress regions, leaving behind the smaller particles. Size separation of otherwise identical particles has been observed in tube flow, concentric cylinder flow and free surface flow [78], channel flow [79], and torsional flow between parallel plates [80]. Shauly *et al.* [81] developed a model to describe the shear-induced particle migration in a polydisperse concentrated suspension, which was applicable to solve the flow patterns and the particle concentration distributions in bidisperse suspensions in various viscometric flows. They found that the total energy dissipation rate and, therefore, the power required to drive the flow were diminished considerably at

steady state. The drift velocity arising from shear-induced particle migration in a monomodal suspension is typically estimated as  $(a \phi \dot{\gamma})$ , where  $a$  is the particle radius,  $\phi$  the particle volume fraction and  $\dot{\gamma}$  the shear rate [82].

In addition to the experimental investigations on the rheological properties of bimodal suspensions, many studies have focused on the theoretical prediction of the relative viscosities of bidisperse suspensions. Farris [83] first proposed a model to estimate the viscosity of multi-modal systems in terms of the viscosity of its components, in which fine particles in suspension were viewed as a continuum and a maximum volume fraction parameter was not involved. Farris's model was further modified by D'Haene and Mewis [84] and also by Zaman and Moudgil [85, 86] to take particle interactions into account. Chong *et al.* [75] and Sudduth [87] suggested that the particle size distribution (the diameter ratio of large to small spheres), the volume fraction of small particles, and maximum packing fraction are important parameters to characterize a bimodal suspension. The value of the maximum packing fraction is an empirical quantity, and a wide range of values has been established [73, 75-77, 88-91]. In this paper, 0.62 was used as the maximum packing fraction for monomodal suspensions, consistent with Zarraga's results.

Recently, Qi and Tanner [92] developed a new model to estimate the maximum random close packing of a bidisperse system. In their model, they successfully related the value of the maximum packing fraction of bimodal system  $\phi_{bm}$  to that of monomodal system  $\phi_{rcp}$  by the following equation

$$\varphi_{bm} = \varphi_{rcp} + \xi_k \xi_\lambda \varphi_{rcp} (1 - \varphi_{rcp}) \quad (6-3)$$

where  $\xi_k$  is a function of the relative volume fraction of small particles  $k$  and  $\xi_\lambda$  is a function of the particle size ratio  $\lambda$ , which can be calculated by equations (6-4) and (6-5).

$$\xi_\lambda = 1 - e^{-\frac{(\lambda-1)^{1/3}}{6}} \quad (6-4)$$

$$\xi_k = \begin{cases} 1 - \frac{1}{0.0729} (k - 0.27)^2 & k \leq 0.27 \\ 1 - \frac{1}{0.284} (k - 0.27)^4 & k > 0.27 \end{cases} \quad (6-5)$$

Once the value of  $\varphi_{bm}$  is attained, Qi and Tanner assess the relative viscosity of bimodal system by using the Mendoza and Santamaria-Holek model [74], shown in equation (6-6) and (6-7).

$$\eta_r = \left(1 - \frac{\varphi}{1 - c\varphi}\right)^{-\frac{5}{2}} \quad (6-6)$$

in which

$$c = \frac{1 - \varphi_{rcp}}{\varphi_{rcp}} \quad (6-7)$$

and  $\varphi$  is the volume fraction of particles.

Then, the relative viscosity of a bimodal system is defined by equation (6-8), as a product of two functions

$$\eta_r = \frac{\eta(\varphi_l, \varphi_s)}{\eta_0} = \frac{\eta(\varphi_l)}{\eta_0} \frac{\eta(\varphi_l, \varphi_s)}{\eta(\varphi_l)} = H(l/0)H(s/l) \quad (6-8)$$

where  $\eta(\varphi_l, \varphi_s)$  is the viscosity of the bimodal suspension,  $\eta(\varphi_l)$  is the viscosity of a suspension containing only the large particle fraction, and  $\eta_0$  is the viscosity of the suspending fluid.

Each function can be computed by Mendoza and Santamaria-Holek model respectively from the following equations.

$$H(l/0) = \left(1 - \frac{\varphi_l}{1 - c_l \varphi_l}\right)^{\frac{5}{2}} \quad (6-9)$$

$$c_l = \frac{1 - \varphi_{rcp}}{\varphi_{rcp}} \quad (6-10)$$

$$H(s/l) = \left(1 - \frac{\varphi_s}{1 - c_s \varphi_s}\right)^{\frac{5}{2}} \quad (6-11)$$

It is important to notice that  $H(s/l)$  is not the relative viscosity of the small particle fraction. In other words, the suspension “matrix” consists of suspending fluid and large particles instead of only suspending fluid by itself. Hence, the random close packing fraction of the small particles is no longer  $\varphi_{rcp}$ . It should be adjusted to  $(\varphi_{bm} - \varphi_l)$  because of the presence of the large particles.

$$c_s = \frac{1 - (\varphi_{bm} - \varphi_l)}{\varphi_{bm} - \varphi_l} \quad (6-12)$$

By substituting Equation (6-9), (6-10), (6-11) and (6-12) into Equation (6-8), the relative viscosity of a bimodal suspension is given by

$$\eta_r = \left[ \left(1 - \frac{\varphi_l}{1 - c_l \varphi_l}\right) \left(1 - \frac{\varphi_s}{1 - c_s \varphi_s}\right) \right]^{-\frac{5}{2}} \quad (6-13)$$

This new model developed by Qi and Tanner was compared to experimental data obtained by Chang and Powell [77], Chong *et al.*[75], and Poslinski *et al.*[89]. Reasonably good agreement was found and reported.

Although many theoretical models have been derived and have provided good estimation of experimental data, most published studies have concentrated on bimodal suspensions of noncolloidal, rigid particles. Bimodal suspensions containing both rigid and soft particles have rarely been discussed, and almost always in the context of cell margination in blood flow [93-95]. Soft particles typically are porous or deformable and contain colloidal-scale structure. In contrast to rigid particle suspensions, when a suspension contains both rigid and soft particles, it can exhibit strongly shear-dependent properties even at moderate particle volume fraction, due to the deformability of the soft particles and the interaction between rigid and soft particles. Therefore, the relative viscosity and shear-dependence of rigid and soft particle suspensions are very sensitive to the bulk particle volume fraction and relative volume fraction of the rigid and soft particles.

In this Chapter, the relative viscosity was measured for bimodal suspensions consisting of rigid, large PMMA particles and soft, small alginate gel beads with varied relative volume fraction and bulk concentration. The rheological properties of rigid/soft particle bimodal suspensions were discussed. In order to quantitatively predict the relative viscosity of a rigid and soft particle bimodal suspension, a new version of the Qi and



Tanner model [92] adapted for such systems was developed and good agreement with experimental data was achieved.

## **6.2 Experimental Methods**

### **6.2.1 Materials**

The bimodal suspension used for the rheology experiment was a mixture of poly(methylmethacrylate) (PMMA) rigid particles and alginate gel beads of varying volume ratios with a Newtonian liquid.

To make alginate beads, three solutions were prepared: i) aqueous 2 wt% alginate solution; ii) an oil solution consisting of 69.5% (v/v) isooctane 29.5%(v/v) 1,6 dibromohexane and 1 wt% Span-80 surfactant; iii) calcium chloride solution with concentrations of 0.1M calcium chloride and 0.5 M sucrose in water. An emulsion was formed by blending equal weight amounts of the alginate solution with the oil solution at 20,000 rpm for 10 minutes (Ultra-Turrax T-25 blender, IKA Works, Staufen, Germany). The flask containing solutions was immersed in ice water during blending to prevent overheating of the mixture. The calcium chloride solution was added slowly immediately afterward to cross-link the alginate beads under magnetic stirring conditions. The emulsions were then separated in a separatory funnel with acetone washing. The alginate

suspension was extracted and centrifuged at 6000 rpm at 4 °C. The supernatant was removed and the resulting pellets were collected as alginate beads. They were stored in deionized water until sieving was performed. The alginate beads used in the experiments were smaller than 38  $\mu\text{m}$  in diameter.

The PMMA particles (Lucite 41, Lucite International, Cordova, TN) used in the experiments have an approximate density of  $1.18 \text{ g/cm}^3$ , and an average diameter of approximately 90-125  $\mu\text{m}$ . Since alginate beads are gel particles, their density is considered to be similar to that of any suspending fluid. To match PMMA particles' density and preclude buoyancy effects, a mixture of glycerin (73 wt%) and water (27 wt%) was used as the suspending fluid, which is a Newtonian fluid with viscosity  $\eta_0=0.025 \text{ Pa s}$  at 25 °C. All the samples were degassed in a vacuum oven until the visible air bubbles disappeared prior to the rheology experiments, in order to eliminate the bubbles' unwanted effects on the flow rheology.

A PMMA (25 vv% ) and alginate (25 vv% ) bimodal suspension was analyzed using a Beckman-Coulter LS-13 320 Laser Diffraction apparatus. The sample was run for combined obscuration and polarization intensity differential scattering (PIDS) analysis. A refractive index of 1.37 was input for alginate, based on measurements of the refractive index of alginate slabs. The unit was thoroughly rinsed between samples; acetone or isopropyl alcohol was used if cleaning was required. The sample was stored in glass vials and sonicated before processing and analyzed immediately after processing. The result presented in Figure 6-1 shows that the average diameter of alginate beads is around 30

$\mu\text{m}$ , while that of PMMA particles is about  $90 \mu\text{m}$ , yielding a diameter ratio of large to small particles of approximately 3.

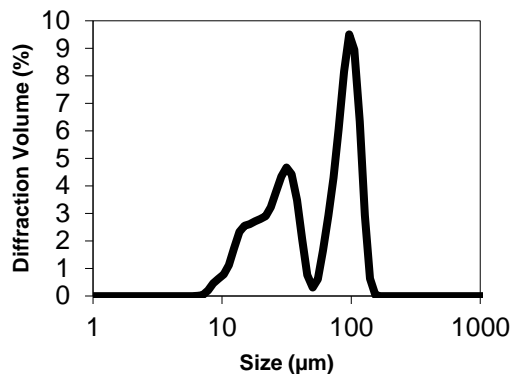


**Figure 6-1.** Size distribution of PMMA (25 vv% ) and alginate (25 vv% ) bimodal suspension measured by laser diffraction spectroscopy.

### 6.2.2 Rheological test

Testing was performed on a Kinexus Rheometer (KNX2100, Malvern Instruments). 40 mm diameter parallel plates (PL40/PU40) with a 2 mm gap were used for all samples, providing a sufficient (20:1) ratio between the sample height and the average PMMA particle diameter. Suspensions were spread evenly on the entire lower plate before contacting with upper plate, in order to avoid particle migration caused by squeezing flow [96]. The temperature was maintained at  $25^{\circ}\text{C}$  in the testing chamber. The samples' viscosity was measured under a series of logarithmically varied shear rates ranging from  $5$  to  $200 \text{ s}^{-1}$ . Reynolds numbers of the bimodal suspensions during the experiments ranged from 0.013 to 4.34 ( $Re < 1$  in most cases), and the parallel plate radius to gap ratio was 20. Therefore, the viscosity measurement of bimodal suspensions was unlikely to be

affected by secondary flow [97]. The particle Reynolds number ranged from 0.00236 to 0.0944, so the inertial effect could be neglected. Two separate scans were performed on each sample. One covered the range from low to high shear rate and the other from high to low. Each sample was pre-sheared at  $20 \text{ s}^{-1}$  for 30 seconds in order to break the microstructure formed during sample loading. The results were averaged in an attempt to avoid result sensitivity to shear history. The standard deviation of all the results ranged from 5% to 15%.

## 6.3 Results and Discussion

### 6.3.1 Monomodal suspension

Figure 6-2 presents the relative viscosity of PMMA particle suspensions as a function of shear rate ranging from 5 to  $200 \text{ s}^{-1}$ . The data are the average of those obtained from increasing and decreasing shear rate experiments, in order to eliminate sensitivity of the results to shear history. In Figure 6-2, the PMMA suspensions exhibit quasi-Newtonian fluid behavior. The viscosities of the PMMA suspensions with the bulk particle volume fraction of 10%, 20%, 30%, and 40% are nearly independent of the shear rate over the range 5 to  $200 \text{ s}^{-1}$ . The concentrated PMMA suspension, which has a bulk particle volume fraction of 50%, shows slightly shear thinning behavior under the measurement shear range, probably caused by complex interparticle interactions[98]. When the volume

fraction of PMMA suspension is high, the average interparticle distance is small. It is possible that particles may attract each other by London-van der Waals forces, and weak flocculation will form. Such complex microstructures would break down under shear, causing shear thinning behavior [99]. In addition, Blanc *et al.* [100] measured the pair distribution function in monomodal suspensions and found an increased probability of finding another particle nearby in the flow direction at high concentration (when bulk concentration is above 45%). Therefore, the alignment of PMMA particles along the flow direction may form at high concentration and lead to the shear thinning trend.

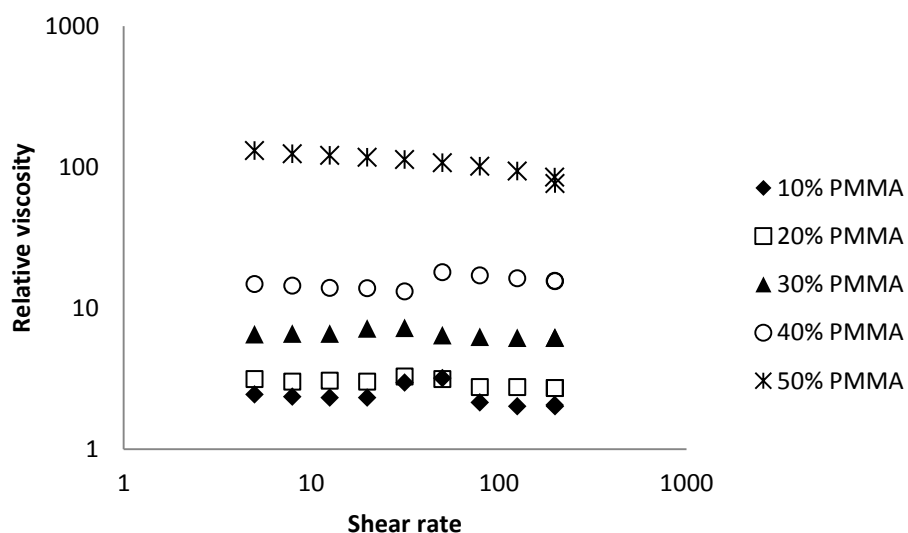


**Figure 6-2.** Relative viscosity of PMMA monomodal suspensions with particle volume fraction varying from 10% to 50%, and shear rate ranging from  $5\text{ s}^{-1}$  to  $200\text{ s}^{-1}$ .

Figure 6-3 plots the viscosities of alginate particle suspensions measured under the same conditions as the PMMA suspensions shown in Figure 6-2. Similar to the PMMA suspensions, alginate suspensions exhibit essentially Newtonian behavior. A slight shear thinning behavior was observed at high shear rate due to the porosity or deformability of

alginate beads. In contrast to rigid particles, when the shear rate increases, the suspending fluid may slip at the surface or flow through the pores of alginate beads, with a corresponding decrease observed in the relative viscosity.

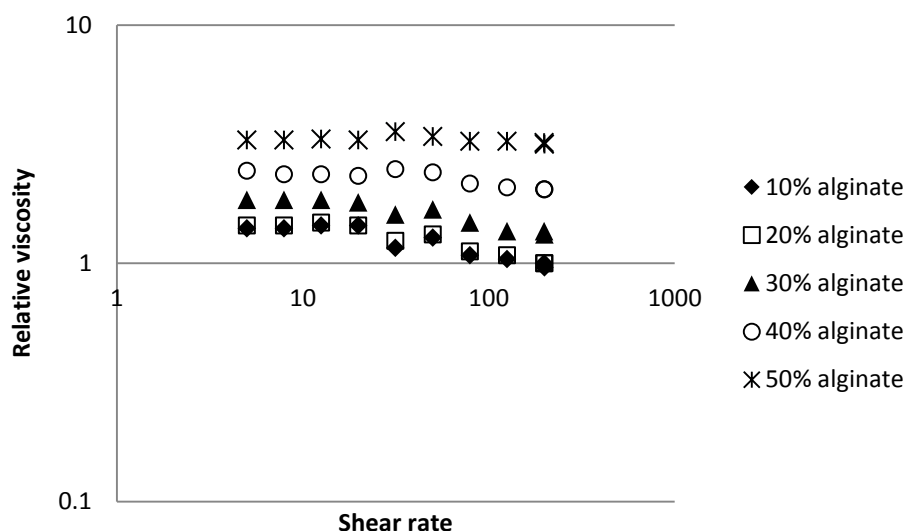


**Figure 6-3.** Relative viscosity of alginate monomodal suspensions with particle volume fraction varying from 10% to 50% and shear rate ranging from  $5 \text{ s}^{-1}$  to  $200 \text{ s}^{-1}$ .

The relative viscosity data of PMMA suspensions and alginate suspensions averaged over the range of shear rates are shown in Figure 6-4. It can be seen that the viscosities of both PMMA and alginate particle suspensions increase with an increase in volume fraction. In addition, the PMMA suspensions are more viscous than alginate suspensions at the same volume fraction, resulting from the porous and flexible structure of alginate beads, and the viscosities of PMMA suspensions increase more significantly at high volume fraction compared to those of alginate suspensions.

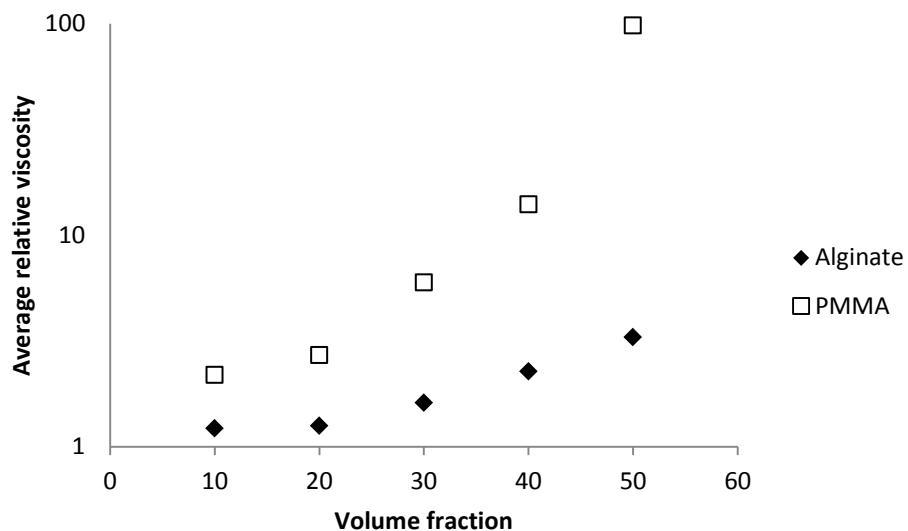


**Figure 6-4.** Average relative viscosity data of PMMA suspensions and alginate suspensions with particle volume fraction varying from 10% to 50%.

### 6.3.2 Bimodal suspension

Monomodal suspensions of either rigid PMMA particles or soft alginate beads proved to be quasi-Newtonian. These two types of particles were then mixed at various relative particle volume fractions and total bulk concentrations in the same suspending fluid, and measured under shear rates ranging from 5 to 200  $\text{s}^{-1}$ . The data presented are the average of those obtained from increasing and decreasing shear rates in order to eliminate the sensitivity of the results to shear history.

Figure 6-5 shows the change of relative viscosity of PMMA/alginate bimodal suspensions with increasing shear rate. The bulk particle volume fraction was fixed at 50%, and each curve represents a constant relative particle volume fraction. Despite the

effect of shear rate, the average viscosity of bimodal suspensions increases when the volume fraction of small particles (alginate beads) decreases at fixed bulk concentration. The plain PMMA and alginate monomodal suspensions exhibit negligible shear thinning and could be considered quasi-Newtonian suspensions. Once they are mixed, shear thinning can become significant and intense in the bimodal suspensions. Comparing the shear dependence of bimodal suspensions with varying volume fractions of small particles at fixed bulk particle volume fraction of 50%, the viscosity of bimodal suspensions with low small particle volume fraction (the volume fraction ratio of PMMA to alginate equals 45/5 and 40/10) decreased severely with increasing shear rate. When the volume fraction of small particles is high and close to 50%, the shear dependence becomes minimal and the viscosity of bimodal suspensions is approximately constant in the low shear rate region.

The shear thinning phenomenon is not included in any reported bimodal suspension viscosity models, since none of those models took the interaction between rigid and soft particles into consideration. In contrast to a bimodal suspension consisting only of rigid particles, shear thinning may occur in this system because the large, rigid PMMA particles tend to deform the small, soft alginate beads at high shear rate. The intensity of deformation would be expected to increase with increasing shear rate, thus providing extra moving space for the large, rigid particles. Effectively, the deforming soft particles are lowering the volume fraction of rigid particles, which leads to shear thinning behavior of rigid/soft bimodal suspensions. Another possible mechanism, following Blanc *et al.*'s research [100], is that the soft, small alginate beads may help PMMA particles to align



along the flow direction when the bulk concentration is high. In polymeric materials and suspensions of rods, shear thinning is often associated with alignment along the flow direction. The small, soft alginate beads may provide slip or lubrication to PMMA particles, and therefore promote the formation of layers of PMMA particles aligned with the flow direction, which can cause the significant shear thinning observed in bimodal suspensions. When the volume fraction of small particles is high, with fixed bulk concentration, the interaction between the two types of particles weakens at low shear rate resulting from the size difference of rigid and soft particles. The small alginate beads tend to act as an additional component of the “continuous phase,” with the large PMMA particles acting as the discrete phase [79]. In addition, ordering of the rigid PMMA particles is not expected for PMMA particle volume fractions below 0.45 [100]. For these suspensions, the deformation of soft small alginate particles is only noteworthy under high shear rate, demonstrated by the 15/35, 25/25, and 30/20 curves in Figure 6-5, which present shear independence at low shear rates and shear thinning at high shear rates.

It is noticeable that the shear dependence of the bimodal suspension is similar to that of PMMA monomodal suspension when the volume fraction of alginate beads is extremely low (volume fraction ratio of PMMA/alginate equals 48/2). It can be explained by the fact that below a certain volume fraction, the small soft particles can easily migrate through the interstices of large, rigid particles, so that the interaction between small and large particles is negligible. Hence, the rheological behavior of the bimodal sample is dominated by that of the large, rigid PMMA particles.

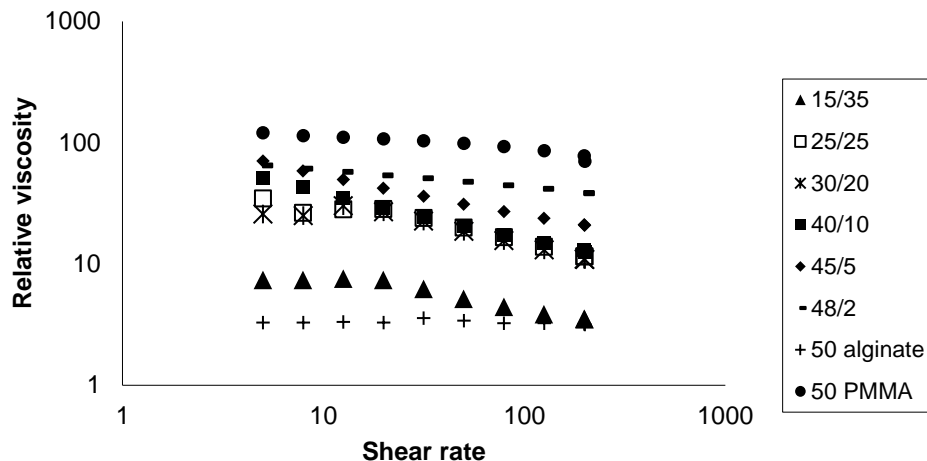


**Figure 6-5.** Relative viscosity of PMMA/alginate bimodal suspensions where the bulk particle volume fraction was fixed at 50% and the shear rate varied from  $5 \text{ s}^{-1}$  to  $200 \text{ s}^{-1}$ .

Next, the relative viscosity of rigid PMMA/soft alginate particle bimodal suspensions was measured with a fixed particle volume fraction of large, rigid PMMA particles, and a varying volume fraction of small, soft alginate beads (and therefore a varying total bulk concentration). Viscosity data points acquired at shear rates ranging from  $5 \text{ s}^{-1}$  to  $200 \text{ s}^{-1}$  were measured and plotted in Figure 6-6 and Figure 6-7.

In Figure 6-6, the volume fraction of PMMA particles was fixed at 40%, and the volume fraction of alginate beads was varied from 0 % (monomodal suspension) to 15%. The data show that the 40% PMMA suspension is only very slightly shear dependent because of nearby particle interactions. Once the alginate beads were added into the suspension, the shear thinning behavior becomes significant. Both the viscosity curves of the 40/5 (40% PMMA and 5% alginate) sample and the 40/10 (40% PMMA and 10% alginate) sample exhibit a strong shear thinning trend, and the 40/10 bimodal suspension is more intensely shear thinning than 40/5 bimodal suspension. When more alginate beads were

added into suspension, making the bulk concentration higher than 50%, the shape of the viscosity curve changed. A plateau appears at low shear rate, connected by a continuous viscosity decrease at high shear rate, as shown in the 40/15 (40% PMMA and 15% alginate) viscosity curve.

Figure 6-7 presents the viscosity data of rigid/soft bimodal suspensions when the volume fraction of PMMA particles was increased to 45%, while the variation of alginate volume fraction maintained the same with the experiment shown in Figure 6-7. It can be seen that the change in the viscosity curves of the rigid/soft bimodal suspensions with the increase in shear rate displays a similar trend with the data points in Figure 6-6. The 45% PMMA monomodal suspension reveals very slight shear thinning behavior, and the shear thinning tendency significantly intensified when a small amount of soft alginate beads were present in the suspension, as exemplified by the data points of the 45/5 (45% PMMA and 5% alginate) sample. When the bimodal suspension is concentrated and the bulk concentration is higher than 50%, the shear thinning behavior becomes minimal at low shear rate, and remains intense at high shear rate, confirmed by the curves of the 45/10 (45% PMMA and 10% alginate) and 45/15 (45% PMMA and 15% alginate) bimodal suspensions.

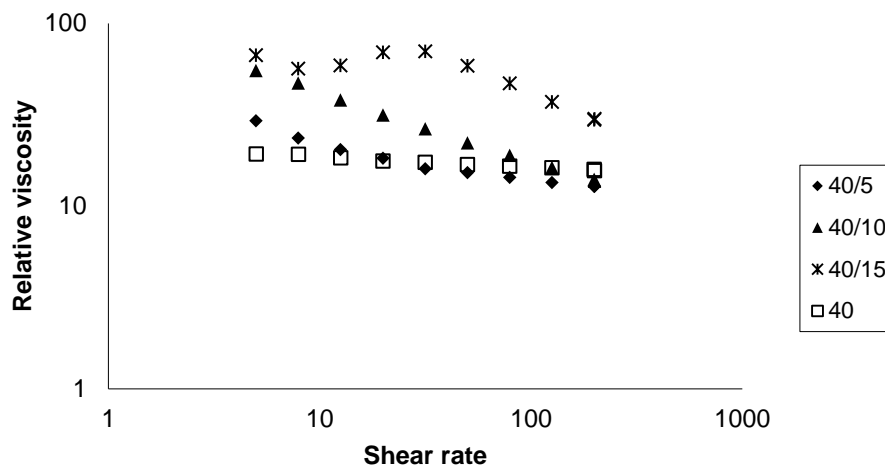


**Figure 6-6.** Relative viscosity of PMMA/alginate bimodal suspensions where the volume fraction of PMMA was fixed at 40%, and the shear rate varied from  $5\text{ s}^{-1}$  to  $200\text{ s}^{-1}$ .

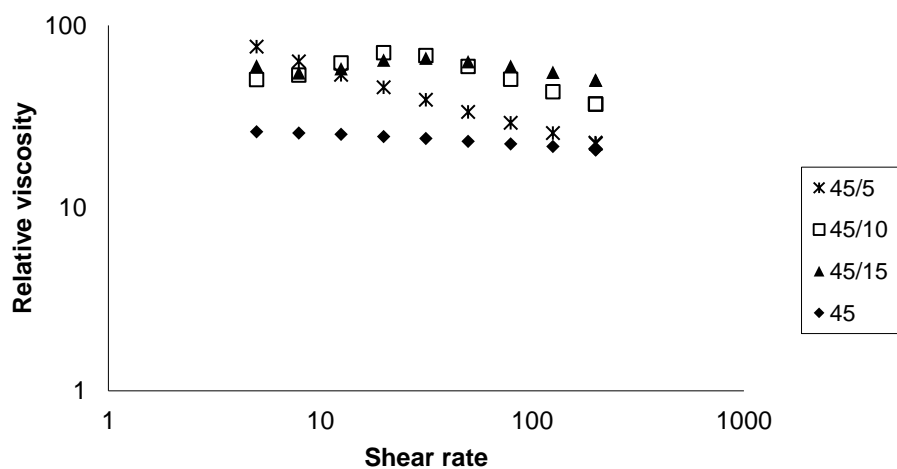


**Figure 6-7.** Relative viscosity of PMMA/alginate bimodal suspensions where the volume fraction of PMMA was fixed at 45%, and the shear rate varied from  $5\text{ s}^{-1}$  to  $200\text{ s}^{-1}$ .

By analyzing the experimental data presented in Figure 6-6 and Figure 6-7, it can be speculated that the bulk concentration can affect the rheological properties of concentrated rigid/soft particle bimodal suspensions, in addition to the relative particle

volume fraction. Therefore, a series of experiments were performed to study the sensitivity of shear dependency of rigid/soft particle bimodal suspensions to the bulk concentration. In order to rule out the effect of the volume fraction of small particles on the relative viscosity, the volume fraction of PMMA particles was altered slightly while the volume fraction of alginate beads was fixed at 10% to vary the bulk concentration. The samples' viscosity was measured under shear rates ranging from  $5 \text{ s}^{-1}$  to  $200 \text{ s}^{-1}$  and plotted in Figure 6-8. The viscosity curve of 40/10 (40% PMMA and 10% alginate) continuously decreases with the increase of shear rate, while the curves of 41/10 (41% PMMA and 10% alginate), 42/10 (42% PMMA and 10% alginate) and 45/10 (45% PMMA and 10% alginate) reveal an evolving shape, which has a plateau at low shear rate and then a decrease at high shear rate. The plateau and decreasing turning points shift to higher shear rate when the bulk concentration is increased from 51% to 55%. This experiment demonstrates that the viscosity of bimodal suspensions is very sensitive to the change of bulk concentration when it is around 50%, and the rigid/soft particle bimodal suspensions possess distinctive shear properties once the bulk concentration of bimodal suspensions is higher than 50%, consistent with the viscosity data of 40/15 (45% PMMA and 15% alginate) in Figure 6-5, 45/10 (45% PMMA and 10% alginate) and 45/15 (45% PMMA and 15% alginate) in Figure 6-6.

The effect of bulk concentration on the relative viscosity can be interpreted by the particle interaction of concentrated suspensions. At low shear rate, the collisions between PMMA and alginate particles are not strong, and alginate particles tend to act as undeformed spheres. Therefore, the viscosity of bimodal suspensions exhibits similar

quasi-Newtonian behavior to monomodal suspensions. At high shear rate, collisions among the rigid and soft particles become intense, and cause the deformation of soft particles. The deformed alginate particles may be able to slide into the interstices of the large, rigid PMMA particles, and act as lubrication, helping the PMMA particles to form aligned layers along the flow direction. The more concentrated the bimodal suspension is, the higher shear rate it requires to produce enough deformation of alginate beads so that they are able to squeeze between the neighboring PMMA particles and help to rearrange them. Hence, the shear thinning only occurs at high shear rate for very concentrated suspensions, and the starting point shifts to higher shear rates when the bulk concentration increases.

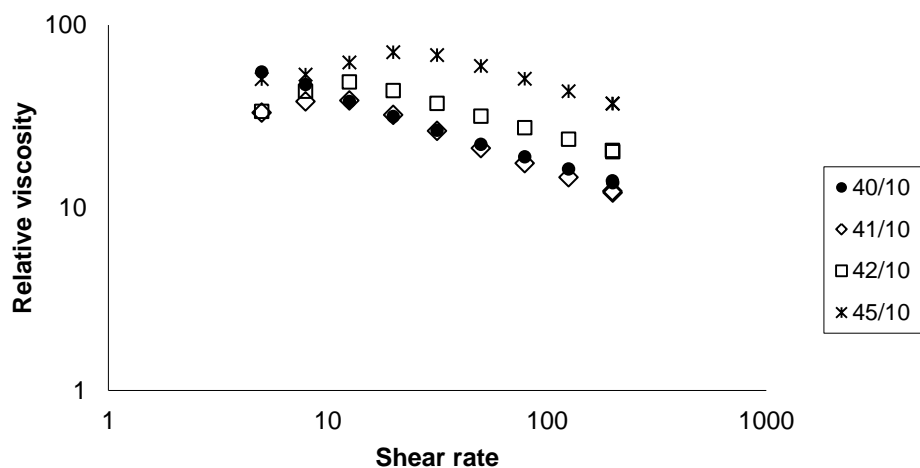


**Figure 6-8.** Relative viscosity of PMMA/alginate bimodal suspensions where the particle volume fraction of alginate beads was fixed at 10%, and the shear rate varied from  $5\text{ s}^{-1}$  to  $200\text{ s}^{-1}$ .

In the low shear rate range ( $5\text{-}30\text{ s}^{-1}$ ), only the viscosity curves of 40/5 (40% PMMA and 5% alginate), 40/10 (40% PMMA and 10% alginate) and 45/5 (45% PMMA and 5%

alginate) had a shear thinning trend, while in high shear rate range ( $30\text{--}200\text{ s}^{-1}$ ), all of the bimodal suspensions exhibited a shear thinning tendency. To compare the intensity of the shear thinning behavior, the slope of each viscosity curve in the high shear rate range shown in Figure 6-5, Figure 6-6, Figure 6-7 and Figure 6-8 was calculated and plotted against the relative volume fraction of small particles  $k$ . The data points from suspensions with several total bulk particle volume fractions roughly fall on a single curve, which exhibits a distinct minimum value in Figure 6-9. The slope (a negative value) of the viscosity curve initially decreases with an increase in  $k$ , and then increases until back to a value of zero. When  $k$  is around 0.27, the slope reaches the lowest point and maximum magnitude, indicating that the shear thinning behavior is most intense when the relative volume fraction of small particles equals 0.27. The only data point that is displaced from the main curve is the one that corresponds to 45% PMMA and 15% alginate beads. This observation suggests that when the bulk concentration is close to the maximum packing fraction, the limited free moving space becomes an obstacle to the ordering of PMMA particles, and therefore weakens the shear thinning behavior.

It appears that there is an optimal small particle volume fraction causing the rigid/soft bimodal suspension to have the most severe shear dependence when the large particle volume fraction is fixed. Below the optimal volume fraction, small, soft particles can easily migrate through the interstices of large, rigid particles and are not present in a large enough number to provide slip or lubrication to large, rigid particles under high shear rate, so that the shear thinning trend is not intense. Meanwhile, above the optimal volume fraction, the extra small soft particles may break the alignment of PMMA, resulting in

less shear thinning behavior at low shear rate. This phenomenon provides the possibility of tuning rheological properties of rigid/soft bimodal suspensions by adjusting the volume fraction of components and shear rate, so that a higher loading or ordered packing can be achieved.

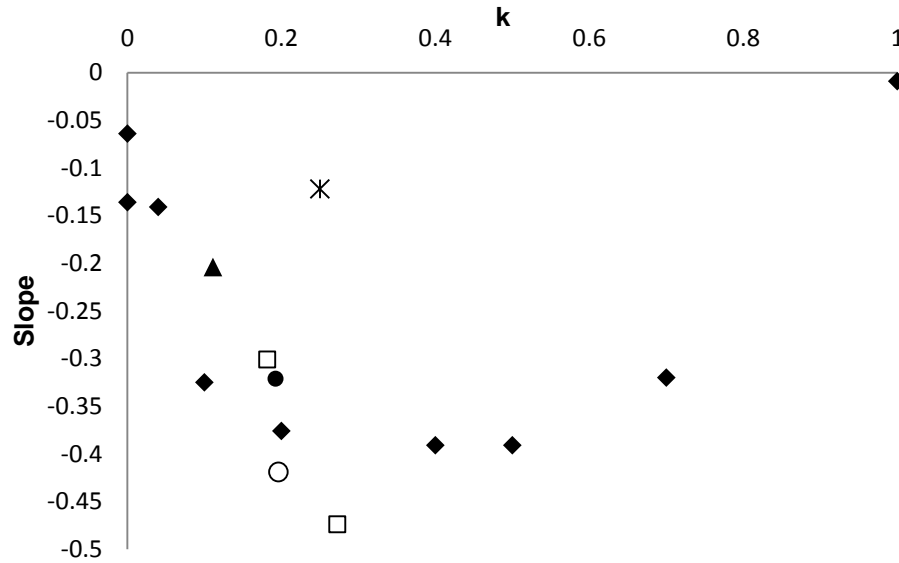


**Figure 6-9.** Intensity of shear dependence of PMMA/alginate bimodal suspensions with varied bulk concentration  $\phi$  and relative volume fraction of small particles  $k$ .  $\blacktriangle$ :  $\phi = 45\%$ ,  $\blacklozenge$ :  $\phi = 50\%$ ,  $\circ$ :  $\phi = 51\%$ ,  $\bullet$ :  $\phi = 52\%$ ,  $\square$ :  $\phi = 55\%$ ,  $*$ :  $\phi = 60\%$ .

Averaging the shearing data of suspensions when the bulk concentration  $\phi = 0.5$ , and comparing them with Qi and Tanner's model [92] (assuming  $\phi_{rec} = 0.6$ ), it shows that although Qi and Tanner's model successfully described many relative viscosity data sets of rigid bimodal suspensions, it is not in a good agreement with our experimental data, as shown in Figure 6-10. The model predicts the trend of relative viscosities of PMMA/alginate bimodal suspensions with varied volume fraction of small particles  $k$ , but it underestimates the value of the relative viscosities of our bimodal system. When



$k=0$  or  $k=1$ , the bidisperse system becomes monodisperse, and Qi and Tanner's model reduces to Mendoza and Santamaria-Holek's model. Apparently, Mendoza and Santamaria-Holek's model failed to assess the relative viscosities of concentrated monomodal suspensions, which may result from the fact that Mendoza and Santamaria-Holek's model does not consider the rigid particle interactions at high concentration. When  $k=0$ , the suspension only contains PMMA particles, and it is likely that the PMMA particles come into direct contact when the bulk concentration is high and therefore frictional and surface roughness effects may further increase the viscosity. Moreover, Mendoza and Santamaria-Holek's model does not apply to gel particle suspensions because of the porous morphology of the particles. For  $k=1$ , the suspension contains pure alginate gel beads. The suspending fluid is able to flow through the pores in the particles, so that the relative viscosity would be much lower than expected.

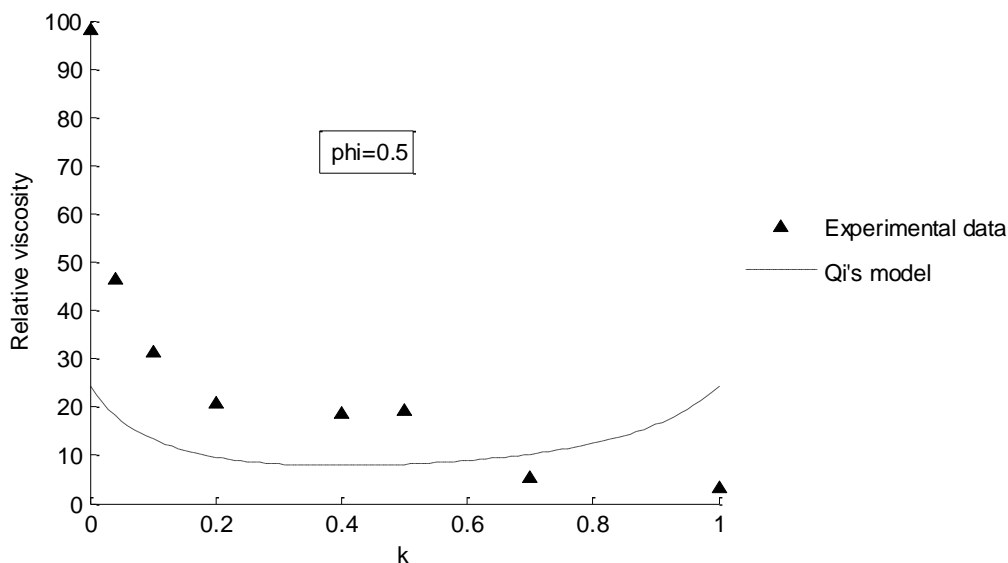


**Figure 6-10.** Estimated relative viscosity of PMMA/alginate bimodal suspensions by Qi's model vs. experimental data where the bulk concentration  $\phi$  was fixed at 50% and the relative volume fraction of small particles  $k$  was varied.

### 6.3.3 Model design

To improve the model for a better description of a rigid/soft particle bidisperse system, Equation (6-8) was modified to the following form,

$$\eta_r = \frac{\eta(\phi_l, \phi_s)}{\eta_0} = \frac{\eta(\phi_s)}{\eta_0} \frac{\eta(\phi_l, \phi_s)}{\eta(\phi_s)} = H(s/0)H(l/s) \quad (6-14)$$

$H(s/0)$  is the relative viscosity of soft particle suspensions. We found that the Maron-Pierce-Kitano model could be used to assess the rheological behavior of alginate gel particle suspensions when the power was scaled to -0.72, as seen in equation (6-15). The modified Maron-Pierce-Kitano model is proved to capture the relative viscosities of alginate monomodal suspensions, as shown in Figure 6-11.

$$H(s/0) = \left(1 - \frac{\phi}{\phi_{rcp}}\right)^{-0.72} \quad (6-15)$$

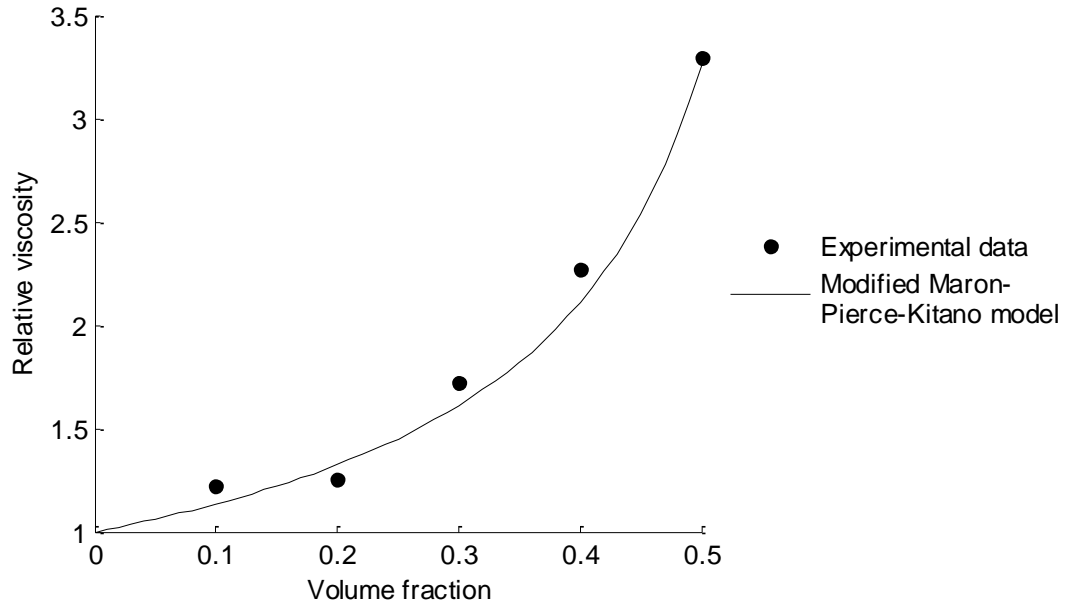


**Figure 6-11.** Estimated relative viscosity of alginate monomodal suspensions by modified Maron-Pierce-Kitano model vs. experimental data.

$H(l/s)$  is the relative viscosity of large rigid particles embedded in the “continuous phase” mixture of suspending fluid and small soft particles. The Zarraga model was used to describe the rheological behavior of rigid PMMA particle suspensions (Zarraga *et al.*, 2000). Since the matrix consisted of both suspending fluid and alginate beads,  $\phi_{rcp}$  was replaced by  $\phi_{bm} - \phi_s$  as shown in the Equation (6-16).  $\phi_{bm}$  can be calculated by Equations (3), (4), (5) taken from the original Qi and Tanner model.

$$H(l/s) = \frac{e^{-2.34\phi}}{\left(1 - \frac{\phi_l}{\phi_{bm} - \phi_s}\right)^3} \quad (6-16)$$

Therefore,

$$\eta_r = \left(1 - \frac{\phi}{\phi_{rcp}}\right)^{-0.72} \frac{e^{-2.34\phi}}{\left(1 - \frac{\phi_l}{\phi_{bm} - \phi_s}\right)^3} \quad (6-17)$$

The estimated relative viscosities of rigid/soft bimodal systems were computed and plotted in Figure 6-12, which shows good agreement to experimental data. The only odd point is the one that has 50% plain PMMA particles. Similar to the Mendoza and Santamaria-Holek model, the Zarraga model failed to predict the fact that PMMA particles may cause extremely large increases in the relative viscosity at high bulk concentration. Compared with Qi's model, the modified model exhibits a significant improvement in characterizing the rheological behavior of soft/rigid particle suspensions, presented in Figure 6-13.

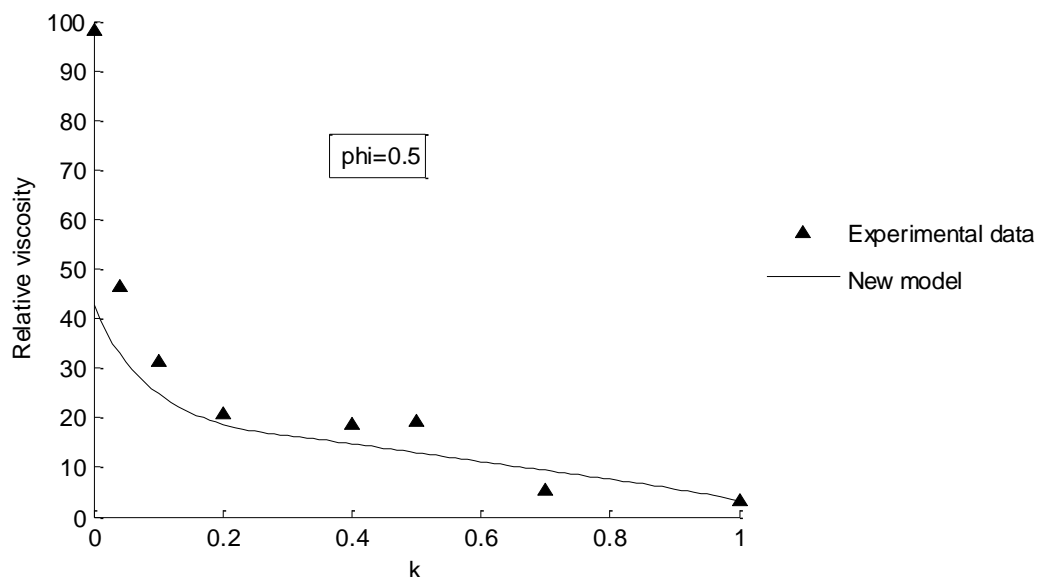


**Figure 6-12.** Estimated relative viscosity of PMMA/alginate bimodal suspensions by new model vs experimental data when bulk concentration  $\phi$  was fixed at 50% and relative volume fraction of small particles  $k$  was varied.

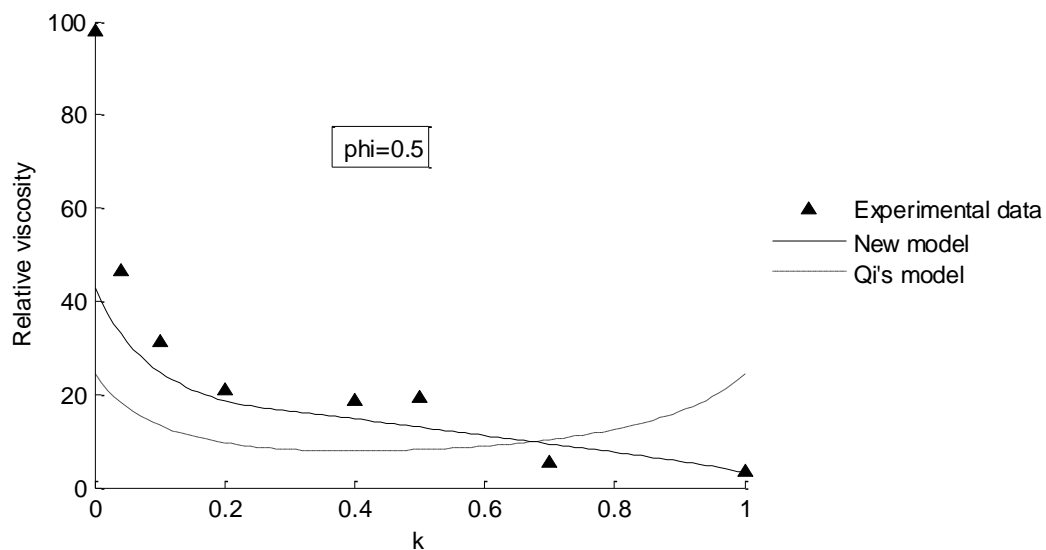


**Figure 6-13.** Comparison of estimated relative viscosity of PMMA/alginate bimodal suspensions by Qi's model, new model and experimental data when bulk concentration  $\phi$  was fixed at 50% and relative volume fraction of small particles  $k$  was varied.

### 6.3 Summary

The relative viscosity of bimodal suspensions consisting of rigid, large PMMA particles and soft, small alginate beads with varied volume fraction and bulk concentration were measured in a parallel plate viscometer. The rheological properties of rigid/soft particle bimodal suspensions have been discussed and a recent model has been adapted for such systems in this paper.

Both PMMA particle suspensions and alginate gel particle monomodal suspensions exhibit approximately shear-independent behavior. Once they are mixed, a strong shear thinning tendency occurs in the bimodal suspensions. One possible explanation of the enhanced shear thinning is that soft small alginate beads may provide slip or lubrication to PMMA particles, and help PMMA particles to align along the flow direction when the bulk concentration is high, which causes significant shear thinning of bimodal suspensions. However, if the volume fraction of small alginate gel beads is extremely low, the viscosity of a bimodal suspension is dominated by the large, rigid PMMA particles, because the small soft particles can easily migrate through the interstices of the large, rigid particles, so that the interaction between small and large particles is negligible.

Despite the effect of shear rate, the average relative viscosity of bimodal suspensions increases when the volume fraction of small gel alginate beads decreases at fixed total bulk concentration. Below a certain bulk concentration of about  $\phi \sim 55\text{-}60\%$ , there is an

optimal relative volume fraction of small particles for causing the rigid/soft bimodal suspension to display the most severe shear dependence. In the high shear rate range, the intensity of shear dependence at first increases with the increase of the relative volume fraction of alginate gel particles, and then decreases until it reduces to the quasi-Newtonian behavior of a monomodal suspension. When the bulk concentration is close to the maximum packing fraction, the limited free moving space becomes an obstacle to the ordering and alignment of PMMA particles, and therefore weakens the shear thinning behavior.

A new model for the relative viscosity of rigid/soft particle bimodal suspensions has been developed. The model is based on the Zarraga model and the Maron-Pierce-Kitano model, and adopts Qi's method to calculate the maximum packing particle volume fraction for bimodal suspensions. The estimation of the relative viscosity for several bimodal suspensions is compared to experimental data, and good agreement is observed.

## Chapter 7 Conclusion and Future Work

### 7.1 Conclusion

Chitosan and alginate are highly abundant, edible and biocompatible natural carbohydrate materials used to remove heavy metal ions from aqueous solutions. In this research, we use chitosan and alginate at various size scales as biosorbents, to seek enhanced understanding of the process and mechanisms of metal ion adsorption, with the aim of guiding the next generation of water purification system design.

First, equilibrium adsorption properties of chitosan gel nanoparticles, calcium-alginate gel microbeads, chitosan/alginate combination particles and large calcium-alginate gel beads were investigated in order to optimize biosorbent choice. Particles were synthesized and characterized by TEM and zetasizing. The equilibrium adsorption capability of the chitosan gel nanoparticles, calcium-alginate gel microbeads, chitosan/alginate combination particles and large calcium-alginate gel beads to adsorb copper ions from copper sulfate solution at fixed pH has been explored. It was found that equilibrium adsorption properties of chitosan nanoparticles have similar trends to those of calcium-alginate gel microbeads and large calcium-alginate gel beads, and the adsorption capacity varies with the synthesis concentration of chitosan nanoparticles. Adsorption for both chitosan nanoparticles and alginate microbeads occurs differently in a low concentration (0.5-50 mM) copper sulfate solution and a high concentration solution (50mM-1 M). The

Langmuir isotherm fits the low concentration region well. In contrast, approximately linearly increasing adsorption was observed at high solution concentrations.

To explore the adsorption mechanism, the adsorption properties of several types of chitosan nanoparticles for copper ions were compared, which suggests that the phosphate groups in the cross-linker TPP can provide additional adsorption sites that have lower affinity than amine groups for copper ions. In addition, exceptionally high affinity between copper ions and chitosan nanoparticles may result in the pore blockage phenomenon, where the interior of the particle becomes inaccessible, and consequently limits the adsorption capacity of particles.

From a comparison between the experimental data and approximate calculations estimating the maximum adsorption capacity of the materials, the most probable adsorption mechanisms could be identified. The “bridge model” can be considered a reasonable description of the chitosan/metal ion binding pattern. Also, adsorption sites of alginate are most likely to be formed by only one mannuronate or guluronate block, in contrast to the four guluronate subunits required by the “egg-box” model. Comparing the two biopolymers, in both the low and high concentration ranges, calcium-alginate gel microbeads have a higher maximum adsorption capacity than that of chitosan nanoparticles, likely due to the higher estimated density of adsorption sites present in alginate compared to chitosan with the properties of the experimental system.



Alginate-chitosan combination particles were also observed, which have an intermediate value of the maximum adsorption capacity  $Q_{max}$ , and identical value of the affinity coefficient  $K_s$  to that of alginate microbeads in part because of structural similarity to alginate beads. The adsorption capabilities of combination particles can be predicted by the weight ratio of calcium-alginate gel microbeads and chitosan gel nanoparticles. Benefitting from the rapid kinetics of chitosan nanoparticles and the high adsorption capacity of alginate, alginate-chitosan combination particles are likely to perform effectively and efficiently in multi-ion systems as a novel, environmentally friendly biosorbent.

Next, the adsorption kinetics of copper ions on to calcium-alginate gel microbeads, chitosan/alginate combination particles and large calcium-alginate gel beads were investigated in addition to the equilibrium study, since the kinetics affect the efficiency and in-service life of a water purification system directly. It was observed that the adsorption of copper ions on to alginate microbeads and combination particles was gradual, while the amount of copper loaded onto large calcium-alginate beads increased rapidly and sharply before reaching equilibrium. In other words, the adsorption kinetics of large calcium-alginate gel beads was much faster than that of alginate microbeads and combination particles, likely resulting from the pore blockage occurring on the surface of microbeads and combination particles. The adsorption of copper ions on to combination particles was slightly faster than on to plain alginate microbeads, benefitting from the existence of chitosan on combination particles. Large calcium-alginate gel beads had

smaller equilibrium adsorption capacity than alginate microbeads and combination particles due to their low degree of cross-linking compared to alginate microbeads.

Comparing experimental data to kinetics models, the result shows that the pseudo-first order kinetic model could not represent the adsorption process accurately, while the pseudo-second order kinetic model successfully predicted the adsorption behavior over the whole range of studies. It is confirmed that the chemisorption mechanism is the rate controlling step in the adsorption process of copper ions on to alginate microbeads, combination particles and large calcium-alginate gel beads from copper sulfate solution in a batch system, and the chemisorption reaction is second order.

After optimizing biosorbent choice by analyzing equilibrium adsorption data and adsorption kinetics of particles, an adsorption study in a continuous system was performed. Large calcium-alginate gel beads were chosen as the adsorbent and packed into a fixed-bed column, since they have high adsorption capacity and fast adsorption kinetics compared to chitosan nanoparticles, alginate microbeads and chitosan/alginate combination particles, and are unlikely to cause clogging or leaking in the fixed-bed columns. The adsorption behavior of fixed-bed columns packed with large calcium-alginate gel beads was studied by varying the column size and volumetric flow rate. The results show that when flow rate was high, the adsorption was performed relatively uniformly in the fixed-bed column, and the fixed-bed column might reach saturation at the end of experiment. For the low flow rate case, adsorption mainly occurred near the

inlet part of column. In the aspect of breaking through, a column had shorter active life at a higher flow rate, or having a smaller size.

There are two main factors in evaluating the efficiency of a fixed-bed column: BV number, and breakthrough time. A column with high BV number at breakthrough and moderate breakthrough time is believed to be performing well. Therefore, there is an optimal flow rate range for a certain size of column. Below that, the breakthrough time would be too long and volume of treated solution would be deficient, while above it, the BV number would be small and the adsorbent would not be used efficiently. In this study, the best tested fixed-bed column is the large column at 0.25 mL/min flow rate.

The Thomas model, Adams-Bohart model and Yoon-Nelson model were used to fit experimental data. All three models proved to be suitable for describing the adsorption behavior of fixed-bed columns. They also provided unique characteristic features, respectively, such as adsorption capacity (Thomas model, Adams-Bohart model), breakthrough curve without sufficient data (Thomas model), service time (Adams-Bohart model) and time for 50% breakthrough (Yoon-Nelson model).

Finally, the rheology of PMMA/alginate concentrated bimodal suspensions was studied, which can provide insight into particle migration and separation in complex flow observed in previous work, and therefore aids the further design of fixed-bed columns. The relative viscosity of bimodal suspensions consisting of rigid, large PMMA particles and soft, small alginate beads with varied volume fraction and bulk concentration were

measured in a parallel plate viscometer. Both PMMA and alginate gel monomodal particle suspensions exhibited nearly shear-independent behavior. Once they were mixed, a strong tendency toward shear thinning occurs in the bimodal suspensions. The enhanced shear thinning could be explained by the fact that soft, small alginate beads may provide slip or lubrication to PMMA particles, and help PMMA particles to align along the flow direction when the bulk concentration is high, which can cause significant shear thinning of bimodal suspensions. However, if the volume fraction of small alginate gel beads is extremely low, the viscosity of a bimodal suspension is dominated by the large, rigid PMMA particles, because the small, soft particles can easily migrate through the interstices of the large, rigid particles, so that the interaction between small and large particles is negligible.

Despite the effect of shear rate, the average relative viscosity of bimodal suspensions increases when the volume fraction of small gel alginate beads decreases at fixed total bulk concentration. Below a certain bulk concentration of about 55-60%, there is an optimal small particle volume fraction causing the rigid/soft bimodal suspension to have the most dramatic shear dependence. In the high shear rate range, the intensity of shear dependence initially increases with the increase of the relative volume fraction of alginate gel particles, and then decreases until it reduces to the quasi-Newtonian behavior of monomodal suspension. Where the bulk concentration is close to the maximum packing fraction, the limited free moving space becomes an obstacle to the ordering and alignment of PMMA particles, and therefore weakens the shear thinning behavior.

A recent model for the relative viscosity of bimodal suspensions has been adapted to rigid/soft particle systems. The new model was built based on the Zarraga model and the Maron-Pierce-Kitano model, and adopted Qi and Tanner's method to calculate the maximum packing fraction for bimodal suspensions. The estimation of the relative viscosity for several bimodal suspensions was compared to experimental data, and good agreement was observed.

## **7.2 Future work**

There are many opportunities for future work to extend this project. First of all, work should continue on the adsorption behavior of a continuous fixed-bed column. Variations on the operation parameters of a fixed-bed column such as the concentration of the initial solution, flow rate and adsorption time provide potential areas for research. Adsorption time could be prolonged until the concentration of the outflow equals the initial concentration of solution, in order to collect a complete data set that is able to describe the entire adsorption process and therefore get more accurate model fitting. The relationship between column size and its corresponding optimal flow rate should be explored. Since the shape of the column may affect the flow pattern inside the column, the effect of the column geometry could be studied by comparing the adsorption capacities of fixed-bed columns with different cross section area/length ratio when other parameters are fixed.

Besides, it would be interesting to locate the active adsorbing part inside a column. From the results presented in this study, it was shown that the equilibrium adsorption capacity of a biosorbent in a continuous fixed-bed column was lower than that in a batch system, indicating that the flow pattern was uneven and there were flow bypasses existing in the column. NMR imaging could be used in an investigation, by which the uneven flow pattern and mass transfer inside the column could be observed visually. And it would provide valuable information to generate better packing of the biosorbent, and therefore improve the adsorption efficiency of fixed-bed column and lower the cost.

Finally, the biosorbent packed into fixed-bed columns could be further optimized. In the study of equilibrium adsorption capacity and adsorption kinetics of particles, it was found that alginate/chitosan combination particles are likely to perform effectively and efficiently, benefitting from the rapid kinetics of chitosan nanoparticles and the high adsorption capacity of alginate. More importantly, they could be used in multi-ion systems since chitosan nanoparticles are able to adsorb not only cations but also anions. The only problem of using them in the study of fixed-bed column is that they may clog the column and cause severe leaking. If there is some method to solve that problem, for example, encapsulating them inside the large calcium-alginate gel beads (or only encapsulating chitosan nanoparticles if it won't lead to aggregation), alginate/chitosan combination particles would have great potential to serve as a novel, environmentally friendly biosorbent.

# Acknowledgement of Previous Publications

Several sections of this dissertation have been published elsewhere or are being prepared for publication. The following are acknowledged:

- Chapter 3 has been published in full under the citation:

**K. Yu, J. Ho, E. McCandlish, B. Buckley, R. Patel, Z. Li, N.C. Shapley,** Copper ion adsorption by chitosan nanoparticles and alginate microparticles for water purification applications, *Colloids and Surfaces A: Physicochemical and Engineering Aspects*, 425 (2013) 31-41.

- Sections of Chapter 4 and 5 are being prepared for publication under the citation:

**K. Yu, N. C. Shapley,** “Batch system and continuous packed column studies of copper adsorption by alginate gel particles.”

- Sections of Chapter 6 is being prepared for publication under the citation:

**K. Yu, N. C. Shapley,** “Rheology of a concentrated bimodal suspension containing rigid and soft particles.”

## References

- [1] R.-S. Juang, H.-J. Shao, Effect of pH on Competitive Adsorption of Cu(II), Ni(II), and Zn(II) from Water onto Chitosan Beads, *Adsorption*, 8 (2002) 71-78.
- [2] N. Li, R. Bai, Copper adsorption on chitosan–cellulose hydrogel beads: behaviors and mechanisms, *Separation and Purification Technology*, 42 (2005) 237-247.
- [3] N. Savage, M.S. Diallo, Nanomaterials and Water Purification: Opportunities and Challenges, *Journal of Nanoparticle Research*, 7 (2005) 331-342.
- [4] R. Schmuhl, H. Krieg, K. Keizer, Adsorption of Cu(II) and Cr(VI) ions by chitosan: Kinetics and equilibrium studies, *Water SA*, 27 (2001) 1-7.
- [5] P. Udaybaskar, L. Iyengar, A.V.S.P. Rao, Hexavalent chromium interaction with chitosan, *Journal of Applied Polymer Science*, 39 (1990) 739-747.
- [6] V.M. Boddu, K. Abburi, J.L. Talbott, E.D. Smith, Removal of Hexavalent Chromium from Wastewater Using a New Composite Chitosan Biosorbent, *Environmental Science & Technology*, 37 (2003) 4449-4456.
- [7] M. Pérez-Candela, J. Martín-Martínez, R. Torregrosa-Maciá, Chromium(VI) removal with activated carbons, *Water Research*, 29 (1995) 2174-2180.
- [8] A. Findon, G. McKay, H.S. Blair, Transport studies for the sorption of copper ions by chitosan, *Journal of Environmental Science and Health . Part A: Environmental Science and Engineering and Toxicology*, 28 (1993) 173-185.
- [9] J.C.Y. Ng, W.H. Cheung, G. McKay, Equilibrium Studies of the Sorption of Cu(II) Ions onto Chitosan, *Journal of Colloid and Interface Science*, 255 (2002) 64-74.
- [10] W.S. Wan Ngah, C.S. Endud, R. Mayanar, Removal of copper(II) ions from aqueous solution onto chitosan and cross-linked chitosan beads, *Reactive and Functional Polymers*, 50 (2002) 181-190.
- [11] G. McKay, H.S. Blair, A. Findon, Equilibrium studies for the sorption of metal-ions onto chitosan, *Indian Journal of Chemistry*, A28 (1989) 356-360.
- [12] Ö. Genç, L. Soysal, G. Bayramoğlu, M.Y. Arica, S. Bektaş, Procion Green H-4G immobilized poly(hydroxyethylmethacrylate/chitosan) composite membranes for heavy metal removal, *Journal of Hazardous Materials*, 97 (2003) 111-125.
- [13] J.C.Y. Ng, W.H. Cheung, G. McKay, Equilibrium studies for the sorption of lead from effluents using chitosan, *Chemosphere*, 52 (2003) 1021-1030.



- [14] H. Niu, X.S. Xu, J.H. Wang, B. Volesky, Removal of lead from aqueous solutions by *Penicillium* biomass, *Biotechnology and Bioengineering*, 42 (1993) 785-787.
- [15] H. Zhang, M. Oh, C. Allen, E. Kumacheva, Monodisperse Chitosan Nanoparticles for Mucosal Drug Delivery, *Biomacromolecules*, 5 (2004) 2461-2468.
- [16] M.U. Larsen, M. Seward, A. Tripathi, N.C. Shapley, Biocompatible nanoparticles trigger rapid bacteria clustering, *Biotechnology Progress*, 25 (2009) 1094-1102.
- [17] I.M. Helander, E.L. Nurmiäho-Lassila, R. Ahvenainen, J. Rhoades, S. Roller, Chitosan disrupts the barrier properties of the outer membrane of Gram-negative bacteria, *International Journal of Food Microbiology*, 71 (2001) 235-244.
- [18] G. Azadi, M. Seward, M. Larsen, N. Shapley, A. Tripathi, Improved Antimicrobial Potency through Synergistic Action of Chitosan Microparticles and Low Electric Field, *Applied Biochemistry and Biotechnology*, 168 (2012) 531-541.
- [19] F.-L. Mi, S.-S. Shyu, S.-T. Lee, T.-B. Wong, Kinetic study of chitosan-tripolyphosphate complex reaction and acid-resistive properties of the chitosan-tripolyphosphate gel beads prepared by in-liquid curing method, *Journal of Polymer Science Part B: Polymer Physics*, 37 (1999) 1551-1564.
- [20] C. Gerente, V.K.C. Lee, P.L. Cloirec, G. McKay, Application of Chitosan for the Removal of Metals From Wastewaters by Adsorption—Mechanisms and Models Review, *Critical Reviews in Environmental Science and Technology*, 37 (2007) 41-127.
- [21] E. Guibal, Interactions of metal ions with chitosan-based sorbents: a review, *Separation and Purification Technology*, 38 (2004) 43-74.
- [22] K. Inoue, Y. Baba, K. Yoshizuka, Adsorption of Metal Ions on Chitosan and Crosslinked Copper(II)-Complexed Chitosan, *Bulletin of the Chemical Society of Japan*, 66 (1993) 2915-2921.
- [23] R.A.A. Muzzarelli, Tanfani, F., Emanuelli, M., Gentile, S., The chelation of cupric ions by chitosan membranes, *Journal of Applied Biochemistry* 2(1980) 380-389.
- [24] S. Schlick, Binding sites of copper<sup>2+</sup> in chitin and chitosan. An electron spin resonance study, *Macromolecules*, 19 (1986) 192-195.
- [25] J.W. Park, Park, M.O., Park, K.K., Mechanism of metal binding to chitosan in solution: Cooperative inter- and intramolecular chelations, *Bulletin of the Korean Chemical Society*, 5 (1984) 108-112.
- [26] W. Kamiński, Z. Modrzejewska, Application of Chitosan Membranes in Separation of Heavy Metal Ions, *Separation Science and Technology*, 32 (1997) 2659-2668.

- [27] K. Ogawa, T. Yui, Crystallinity of Partially N-Acetylated Chitosans, *Bioscience, biotechnology, and biochemistry*, 57 (1993) 1466-1469.
- [28] J.M. Nieto, C. Peniche-Covas, J. Del Bosque, Preparation and characterization of a chitosan-Fe(III) complex, *Carbohydrate Polymers*, 18 (1992) 221-224.
- [29] A. Domard, pH and c.d. measurements on a fully deacetylated chitosan: application to CuII—polymer interactions, *International Journal of Biological Macromolecules*, 9 (1987) 98-104.
- [30] E. Chiessi, G. Paradossi, M. Venanzi, B. Pispisa, Copper complexes immobilized to chitosan, *Journal of Inorganic Biochemistry*, 46 (1992) 109-118.
- [31] O.A.C. Monteiro Jr, C. Airoidi, Some Thermodynamic Data on Copper–Chitin and Copper–Chitosan Biopolymer Interactions, *Journal of Colloid and Interface Science*, 212 (1999) 212-219.
- [32] G.L. Rorrer, T.Y. Hsien, J.D. Way, Synthesis of porous-magnetic chitosan beads for removal of cadmium ions from wastewater, *Industrial & Engineering Chemistry Research*, 32 (1993) 2170-2178.
- [33] K. Inoue, K. Yoshizuka, K. Ohto, Adsorptive separation of some metal ions by complexing agent types of chemically modified chitosan, *Analytica Chimica Acta*, 388 (1999) 209-218.
- [34] F.-L. Mi, H.-W. Sung, S.-S. Shyu, C.-C. Su, C.-K. Peng, Synthesis and characterization of biodegradable TPP/genipin co-crosslinked chitosan gel beads, *Polymer*, 44 (2003) 6521-6530.
- [35] O. Smidsrød, G. Skjåk-Bræk, Alginate as immobilization matrix for cells, *Trends in Biotechnology*, 8 (1990) 71-78.
- [36] A. Martinsen, G. Skjåk-Bræk, O. Smidsrød, Alginate as immobilization material: I. Correlation between chemical and physical properties of alginate gel beads, *Biotechnology and Bioengineering*, 33 (1989) 79-89.
- [37] K. Draget, Smidsrød, O., Skjåk-Bræk, G., Alginates from algae, in: A. Steinbüchel, S.K. Rhee (Eds.) *Polysaccharides and polyamides in the food industry: properties, production, and patents*, WILEY-VCH Verlag GMBH & Co. KGaA, Weinheim, 2005, pp. xi + 771 pp.
- [38] N. Kamiya, A.M. Klibanov, Controlling the rate of protein release from polyelectrolyte complexes, *Biotechnology and Bioengineering*, 82 (2003) 590-594.

- [39] H. Zhu, R. Srivastava, J.Q. Brown, M.J. McShane, Combined Physical and Chemical Immobilization of Glucose Oxidase in Alginate Microspheres Improves Stability of Encapsulation and Activity, *Bioconjugate Chemistry*, 16 (2005) 1451-1458.
- [40] H.J. Hester-Reilly, N.C. Shapley, Imaging contrast effects in alginate microbeads containing trapped emulsion droplets, *Journal of Magnetic Resonance*, 188 (2007) 168-175.
- [41] M. Yakup Arica, Ç. Arpa, A. Ergene, G. Bayramoğlu, Ö. Genç, Ca-alginate as a support for Pb(II) and Zn(II) biosorption with immobilized *Phanerochaete chrysosporium*, *Carbohydrate Polymers*, 52 (2003) 167-174.
- [42] M. Yakup Arica, G. Bayramoğlu, M. Yılmaz, S. Bektaş, Ö. Genç, Biosorption of Hg<sup>2+</sup>, Cd<sup>2+</sup>, and Zn<sup>2+</sup> by Ca-alginate and immobilized wood-rotting fungus *Funalia troglia*, *Journal of Hazardous Materials*, 109 (2004) 191-199.
- [43] T. Gotoh, K. Matsushima, K.-I. Kikuchi, Adsorption of Cu and Mn on covalently cross-linked alginate gel beads, *Chemosphere*, 55 (2004) 57-64.
- [44] J.P. Ibáñez, Y. Umetsu, Uptake of trivalent chromium from aqueous solutions using protonated dry alginate beads, *Hydrometallurgy*, 72 (2004) 327-334.
- [45] I. Braccini, S. Pérez, Molecular Basis of Ca<sup>2+</sup>-Induced Gelation in Alginates and Pectins: The Egg-Box Model Revisited, *Biomacromolecules*, 2 (2001) 1089-1096.
- [46] C.K. Siew, P.A. Williams, N.W.G. Young, New Insights into the Mechanism of Gelation of Alginate and Pectin: Charge Annihilation and Reversal Mechanism, *Biomacromolecules*, 6 (2005) 963-969.
- [47] N. Emmerichs, J. Wingender, H.C. Flemming, C. Mayer, Interaction between alginates and manganese cations: identification of preferred cation binding sites, *International Journal of Biological Macromolecules*, 34 (2004) 73-79.
- [48] I. Donati, S. Holtan, Y.A. Mørch, M. Borgogna, M. Dentini, New Hypothesis on the Role of Alternating Sequences in Calcium–Alginate Gels, *Biomacromolecules*, 6 (2005) 1031-1040.
- [49] J. Rui Rodrigues, R. Lagoa, Copper Ions Binding in Cu-Alginate Gelation, *Journal of Carbohydrate Chemistry*, 25 (2006) 219-232.
- [50] I. Langmuir, THE CONSTITUTION AND FUNDAMENTAL PROPERTIES OF SOLIDS AND LIQUIDS. II. LIQUIDS.1, *Journal of the American Chemical Society*, 39 (1917) 1848-1906.
- [51] H.Z. Freundlich, Over the adsorption in solution, *Journal of Physical Chemistry*, 57 (1906) 385-470.

- [52] Y.S. Ho, G. McKay, Pseudo-second order model for sorption processes, *Process Biochemistry*, 34 (1999) 451-465.
- [53] S. Lagergren, Zur theorie der sogenannten adsorption gelöster stoffe. *Kungliga Svenska Vetenskapsakad, Handlingar*, 24 (1898) 39.
- [54] C. Aharoni, D.L. Sparks, Kinetics of Soil Chemical Reactions—A Theoretical Treatment, in: D.L. Sparks, D.L. Suarez (Eds.) *Rates of Soil Chemical Processes*, Soil Science Society of America, 1991, pp. 1-18.
- [55] Y.S. Ho, G. McKay, A Comparison of Chemisorption Kinetic Models Applied to Pollutant Removal on Various Sorbents, *Process Safety and Environmental Protection*, 76 (1998) 332-340.
- [56] H.C. Thomas, CHROMATOGRAPHY: A PROBLEM IN KINETICS, *Annals of the New York Academy of Sciences*, 49 (1948) 161-182.
- [57] G.C. Bohart, E.Q. Adams, Some aspect of the behavior of charcoal with respect to chlorine, *Journal of the American Chemical Society*, 42 (1920) 7.
- [58] Y.H. Yoon, J.H. Nelson, Application of Gas Adsorption Kinetics I. A Theoretical Model for Respirator Cartridge Service Life, *American Industrial Hygiene Association Journal*, 45 (1984) 509-516.
- [59] B. Thu, O. G åser ød, D. Paus, A. Mikkelsen, G. Skj åk-Bræk, R. Toffanin, F. Vittur, R. Rizzo, Inhomogeneous alginate gel spheres: An assessment of the polymer gradients by synchrotron radiation-induced x-ray emission, magnetic resonance microimaging, and mathematical modeling, *Biopolymers*, 53 (2000) 60-71.
- [60] N.S. Raghavan, D.M. Ruthven, Numerical simulation of a fixed-bed adsorption column by the method of orthogonal collocation, *AIChE Journal*, 29 (1983) 922-925.
- [61] T. Larsen, D.L. Taylor, M.B. Leigh, D.M. O'Brien, Stable isotope fingerprinting: a novel method for identifying plant, fungal, or bacterial origins of amino acids, *Ecology*, 90 (2009) 3526-3535.
- [62] W.S.W. Ngah, S. Fatinathan, Adsorption characterization of Pb(II) and Cu(II) ions onto chitosan-tripolyphosphate beads: Kinetic, equilibrium and thermodynamic studies, *Journal of Environmental Management*, 91 (2010) 958-969.
- [63] A. Karagunduz, D. Unal, New method for evaluation of heavy metal binding to alginate beads using pH and conductivity data, *Adsorption*, 12 (2006) 175-184.
- [64] H. Aydın, Y. Bulut, Ç. Yerlikaya, Removal of copper (II) from aqueous solution by adsorption onto low-cost adsorbents, *Journal of Environmental Management*, 87 (2008) 37-45.

- [65] R. Roscoe, The viscosity of suspensions of rigid spheres, *British Journal of Applied Physics*, 3 (1952) 3.
- [66] S.H. Maron, P.E. Pierce, Application of ree-eyring generalized flow theory to suspensions of spherical particles, *Journal of Colloid Science*, 11 (1956) 80-95.
- [67] I.M. Krieger, T.J. Dougherty, A Mechanism for Non-Newtonian Flow in Suspensions of Rigid Spheres, *Transactions of the Society of Rheology*, 3 (1959) 137-152.
- [68] I. Kreiger, Rheology of monodisperse latices, *Adv. Colloids Interface Sci*, 3 (1972) 111-136.
- [69] D.J. Jeffrey, A. Acrivos, The rheological properties of suspensions of rigid particles, *AIChE Journal*, 22 (1976) 417-432.
- [70] C. Castillo, M.C. Williams, RHEOLOGY OF VERY CONCENTRATED COAL SUSPENSIONS, *Chemical Engineering Communications*, 3 (1979) 529-545.
- [71] T. Kitano, T. Kataoka, T. Shirota, An Empirical Equation of the Relative Viscosity of Polymer Melts Fined with Various Inorganic Fillers, *Rheol. Acta*, 20 (1981) 3.
- [72] A.B. Metzner, Rheology of Suspensions in Polymeric Liquids, *Journal of Rheology*, 29 (1985) 739-775.
- [73] I.E. Zarraga, D.A. Hill, J.D.T. Leighton, The characterization of the total stress of concentrated suspensions of noncolloidal spheres in Newtonian fluids, *Journal of Rheology*, 44 (2000) 185-220.
- [74] C.I. Mendoza, I. Santamaria-Holek, The rheology of hard sphere suspensions at arbitrary volume fractions: An improved differential viscosity model, *The Journal of Chemical Physics*, 130 (2009) 044904-044907.
- [75] J.S. Chong, E.B. Christiansen, A.D. Baer, Rheology of concentrated suspensions, *Journal of Applied Polymer Science*, 15 (1971) 2007-2021.
- [76] R.F. Storms, B.V. Ramarao, R.H. Weiland, Low shear rate viscosity of bimodally dispersed suspensions, *Powder Technology*, 63 (1990) 247-259.
- [77] C. Chang, R.L. Powell, Effect of particle size distributions on the rheology of concentrated bimodal suspensions, *Journal of Rheology*, 38 (1994) 85-98.
- [78] D.M. Husband, L.A. Mondy, E. Ganani, A.L. Graham, Direct measurements of shear-induced particle migration in suspensions of bimodal spheres, *Rheol. Acta*, 33 (1994) 185-192.

- [79] M.K. Lyon, L.G. Leal, An experimental study of the motion of concentrated suspensions in two-dimensional channel flow. Part 2. Bidisperse systems, *Journal of Fluid Mechanics*, 363 (1998) 57-77.
- [80] G.P. Krishnan, S. Beimfohr, D.T. Leighton, Shear-induced radial segregation in bidisperse suspensions, *Journal of Fluid Mechanics*, 321 (1996) 371-393.
- [81] A. Shauly, A. Wachs, A. Nir, Shear-induced particle migration in a polydisperse concentrated suspension, *Journal of Rheology* (1978-present), 42 (1998) 1329-1348.
- [82] A. Ramachandran, D.T. Leighton, The influence of secondary flows induced by normal stress differences on the shear-induced migration of particles in concentrated suspensions, *Journal of Fluid Mechanics*, 603 (2008) 207-243.
- [83] R.J. Farris, Prediction of the Viscosity of Multimodal Suspensions from Unimodal Viscosity Data, *Transactions of the Society of Rheology*, 12 (1968) 281-301.
- [84] P. D'Haene, J. Mewis, Rheological characterization of bimodal colloidal dispersions, *Rheola Acta*, 33 (1994) 165-174.
- [85] A.A. Zaman, B.M. Moudgil, Rheology of bidisperse aqueous silica suspensions: A new scaling method for the bidisperse viscosity, *Journal of Rheology*, 42 (1998) 21-39.
- [86] A.A. Zaman, B.M. Moudgil, Role of Electrostatic Repulsion on the Viscosity of Bidisperse Silica Suspensions, *Journal of Colloid and Interface Science*, 212 (1999) 167-175.
- [87] R.D. Sudduth, A generalized model to predict the viscosity of solutions with suspended particles. I, *Journal of Applied Polymer Science*, 48 (1993) 25-36.
- [88] S. Yerazunis, J.W. Bartlett, A.H. Nissan, Packing of Binary Mixtures of Spheres and Irregular Particles, *Nature*, 195 (1962) 3.
- [89] A.J. Poslinski, M.E. Ryan, R.K. Gupta, S.G. Seshadri, F.J. Frechette, Rheological Behavior of Filled Polymeric Systems II. The Effect of a Bimodal Size Distribution of Particulates, *Journal of Rheology*, 32 (1988) 751-771.
- [90] A.P. Shapiro, R.F. Probst, Random packings of spheres and fluidity limits of monodisperse and bidisperse suspensions, *Physical Review Letters*, 68 (1992) 1422-1425.
- [91] S. Yerazunis, S.W. Cornell, B. Wintner, Dense Random Packing of Binary Mixtures of Spheres, *Nature*, 207 (1965) 3.
- [92] F. Qi, R. Tanner, Relative viscosity of bimodal suspensions, *Korea-Aust. Rheol. J.*, 23 (2011) 105-111.

- [93] H. Zhao, E.S.G. Shaqfeh, Shear-induced platelet margination in a microchannel, *Physical Review E*, 83 (2011) 061924.
- [94] A. Kumar, M.D. Graham, Margination and segregation in confined flows of blood and other multicomponent suspensions, *Soft Matter*, 8 (2012) 10536-10548.
- [95] A. Kumar, M.D. Graham, Mechanism of Margination in Confined Flows of Blood and Other Multicomponent Suspensions, *Physical Review Letters*, 109 (2012) 108102.
- [96] A. Ramachandran, D.T. Leighton, Particle migration in concentrated suspensions undergoing squeeze flow, *Journal of Rheology* (1978-present), 54 (2010) 563-589.
- [97] D.H. McCoy, M.M. Denn, Secondary flow in a parallel-disk viscometer, *Rheola Acta*, 10 (1971) 408-411.
- [98] J. Mewis, A.J.B. Spaul, Rheology of concentrated dispersions, *Advances in Colloid and Interface Science*, 6 (1976) 173-200.
- [99] R.R. Miller, E. Lee, R.L. Powell, Rheology of solid propellant dispersions, *Journal of Rheology*, 35 (1991) 901-920.
- [100] F. Blanc, E. Lemaire, A. Meunier, F. Peters, Microstructure in sheared non-Brownian concentrated suspensions, *Journal of Rheology*, 57 (2013) 273-292.